Particle Emission from Extreme Ultraviolet Light Sources

Dissertation

zur Erlangung des akademischen Grades
doctor rerum naturalium

vorgelegt dem Rat der Physikalisch-Astronomischen Fakultät der
Friedrich-Schiller-Universität Jena

von Diplom-Physiker **Thomas Brauner**

geboren am 23.03.1976 in Wittlich

Gutachter:

1. Prof. Dr. R. Sauerbrey, Forschungszentrum Dresden-Rossendorf (Deutschland)

2. Prof. Dr. H. Fiedorowicz, Military University of Technology Warszawa (Polen)

3. Prof. Dr. D. Ruzic, University of Illinois at Urbana-Champaign (USA)

Tag der letzten Rigorosumsprüfung: 26.04.2007

Tag der öffentlichen Verteidigung: 29.05.2007

Contents

Chapter 1

Introduction

In the past years, the density of transistors on a microchip has doubled approximately every eighteen months. This fact is often referred to as Moore's law, named after one of the founders of the well-known technology company Intel [1]. The semiconductor industry is very interested in continuing the pace of this progress. However, the current manufacturing technology is at its limits and will require some major changes in order to further increase the integration. The general direction of research and development in that field are coordinated by the International Technology Roadmap for Semiconductors [2].

Today's microchips are fabricated by optical lithography technology. In optical lithography, the semiconductor wafer is coated with a photosensitive material called photo resist. The desired pattern is projected with a mask onto the photo resist, where it causes a photochemical reaction. Depending on the nature of the photo resist, the exposed or the unexposed areas can be chemically dissolved, so that the photo resist takes on the projected pattern. This then enables selective etching in the areas without photo resist. In this way the pattern can be etched into the surface of the wafer. Similarly, it is possible to grow additional layers of semiconductor crystal selectively on areas that are coated or uncoated with photo resist. By combining these techniques, and performing them many times with different masks, very small and complex structures can be given to the wafers.

The minimum possible structure size that can be achieved by this technique is determined by the optical resolution RES of the imaging. This is given by

$$RES = \frac{k_1 \lambda}{NA} \,, \tag{1.1}$$

where λ is the wavelength of the light being used, NA the numerical aperture of the imaging system and k_1 an application dependent coefficient. Another important parameter is the depth of focus (DOF), given by

$$DOF = \frac{k_2 \lambda}{NA^2} \,, \tag{1.2}$$

where k_2 is - as k_1 in 1.1 - an application dependent coefficient. For diffraction-limited imaging, k_1 and k_2 equal 0.61. It can easily be seen that there are two ways to decrease the structure sizes: The wavelength used λ can be decreased or the numerical aperture NA can be increased.

In the past twenty years, the lithography process was improved by continuously decreasing the wavelength of the light used. Lasers are used as a light source, providing monochromatic light at high intensities. Throughout this development, no major changes had to be implemented to the rest of the lithography system. At the moment, microchip production is done using excimer lasers in the vacuum UV (VUV) using optical components made of calcium fluoride or magnesium fluoride. However, the shortest commercially available laser wavelength is 157 nm.

For the lithography of smaller structures both parameters λ and NA are under consideration. The continued reduction of the wavelength leads to extreme ultraviolet (EUV) lithography. For scaling up the numerical aperture, the refractive index of the light path needs to be increased. This approach leads to immersion lithography. The work in this thesis is concerned with extreme ultraviolet lithography.

1.1 Extreme Ultraviolet Radiation

1.1.1 Optical Properties of EUV Radiation

Electromagnetic radiation in the wavelength range of about 5-20 nm is usually called extreme ultraviolet radiation. The most important feature of EUV radiation is that it is strongly absorbed in any known medium - even in gases at low pressures. Two immediate conclusions can be drawn from this fact: First, only reflective optics can be used for imaging as there are no transmissive optical elements for EUV radiation. Second, the whole imaging system, from the light source to the wafer, has to be in high vacuum.

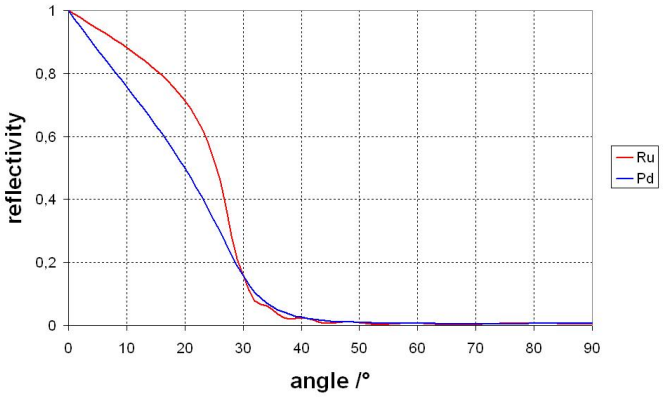

Figure 1.1: Reflectivity of ruthenium and palladium for EUV radiation. For this figure a 50 nm thick layer of the metal on a nickel substrate was assumed. The substrate and the coating were both assumed to have no roughness at all. Therefore this graph represents an ideal grazing incidence mirror. The values were calculated with [4].

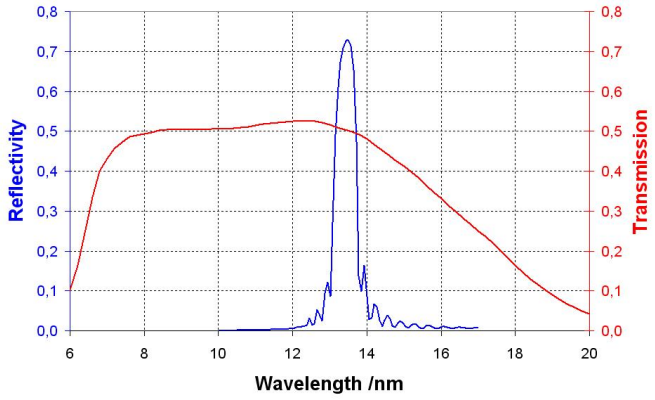

Figure 1.2: Reflectivity spectrum of a 40 bilayer Si/Mo mirror (blue) and transmission spectrum of a 0.2 micron Zr filter (red). Both spectra have been calculated with [4].

Reflective optics in the EUV range can be either very smooth grazing incidence mirrors or multilayer systems that work at and near normal incidence. Ruthenium and palladium are very common surface materials for grazing incidence EUV mirrors. Their reflectivity dependence on the incidence angle is shown in fig. 1.1.

There are two known multilayer systems reflecting in the EUV range: molybdenum and beryllium reflecting around 11.5 nm, or silicon and molybdenum reflecting around 13.5 nm (see fig. 1.2). The Mo/Be has a smaller reflection bandwidth and therefore a lower integral reflectivity [3]. Additionally, beryllium dust is toxic and causes cancer, which makes it unsuitable for industrial use. Therefore the agreed wavelength for EUV lithography is set to be 13.5 nm with a bandwidth of 2%. All numbers of EUV power in this work are to be seen as integrated over this spectral bandwidth, unless specified differently.

1.1.2 Sources of EUV Radiation

There are two known sources of EUV radiation that could be powerful enough to meet the industry requirements: radiation taken out of a synchrotron or emitted by a hot plasma. The use of a synchrotron is being ruled out as there are strong doubts that it could work economically for high volume manufacturing (HVM). The research focus is therefore put on hot plasmas. These can be produced by two ways: either by focusing a powerful short pulse laser onto a target, creating a laser produced plasma (LPP) (see section 1.3) or by producing a strong gas discharge (GDP) (see section 1.4). In both cases a plasma will form, emitting electromagnetic radiation dependent on its parameters. The EUV radiation will be collected by a suitable mirror and focused into the so-called intermediate focus (IF). The IF serves as interface to the other optical components of the stepper. Thus the source parameters have to be defined at the IF. Furthermore, the IF serves as a flow resistance between the different vacuum chambers, so that the imaging optics can be kept in a much better and cleaner vacuum than the source.

The output power at 13.5 nm and the lifetime of components and optics have shown to be the most critical factors in EUV source development [5]. The parameter one tries to optimise in respect of output power is usually the conversion efficiency (CE), which is defined as the ratio of laser power (for LPP) or electrical power (for GDP) and the EUV emission power into a solid angle of 2π sterad (see section 1.2.3).

The most limiting factor in components lifetime of a GDP is the lifetime of the electrode system. The electrodes have a rather short distance (approx. 1 cm) to the plasma. When they operate at kHz repetition rates, they have to cope with the major part of heat dissipation from the plasma and have to be cooled. However, the surfaces of the electrode will slowly evaporate in the process. Optimising the electrode lifetime mainly consists of finding electrode materials and geometries that minimise evaporation, and applying cooling circuits that can remove the heat energy from the electrodes very efficiently.

In an LPP, no solid parts have to be near the plasma, so there is no problem of surface evaporation due to heating. However, the laser window of the vacuum chamber can be subject to damage due to the debris effect (see section 1.5) and exposure to intense UV radiation.

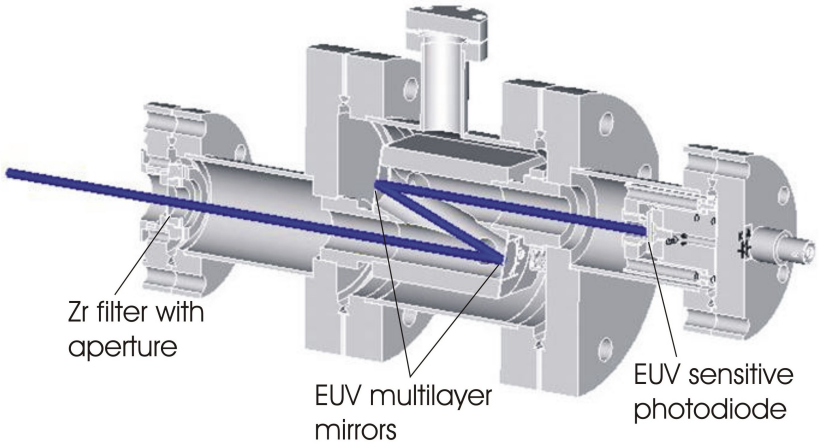

Figure 1.3: Illustration of an energy monitor. The EUV light has to pass a Zr filter and two multilayer mirrors [8].

The limits in optics lifetime for both LPP and GDP are mainly determined by the debris effect. This problem will be described in more detail in section 1.5.

1.1.3 EUV Metrology

1.1.3.1 Energy Monitor

The standard device for the calibrated measurement of EUV radiation power is the energy monitor originally manufactured by Jenoptik Mikrotechnik [6]. Meanwhile this product is produced by XTREME technologies [7]. The setup is shown in figure 1.3. The energy monitor consists of a zirconium filter, two EUV multilayer mirrors and a UV sensitive diode. Zirconium blocks visible and near UV radiation, but has a transmission window in the EUV region, from approx. 7 to 17 nanometers. This can be seen in the theoretical transmission spectrum of a 200 nm thick zirconium filter in that range (fig. 1.2). The zirconium filter is mounted into an aperture, which also ensures that the solid angle of EUV emission captured by the monitor is clearly defined. Furthermore, the filter is supposed to protect the mirrors from particle debris emitted by the plasma source (see section 1.5). The mirrors are Si/Mo multilayer mirrors with a reflection maximum at 13.5 nm.

The spectrum that the diode is exposed to is the product of the emission spectrum of the source, the transmission spectrum of the zirconium filter and the reflectivity spectra of the two mirrors. The latter two are parameters of the monitor itself and need to be known for a measurement. The bandwidth given by the mirrors and the filter do not correspond to the 2% bandwidth exactly. In order to determine absolute EUV powers, the emission spectrum of the source needs to be known. For each type of source, the spectrum in the EUV area looks very much alike. Therefore, a calibration factor can be given, so that measurements can be performed without taking into account the spectrum every time.

The components of the energy monitor suffer from degradation. On the zirconium filter facing the plasma, growth of carbon or condensation of particles can occur, resulting in increased absorption. There can also be sputtering by plasma ions, or holes resulting from the bombardment of atomic clusters, both increasing the transmission. The same things can happen to the mirrors once harmful particles have passed the filter. The diodes also suffer from degradation after a certain time of operation. In the case of a laser produced plasma, the zirconium filters were destroyed within the first few shots. Therefore the filters were relocated between the second mirror and the diode, not facing the plasma anymore. As the first mirror now faced the plasma, it continuously degraded in use. Therefore the operation times of the monitor were kept short and it was frequently recalibrated. This was done as a cross calibration at a gas discharge source with a reference monitor. The reference monitor is regularly calibrated at the EUV beam line at BESSY II at the Physikalisch-Technische Bundesanstalt [9].

1.1.3.2 Other EUV Metrology Instruments

There is another calibrated EUV energy measuring device frequently used in research. It is called Flying Circus (FC) [10]. It also uses a mirror / filter combination to get the desired spectral sensitivity. The main difference is that a curved mirror focuses the EUV radiation onto the diode. Thus the FC can be more sensitive to small EUV fluxes, but it is much harder to operate.

Apart from the EUV power emitted by the plasma, there are other parameters that can be of interest. One is of course the spectrum emitted by the plasma in the EUV range, but also in longer wavelength regions. Knowing the spectrum can give information about plasma parameters such as the temperature and the electron

density, both of which are important for the EUV emission. This information can be important for optimising the sources. Furthermore, a spectral analysis also gives insight to the amount of radiation that is out of the desired 13.5 nm emission band. Knowing the out-of-band radiation is an important factor in increasing the optics lifetime (see section1.5). For spectral analysis in the EUV region, EUV spectrometers are available. They have a transmission or reflection grating and provide spectra in the EUV range.

Another important parameter of EUV-emitting plasmas is their size. If they get too large, not all of the emitted power can be transferred through the optical imaging system onto the resist. In order to characterise the size of EUV-emitting plasmas, usually monochromatic pinhole cameras are used [11]. Meanwhile, also more advanced imaging tools for EUV plasmas, like Schwarzschild microscopes, have been developed [12].

1.2 Properties of Hot Plasmas

This section gives a brief overview of the plasma parameters that are most important for this work. For more detailed descriptions, please refer to [13, 14], for example.

1.2.1 Basic Parameters

When matter becomes hot enough that negatively charged electrons and positively charged ions coexist, it is in the plasma state. The plasma can be thought of as a mixture of two gases, the ion gas and the electron gas. It is possible that these have different temperatures. There is an electron temperature T_e and an ion temperature T_i. The equipartition times of electrons and ions, however, are less than a nanosecond for electron densities of more than 1×10^{19} cm^{-3} [13]. This is the lowest electron density important for this work, and all plasma processes considered here occur at longer timescales. Therefore the electrons and ions can be considered as being in thermal equilibrium, having the same temperature. The plasma temperature is usually given in units of electron volts. A temperature of 1 eV then means that the energy $k_B T$ is 1 eV. Thus the conversion is

$$1\text{eV} = 1.2 \times 10^4\text{K} \quad . \tag{1.3}$$

In a plasma there is an electron density n_e and an ion density n_i. The bulk plasma can be considered neutral. Therefore

$$n_e = \bar{Z} n_i \quad , \tag{1.4}$$

with $\bar{Z}$ being the average ionisation state of the ions.

The electron and ion gases have resonance frequencies, called plasma frequencies. They are defined by

$$\omega_{pe} = \sqrt{\frac{e^2 n_e}{\epsilon_0 m_e}} \quad , \omega_{pi} = \sqrt{\frac{Z^2 e^2 n_i}{\epsilon_0 m_i}} \quad , \tag{1.5}$$

with m_e and m_i being the masses of the electrons and the ions. Note that there is only one plasma frequency for a given electron density. In contrast to this, the ion gas usually contains a mixture of charge states, all having different ion plasma frequencies.

The thermal pressure inside the plasma is given by [14]

$$p_{pl} = n_i \left(\bar{Z} + 1 \right) k_B T \quad . \tag{1.6}$$

This pressure causes the plasma to expand. The expansion velocity for the plasma is the speed of sound, given by [15]

$$v_s = \sqrt{\frac{\gamma \bar{Z} k_B T}{m_i}} \quad , \tag{1.7}$$

with γ as adiabatic exponent. For monoatomic gases, it is given by $\gamma = 5/3$.

1.2.2 Thermodynamic Plasma Models

In complete thermal equilibrium, the ions, electrons and the radiation are in equilibrium. In that case, the velocity distribution of the free electrons and ions is given by the Maxwell-Boltzmann-distribution function, the excited states of bound electrons are governed by the Boltzmann distribution, and the photon spectrum follows the Planck distribution. However, the complete thermal equilibrium is merely a theoretical construct, hardly ever found in reality.

In order to model the population distributions in a plasma, the rates of all collisional and radiative processes have to be calculated. This is usually simplified by looking at the two limiting cases of very high or low density.

The high density case is called local thermal equilibrium (LTE). In the LTE, electrons and ions are in thermal equilibrium with each other, but not with the radiation. This occurs in plasmas where the photon mean free path is much longer than the collision length of the electrons. Excitation and de-excitation happen mainly by electron collisions, whereas radiative processes are of minor importance. Thus the LTE is valid for rather high electron densities, typically of the order of of $n_e > 10^{20}$ cm^{-3} [16].

For the EUV emission, the ion state distribution is of great importance. In the LTE, it is governed by the Saha equation [14]:

$$\frac{N_{m+1} n_e}{N_m} = 2 \frac{u_{m+1}}{u_m} \left(\frac{2\pi m_e k_B T}{h^2} \right)^{3/2} \exp\left(\frac{-I_{m+1}}{k_B T} \right) . \tag{1.8}$$

Here N_{m+1} and N_m are the number of ions in the charge state $m+1$ or m, n_e is the electron density, u_{m+1} and u_m are the statistical weights of the respective charge states, m_e is the electron mass, k_B the Boltzmann constant, T the temperature, h the Planck constant and I_{m+1} the ionisation potential of the mth ion.

The special case for low density is called Corona equilibrium. It gained its name from the corona of the sun, where such conditions prevail. The dominant processes here are electron impact ionisation and radiative and dielectronic recombination. The ion charge distribution can then be calculated by equating the rates of these processes. Its general features are the same as for the LTE case: the higher the temperature, the higher the dominant charge state. For temperatures of more than 30 eV, the average ion charge can be approximated as [16]

$$Z \approx \frac{2}{3} (AT)^{1/3} \quad , \tag{1.9}$$

where A is the atomic mass in amu and T the plasma temperature in eV. For $Z < 15$, the corona model is valid for electron densities below 10^{19} cm^{-3}.

1.2.3 EUV Emission

The research for EUV emitter materials concentrates on three elements: lithium, tin and xenon. The Li^{2+} ion displays a strong emission line for the $2p - 1s$ transition at 13.5 nm and therefore seems suitable as an emitter. The line emission also leads to a certain spectral purity of the produced EUV radiation. Handling lithium, however, can be very problematic. It is known to be chemically very reactive.

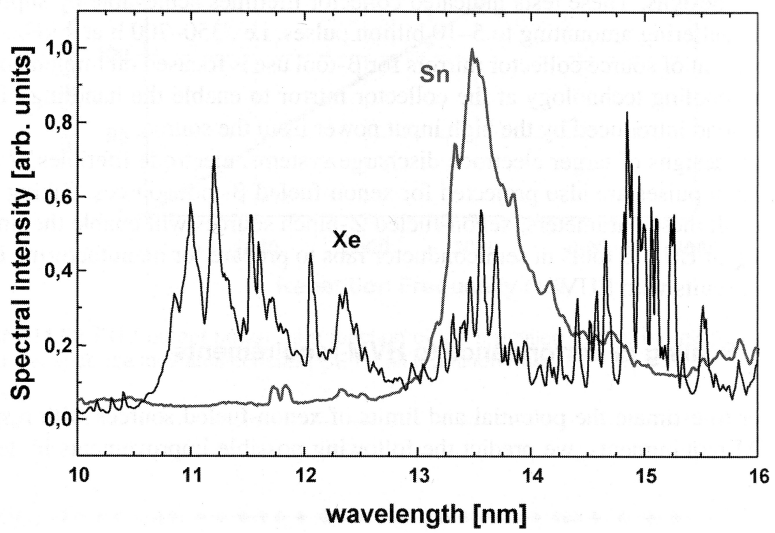

Figure 1.4: EUV spectrum of xenon and tin. These spectra were taken at a Z-Pinch GDP source [17].

Heavier elements do not display simple line emission anymore. For them, the EUV yield scales with the atomic number [18]. The highest EUV yields are to be expected of elements with an atomic mass around 52. These are tin, antimony, tellurium, iodine and xenon. Chemical considerations make only tin and xenon suitable candidates for EUV emitters. Fig. 1.4 shows experimentally recorded EUV spectra of tin and xenon. Tin (mass number 50) displays an unresolved transition array (UTA) around 13.5 nm. All ionisation stages from Sn^{5+} to Sn^{13+} contribute to it [19, 20]. For xenon (mass number 54), the same UTA can be seen around 11 nm. At 13.5 nm the emission is much weaker. It is caused by $4d - 5p$ transitions in the Xe^{10+}-ion [21, 22, 23]. Although xenon has a lower EUV yield than tin and is very expensive, its chemical inertness makes it very interesting as a clean plasma fuel.

Given a number of emitting ions, the most important parameter for EUV emission is the plasma temperature. The simplest approach to estimate a temperature is to consider Wien's displacement law. If the emission maximum of black body radiation is to be in the EUV range with a photon energy of 91.7 eV, the temperature needs to be about 31 eV.

More important, the temperature has to ensure that the EUV-emitting ion stages are abundant. The distribution of the ion charge states of xenon in a plasma is displayed

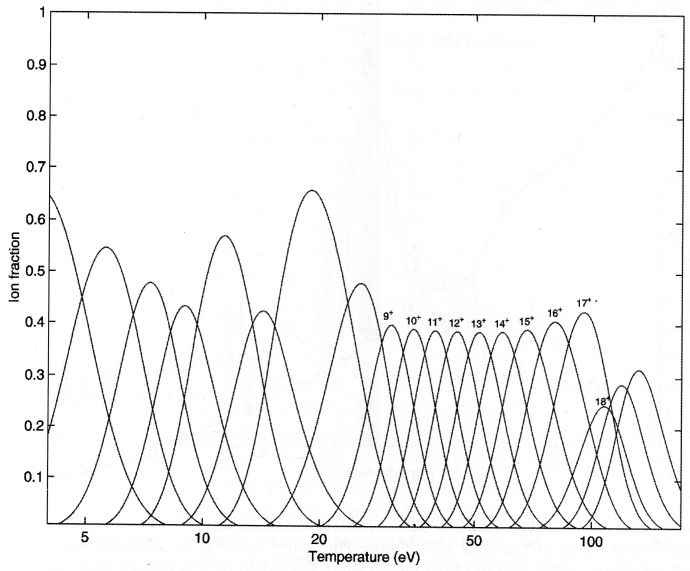

Figure 1.5: Abundance of ion states of xenon for different electron temperatures [24].

in fig. 1.5. It can easily be seen that the plasma temperature has to be about 35 eV. Only then the Xe^{10+}-ion exists. It should also be noted that for ideal conditions only about 40% of the xenon ions are in that charge state and contribute to the EUV emission.

The ion state abundances of tin are shown in fig. 1.6. As many neighbouring charge states contribute to the EUV emission, the temperature range for EUV emission is broader. However, it is best to be somewhere in the middle of the temperature range between 15 eV to 80 eV. In this range, EUV-emitting ion stages exist. The above mentioned condition of Wien's law also puts the ideal EUV-emitting temperature at 30 eV to 35 eV.

The energy required to transform one xenon atom into an ion with a tenfold charge and ten electrons is the sum of the potential and kinetic energy. The potential energy is the sum of the first ten ionisation energies of xenon, which is approx. 800 eV [25]. The kinetic energy is given by $E_{kin} = 3/2 k_B T\,(Z+1)$. For $Z = 10$ and $k_B T = 35$ eV this results in approx. 600 eV. Thus each emitting xenon ion needs to have an energy input of 1.4 keV.

It should be noted that the electrons have to be excited to emit strongly in the EUV region. The excitation of electrons to higher energies and deexcitation usually

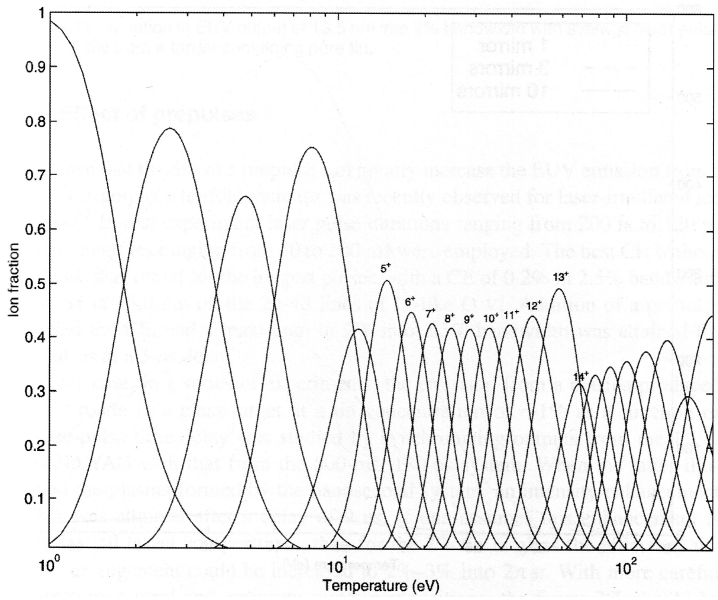

Figure 1.6: Abundance of ion states of tin for different electron temperatures [24].

happen within sub-ns timescales. Because of that, the EUV emission takes place at the same time as the energy coupling (laser absorption or gas discharge). It is not possible to heat the plasma to a higher temperature and wait for the EUV emission when the plasma has the right temperature during the cooling off. Plasma expansion and the cooling that goes along with it happens on a ns timescale, when the electronic configuration is back in the Boltzmann equilibrium.

Another important factor is the self-absorption of EUV radiation in the plasma. In the xenon case, most transitions resulting in EUV emissions are weak, therefore the probability of reabsorption is low. For lithium and tin this is not the case. In order to optimise their EUV emissions, the opacity has to be taken into account, too.

The parameter technically most important for EUV sources is the conversion efficiency (CE). It is defined as the ratio of the emitted energy in the 13.5 nm band and the total deposited energy in the plasma. Maximising the CE is one major task in EUV source development. For the xenon LPP, the highest reported number so far is a CE of 1% [26]. With tin as LPP fuel, CEs up to 2.5% [27] have been reported. A lithium-based LPP was published to have a CE of 2.5% [28]. The highest CE numbers for GDPs published so far are 1% (xenon) [26] and 2% (tin) [29].

1.3 Laser Produced Plasmas

In a laser produced plasma the energy is coupled into the plasma with a laser pulse. Laser pulses used for EUV generation typically have an energy of 0.1 to several Joules and pulse width of several nanometers.

The cold target material absorbs the laser light mostly by multiphoton ionisation. During that process, a certain number of photons can be absorbed at once and ionise an atom. The probability P_{mp} for this process to happen is [14]

$$P_{mp} = P_{sg}^{N} \quad , \tag{1.10}$$

with P_{sg} the probability for one photon to be absorbed and N the number of photons needed to get the whole ionisation energy. For xenon, the first ionisation energy is $E = 11$ eV [25]. For a laser wavelength of 1064 nm, the photon energy is 1.16 eV. Thus 10 photons need to be absorbed at once for this process. Even though this is not very probable, the high photon flux in the focus of a short laser pulse provides enough photons for these events to happen.

As the target becomes ionised, free electrons are released and inverse Bremsstrahlung absorption starts to dominate. This means that free electrons absorb photons. The energy they gained is transferred to the ions by collisions. The most crucial parameter for the laser pulse absorption then is the electron density n_e, with its resonance frequency ω_{pe}. If the electron plasma frequency equals the laser pulse frequency, the electron density is called critical density [30]

$$n_{crit} = \frac{1.1 \times 10^{21}}{\lambda_{\mu}^{2}} \mathrm{cm}^{-3} \quad , \tag{1.11}$$

where λ_{μ} is the laser wavelength in microns.

For electron densities below the critical density, the laser pulse will be transmitted through the plasma. Higher electron densities will result in a reflection of the pulse. Effective absorption of the laser pulse will only happen if the electron density is close to the critical value.

If the target is hit by a single laser pulse, most of the pulse will transmit the target. This is because the time needed to reach a good absorption level is usually larger than the laser pulse width. For a good conversion efficiency, however, the laser pulse has to be absorbed as much as possible. Thus, usually a prepulse technique is applied known

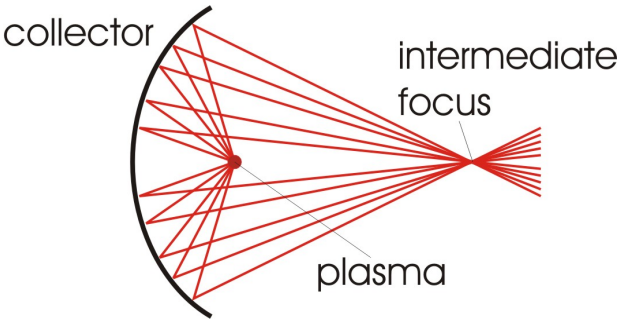

Figure 1.7: Collector setup for the LPP. The collector ideally has an elliptical shape and has a collection angle up to 2π.

from x-ray production in laser produced plasmas [31, 32]. At first, a small laser pulse hits the target. After a time delay it is followed by a large pulse. The prepulse ionises the target and forms a preplasma. The main pulse then hits the preplasma. For an optimised pulse delay, the main pulse will be absorbed almost completely.

In conclusion, it can be said that for EUV emission there are two important plasma parameters: The electron density determines the absorption of the laser pulse, and the plasma temperature governs the EUV emission. The EUV emission happens on the same timescale as the absorption of the main laser pulse. That means that the two mentioned parameters need to be optimised at the same time.

Targets being investigated are gas jets [33, 34, 35], cluster jets [36, 37], liquid jets [38] and droplets for xenon. For tin, liquid jets and various kinds of tin-containing solid targets [39] are being explored.

As there do not have to be any solid parts in the immediate vicinity of the laser plasma, a large collection angle (up to 2π) is available for collecting the EUV radiation into the intermediate focus. The collector mirrors used for that usually have an elliptical surface, one focus being the plasma and the other the IF (see fig. 1.7). They have to operate close to normal incidence; thus Si/Mo layer mirrors are used for that purpose (see section 1.1.1).

1.4 Gas Discharge Plasmas

In the GDP case, the energy is coupled into the plasma by a strong gas discharge. In order to trigger the gas discharge, the pressure between cathode and anode needs to be in a certain area determined by the Paschen curve. In order to achieve a maximum coupling at defined breakthrough conditions, the gas is preionised with a small discharge before the main discharge is triggered.

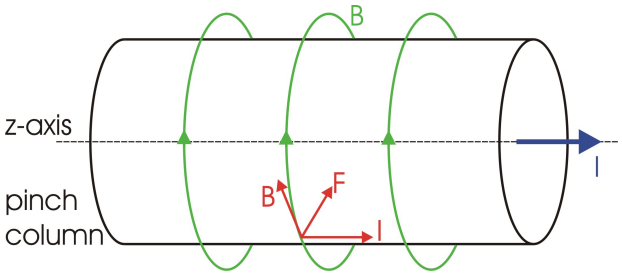

Figure 1.8: Physics of the pinch process. The plasma electrons get dragged to the z-axis, the ions follow.

For certain geometries the pinch effect can be seen: the plasma confines itself to a certain region (see fig. 1.8)[40]. To enable this process, the magnetic field pressure $p_{mag} = B^2/2\mu_0$ induced by an electrical current must be higher than the plasma pressure (see section 1.2.1). This leads to a constriction of the plasma until the two pressures are in balance [17]:

$$\frac{B^2}{2\mu_0} = (\bar{Z}+1)n_i k_B T \quad . \tag{1.12}$$

This relation can be used to estimate the plasma temperature. With the current I and the pinch radius r and using $B = \mu_0 I/(2\pi r)$, equation 1.12 yields

$$k_B T = \frac{\mu_0 I^2}{8\pi^2 r^2 n_i \left(\bar{Z}+1\right)} \quad . \tag{1.13}$$

Geometries used for the generation of EUV radiation are the Z-Pinch [17], the dense plasma focus (DPF) [21], the capillary discharge [41], or the hollow cathode geometry [42].

It should be noted that pinch plasmas usually are considerably larger than laser plasmas. They have a cylindrical shape due to the electrode geometry . As the pinch is naturally close to the electrodes, the collection angle is limited stronger than the one for the LPP. A grazing incidence Wolter collector has to be used [43, 44]. The surfaces of the collector are a combination of elliptic and hyperbolic parts (see fig. 1.9). Each EUV ray is reflected once by the hyperbolic part and once by the elliptic part. The intermediate focus is in one focus of the ellipsoid. The other ellipsoid focus is the same as the secondary focus of the hyperboloid. The plasma is in the primary hyperboloid focus. In theory, the whole scheme would work with just an elliptical surface and one reflection - the source being in one focus and the IF in the other focus of the ellipsoid. An ellipsoid alone, however, does not fulfill the Abbe sine condition and therefore has very poor imaging qualities. In addition, two reflections at smaller incidence angles are more efficient than just one reflection at a larger angle (see also fig. 1.1).

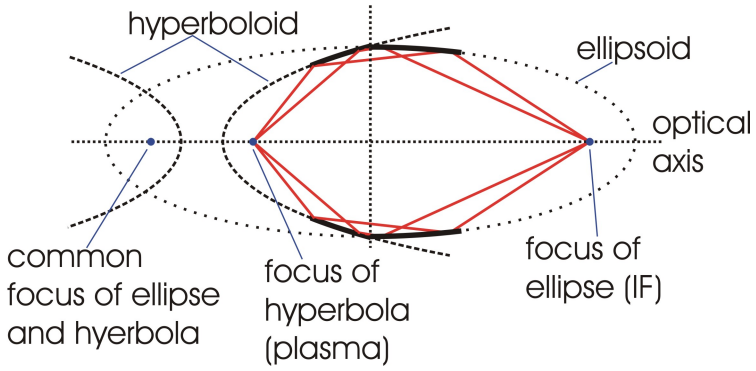

Figure 1.9: Collector design for the GDP. A single shell with a hyperbolic and elliptic part is displayed. Real collectors have up to 12 shells in order to cover the whole solid angle.

1.5 Particle Emission from Hot Plasmas and Optics Lifetime

It has long been known that, apart from electromagnetic radiation, hot plasmas emit various kinds of particles [45, 46, 47, 48, 49, 50, 51, 52]. From the plasma itself, mainly ions and electrons are emitted. But for non-gaseous targets, the shock wave induced by the plasma explosion also leads to the emission of macroscopic debris particles of the target material.

As was mentioned in section 1.2.1, the plasma expands with the speed of sound, given in equation 1.7. The sound speed for a plasma temperature of $T = 35$ eV and an average ionisation of $\bar{Z} = 10$ is 2×10^4 m/s. A xenon ion with that speed has an energy of 290 eV.

The electrons, however, expand from the plasma with a much higher speed. This creates a charge separation between electrons and ions, accelerating the ions further. This contribution to the ion acceleration is much higher than the pure kinetic effect.

For idealised conditions, an analytic expression for the ion spectrum resulting from the charge separation effect can be given. For this model, at $t = 0$, a plasma with constant temperature T, ion density n_i and ionisation $\bar{Z}$ occupies a half space. The

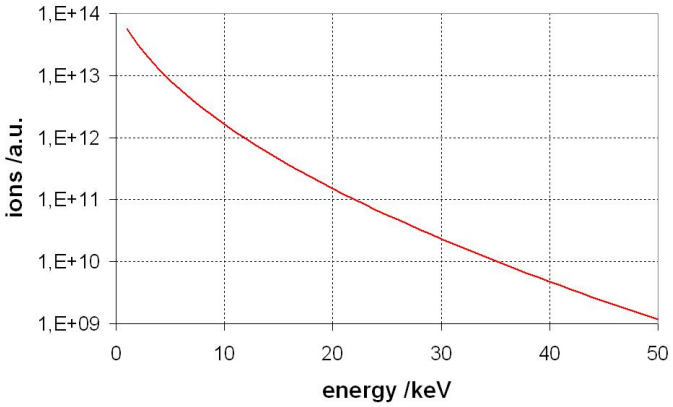

Figure 1.10: Ion energy distribution according to equation 1.14.

electron density n_e is continuous through space and follows a Boltzmann distribution. At a time t after the explosion the energy distribution is given by [53]

$$\frac{dN}{dE} = \frac{n_{i0} c_s t}{\sqrt{2 E E_0}} \exp\left(-\sqrt{2\frac{E}{E_0}}\right) \quad , \tag{1.14}$$

where $c_s = \sqrt{Z k_B T / m_i}$ and $E_0 = Z k_B T$ with Z and m_i the ion charge and mass. This formula is only valid for energies below a cutoff energy which is given by

$$E_{max} = 2E_0 \left(\ln\left(\frac{\omega_{pi} t}{\sqrt{2e}}\right)\right)^2 \quad , \tag{1.15}$$

with ω_{pi} being the ion plasma frequency.

Figure 1.10 shows the ion energy spectrum after 1 ns for a xenon plasma with the typical parameters of the laser plasma described in section 2.2. These were $T = 35$ eV, $\bar{Z} = 10$ and $n_i = 10^{20}$ cm^{-3}. It can be seen that the number of ions decreases with rising energy, for $E = 50$ keV, the ion number is already five orders of magnitude lower than for $E = 1$ keV. The energy cutoff given by equation 1.15 for these conditions is 687 keV. This value is more of theoretical interest, as the number of ions at this energy given by equation 1.14 is 18 orders of magnitude smaller than for $E = 1$ keV.

It has to be taken into account that a background gas leads to thermalisation of ions. The higher the ion charge, the higher the ion-neutral elastic scattering cross section and thus lower the mean free path. There are, however, no numbers available for the ion-neutral elastic scattering cross section of highly ionised xenon atoms. This effect shifts the energy spectrum to lower energies. Ions energies up to 20 keV have been published so far [54, 55, 56].

For EUV lithography the particle emission from the plasma is a very important issue, as it limits the lifetime of surrounding collector optics. There are several effects that are associated with particle emission from the plasma and lead to the degradation of surrounding optics:

- Particles with comparably large energies can sputter atoms off the mirror surface. This can lead to roughening of the surface and, in more severe cases, removal of the surface material.
- Particles with comparably low energies can condense on the mirror, thus building up a layer of EUV-absorbing material.
- Particles can also undergo chemical reactions with surface atoms. This is especially applicable when chemically aggressive substances are used in the EUV production process.
- In the GDP case there is a strong electron beam emitted in the direction of the optical axis. This leads to strong heating of components there, resulting in evaporation of material.

It should also be noted that high energy particles that do not hit optical components by themselves can create other freely moving particles by hitting the chamber walls or other components - an effect which is called secondary sputtering. The secondary particles can cause the same above-mentioned effects as the primary particles from the plasma.

However, particle emission from the plasma is not the only effect that can lead to optics degradation. In a gas discharge plasma, the electrodes suffer erosion due to the high thermal load they are exposed to, so particles of the electrode material are also around. These can trigger the effects mentioned above, too. In the LPP case, all solid parts can be placed several centimetres away from the plasma, minimising this problem.

As an example, the degradation of a grazing incidence mirror due to coating with a tungsten (electrode material) layer was calculated. The substrate was assumed to be nickel with a roughness of 1 nm. The coating was a 50-nm palladium layer with a roughness of 1 nm as well. The reflectivity of EUV radiation depending on the thickness of the tungsten coating and its roughness was calculated. The results are shown in fig.

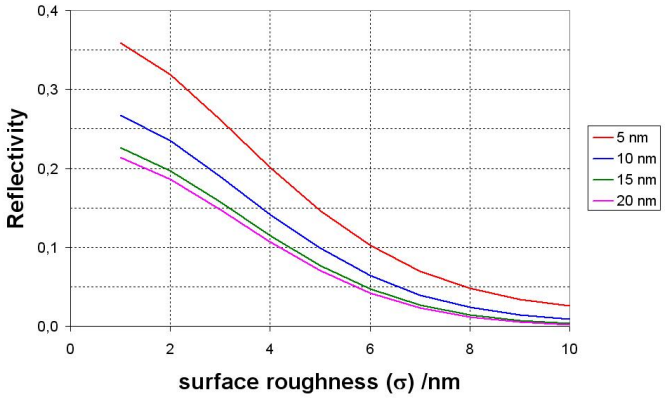

Figure 1.11: Decrease of reflectivity of a grazing incidence mirror when coated with a tungsten layer. The calculations were performed with [4].

1.11. The thickness of the tungsten layer reduces the reflectivity moderately. For layers thicker than 20 nm, no further decrease in reflectivity could be seen. The surface roughness has a stronger effect on the reflectivity. A surface roughness of 4 nm already reduces the reflectivity by about 50% in all cases. For a roughness of more than 8 nm the mirror is practically blind to EUV radiation.

Furthermore, the optical components have to withstand the electromagnetic radiation from the plasma. Only a small part of the radiation is in the desired 13.5 nm band. There is out-of-band radiation from the infrared to the x-ray range. EUV mirrors reflect infrared, visible and near UV light due to their very smooth surfaces. In the far UV and x-ray range, however, they act as absorbers, except for the reflection band at 13.5 nm [4]. X-ray irradiation can damage optical components [57]. In a high-power EUV source, the mirrors must be cooled efficiently to prevent destruction by overheating. It is also known that optical components in a vacuum under EUV exposure can become contaminated with carbohydrates, and / or their top layers can be changed due to oxidation [58, 59, 60, 61].

Naturally, the first mirror is exposed to the highest load of problematic particles and radiation. All further optical elements are not expected to have to deal with fast ions or clusters, only with contamination, oxidation and possible overheating. In general, one distinguishes therefore between collector lifetime and optics lifetime, the collector being the first mirror and optics being the rest. The specifications for the collector lifetime are much less stringent than for the optics lifetime [2]. Still, for a high-volume manufacturing tool a collector lifetime of 8×10^{10} pulses is desired.

The first approach that is used for minimising debris problems in the LPP case is the use of a so-called mass-limited target [62, 63]. A mass-limited target is a little

droplet of material that gets completely evaporated by the laser pulse. In a target that is not mass-limited, e.g. a disk of bulk target material, the plasma shock wave will eject clusters of atoms from the material. In comparison to single atoms or ions, these very large particles will cause visible craters in optical surfaces, destroying them quickly. By using the mass-limited target, all atoms that are affected by the laser pulse will actually be part of the plasma, therefore not forming any clusters. By using mass-limited targets, debris clusters can practically be eliminated. For laboratory applications, with laser repetition rates of typically around 10 Hz, mass-limited targets solve the debris problem to a great extent.

Until the work for this thesis, however, no systematic research about either the debris emission characteristics of a mass-limited target or its effects on optical surfaces at high repetition rates and consequently high doses has been published. This is rather surprising, as collector lifetime is considered one of the major technical challenges in the development of EUV lithography [5].

1.6 Scope of this Work

This thesis is concerned with xenon-based LPP and GDP sources. The main part is directed to debris emission and the resulting optics lifetime of both types of EUV sources. Additionally, the EUV emission isotropy of an LPP source was evaluated. Furthermore, the optical transmission of debris shields used for the GDP (so-called debris mitigation tools) was measured.

The thesis is set up as follows: Chapter 1 contains an introduction and the physical basics of the EUV-emitting plasma. Chapter 2 describes the experimental setup for the LPP experiments. The EUV emission isotropy experiments are described chapter 3. The fourth chapter contains debris emission and mitigation measurements for the LPP. In chapter 5, the experimental setup for the GDP source is described. Chapter 6 follows with debris emission and suppression measurements on the GDP source. In chapter 7 the transmission measurements of the debris mitigation tools (DMTs) for the GDP are reported.

Chapter 2

Experimental Setup of the Laser Produced Plasma

The principal setup consists of two main components: The laser, including the focusing optics, and the target, including the vacuum setup it is situated in. The diagnostic equipment varied widely for different experiments. It is therefore described in the respective sections.

2.1 Laser

Two lasers were used in the experiments: the ILT 500 and the ILT 2000. Both were designed by the Fraunhofer Institute for Laser Technology in Aachen, Germany [64]. They were designed with the master-oscillator power-amplifier (MOPA) architecture, displayed in fig. 2.1. A Nd:YAG oscillator couples the pulse into a pre-amplifier via a Faraday isolator. The pulse passes the pre-amplifier twice before it enters the power-amplifier. The power-amplifier is passed twice as well, and the pulse reaches its final energy. Both pre-amplifier and power-amplifier consisted of two diode-pumped amplifier modules each for the ILT 500. The ILT 2000 had twice as many amplifiers in each stage.

The repetition rate of both lasers could be varied from 1 Hz to 10 kHz. Their output power at 5 kHz could be set up to 400 W (80 mJ pulse energy) for the ILT 500, and up to 800 W (160 mJ pulse energy) for the ILT 2000. For lower repetition rates, higher pulse energies were also possible. The pulse length was 12 ns for both.

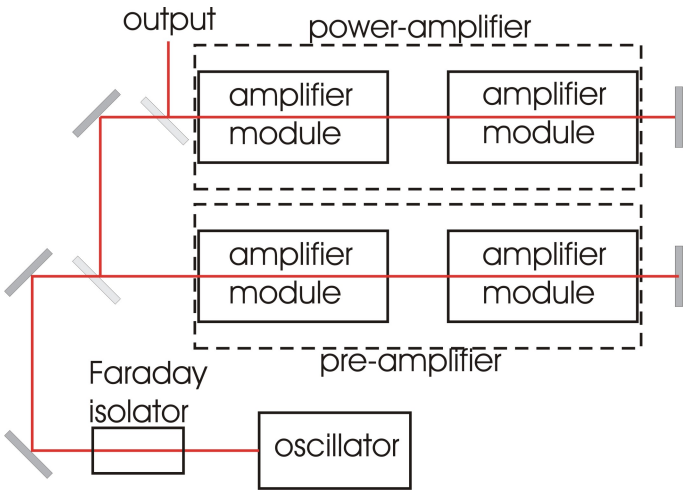

Figure 2.1: Schematic setup of the MOPA architecture of the lasers used to drive the LPP source.

The M^2 number for the ILT 500 was 2, and 11 for the ILT 2000. The wavelength was determined by the Nd:YAG oscillator to 1064 nm.

For most measurements, the ILT 500 provided a prepulse and the ILT 2000 a main pulse for the laser plasma. The ILT 500 was then set to a pulse energy of 10 % of the main pulse. The ILT 2000 was triggered with a time delay of typically 100 ns after the ILT 500 had fired. It was also possible to operate both lasers independently of each other.

The optical setup can be seen in fig. 2.2. Both lasers were focused separately onto the target, the laser beams therefore enclosing a small angle when hitting the target. Both were expanded with a telescope to a beam diameter of 5 cm. They were focused with a focusing length of 50 cm. In order to optimise emission efficiency, the main pulse was moved out of focus, so that the beam diameter matched the preplasma size.

After passing the chamber, both beams were monitored with a laser power meter. Thus it could be seen how much of the power was absorbed into the chamber.

With these parameters a conversion efficiency of 1% in 2π was achieved. Due to instabilities of the setup, the average conversion efficiency was about 0.8% in most experiments.

2.2 Target

The target was a liquid xenon jet pressed into the vacuum chamber. The vacuum chamber could be pumped with a Varian turbo pump [65] (model Turbo V 1001 Navi-

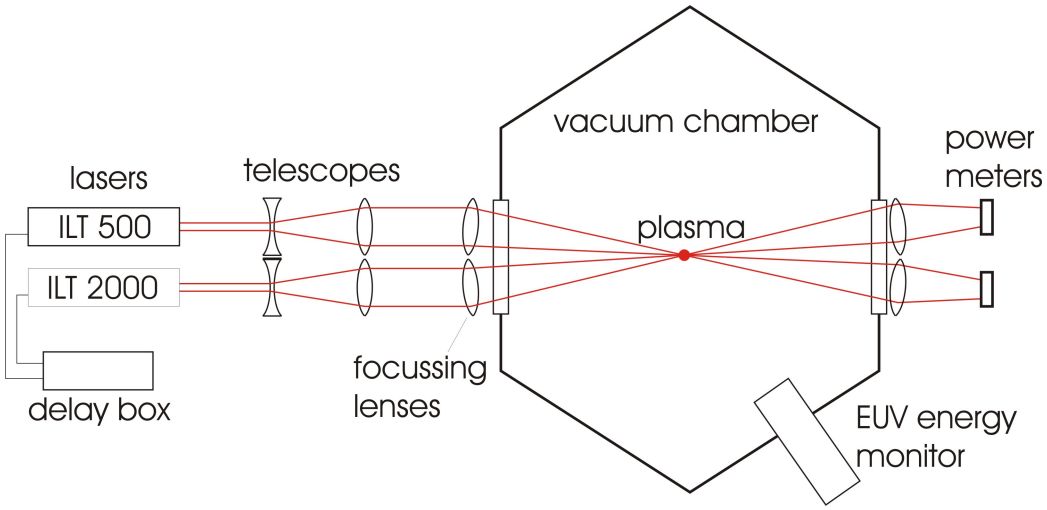

Figure 2.2: Optical setup for LPP experiments.

gator), having a pumping speed of 1050 l/s for nitrogen. As turbo pumps are not very suitable for continuously pumping heavy atoms like xenon there was also a cryo pump. It was model Cryo-Torr 10 manufactured by CTI Cryogenics [66]. Its pumping speed for air was 3000 l/s. Without jet operation, the minimum pressure in the chamber was 1×10^{-6} mbar when pumping with the with the turbo pump and to 5×10^{-7} mbar when the cryo pump was used.

The principal setup of the xenon supply into the chamber is shown in fig. 2.3. The backing pressure for the xenon jet was about 10 bar, achieved by reducing the original pressure of a xenon gas bottle. On the way from the bottle to the nozzle, the xenon was cooled down to about -105 °C and thereby liquefied. The xenon flow was controlled with a mass flow controller. The mass flows used for a typical nozzle were around 200 sccm. There were two types of nozzles used in the experiments - a capillary that narrowed down to approx. 20 μm, and a pinhole with the same size. Both nozzle types produced jets of 20 μm diameter.

It had been observed that the jet stability was higher when the xenon did not exit the nozzle directly into high vacuum. Therefore, the nozzles were designed consisting of two stages. The xenon jet entered a first small chamber of several mm length before entering the main vacuum chamber. The small chamber and the main chamber were connected with an aperture of 100 μm. In the small chamber, the pressure was several

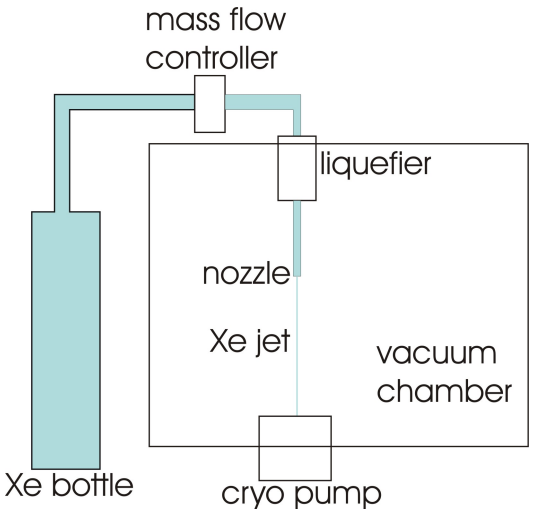

Figure 2.3: Experimental setup of the gas supply for the xenon target.

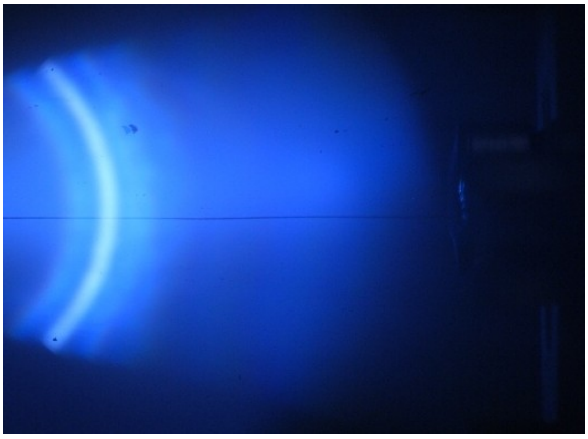

Figure 2.4: Flash lamp photograph of a xenon jet. The single jet filament can be seen as a horizontal black line. The round light part in the picture is a reflection of the flash lamp in the imaging optics.

hundred mbar, due to evaporation of xenon. This high pressure led to the formation of a stable xenon jet which then entered the high vacuum through the aperture.

The main chamber, pumped by the cryo pump, had a pressure of 3×10^{-3} mbar. Evaporation of xenon from the jet surface into the chamber led to a rapid cooling of the jet and let it freeze. The laser pulse actually hit a frozen xenon needle. An image of such a needle is shown in fig. 2.4.

The xenon volume evaporated by the prepulse was a cylinder with a height and a diameter of 20 μm. It contained 3×10^{14} xenon atoms and expanded to a sphere of 200 μm diameter within 100 ns, when the main pulse arrived. This was known from measurements of the EUV source size, as the EUV emission takes place simultaneously with the laser absorption (see section 1.2.3). The average ion density in that sphere then was about $n_i = 10^{20}$ cm^{-3}. The average ionisation state was $\bar{Z} = 10$. Thus the average

electron density was approximately $n_e = 10^{21}$ cm^{-3}. The plasma temperature was in the EUV-emitting optimum about 35 eV. These plasma conditions can be described by the LTE model (see section 1.2.2).

Chapter 3

Angular Dependence of EUV Emission from an LPP source

In the LPP case, a very large solid angle has to be collected in order to make the plasma a suitable light source for lithography. Of course, the intensity distribution of the EUV radiation across that solid angle is of great interest. Therefore it has been measured, the results being described in this chapter.

3.1 Experimental Setup

This measurement could not be performed using the standard energy monitors, as they have to be fixed to a vacuum flange and cannot be moved within an experiment. Therefore, a special detector was designed and built. It consisted of a detector head mounted on a goniometer (figure 3.1). The detector head worked in a similar way as an energy monitor, but only with one mirror inside. It was not absolutely calibrated. However, a relative measurement served the purpose of evaluating the EUV emission isotropy well enough.

The goniometer was built into the chamber with the plasma being in the centre of the goniometer half-circle. Thus the detector head could be arbitrarily moved on a sphere with a fixed distance to the plasma. It was moved by servo motors controlled by a LabView program. The definitions of the angles are shown in fig. 3.2. The detector head could be moved from 25° to 135° in the horizontal plane, and from −35° to 45° in the vertical direction (fig. 3.3).

Figure 3.1: Goniometer with detector head used for the measurement of the angular distribution of EUV emission.

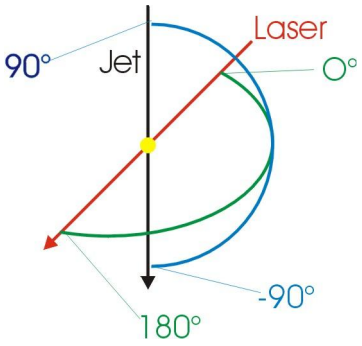

Figure 3.2: Definition of angles for the measurement of the angular distribution of EUV radiation.

Due to instabilities of the target, the laser pulse sometimes hit at the side. This resulted in an emission of EUV radiation to that side and almost none to the other. For this measurement, it had to be ensured that only central hits of the target were taken into account. This was achieved by placing an energy monitor into the plane defined by the laser beam and the xenon jet, and using it as a trigger for the detector head. If the trigger level was set high enough, then only central hits on the target triggered the measurement. Due to constraints given by the vacuum chamber, the energy monitor had to be positioned 15 ° out of that plane in this experiment. However, it showed that the triggering mechanism still worked well enough. By averaging over several shots, a reproducibility better than 5% was achieved.

By the time the measurement was performed, there was no prepulse available for the laser pulse, so the experiments were performed with a main pulse only. The laser

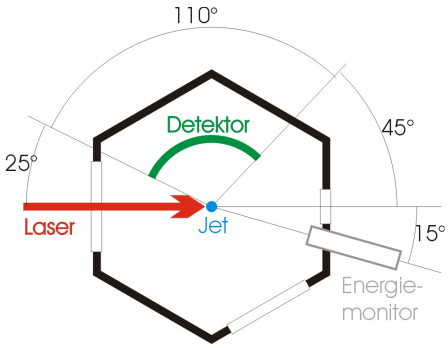

Figure 3.3: Setup for the measurement of angular EUV distribution.

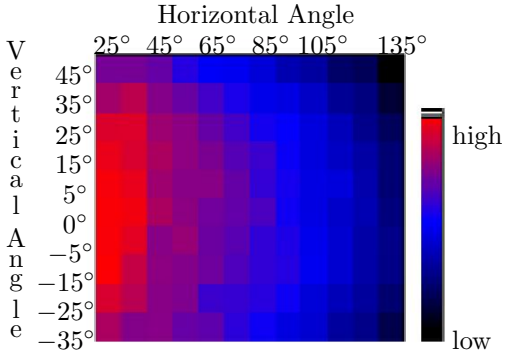

Figure 3.4: Relative EUV intensity for different horizontal and vertical angles.

being used was the ILT 500. The pulse energy was 110 mJ. In order to minimise possible effects of optics damage, the laser was operated at a low frequency of 10 Hz.

3.2 Results

At the end of the experiment, the first values were recorded again in order to check if there was any degradation in the measuring equipment. The signals measured at the end were 15% lower than at the beginning. It was assumed that this degradation was a linear function of the number of pulses, and so a correction factor was obtained for the measurements.

Data points were taken every 10° in horizontal and in vertical direction. The results are shown in figures 3.4 and 3.5. In the horizontal direction, the EUV emission is strongly dependent on the angle: the larger the angle to the incoming laser, the lower the EUV emission. For a vertical angle of 0°, the signal at 135° horizontal angle is only 44% of the signal at 25° horizontal angle. This decrease of the signal for increasing horizontal angle takes place at all vertical angles.

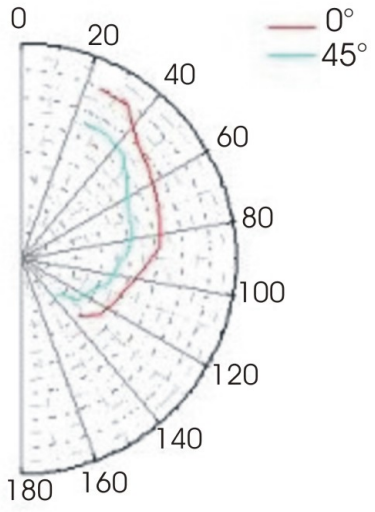

Figure 3.5: Relative EUV intensity for different horizontal angles at 0° and 45° vertical angle.

In the vertical direction, the signal maximum can be found at 0°. The larger the angle to the laser axis, the more the signal decreases. At 45°, the signal is 75% of the maximum. This decrease happens symmetrically in both directions; there is no difference between positive and negative vertical angles (figure 3.6).

3.3 Discussion

The strong anisotropy of EUV emission confirms the results that were measured in a similar setup [67]. The anisotropy can be explained by reabsorption of EUV radiation on the back side of the plasma. Obviously, the target is not transformed into a plasma across the whole jet diameter, but only on the side pointing to the laser.

For a full theoretical description, the actual size and position of the emission area and the density of the material around it need to be known. These parameters are, however, very difficult to measure. In order to give a qualitative interpretation, a geometrical model has been developed. The geometry is shown in figure 3.7. It is assumed that in the plane perpendicular to the jet, there is a circular zone of plasma with radius r_i, assumed to emit EUV. Around the plasma, there is a bigger circular zone of jet material with radius r_a, assumed to absorb EUV. The decrease of EUV intensity can be estimated by the Lambert-Beer-law

$$I \propto I_0 \exp(-\kappa d) \,, \tag{3.1}$$

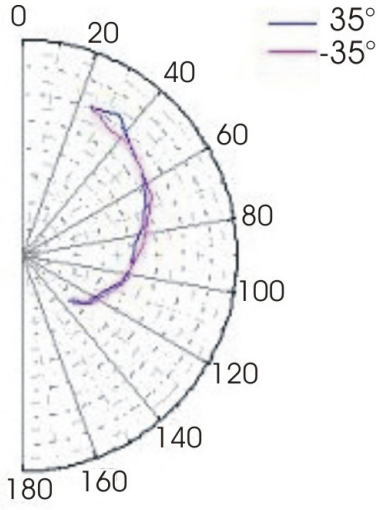

Figure 3.6: The intensity distribution is symmetrical with respect to the horizontal plane.

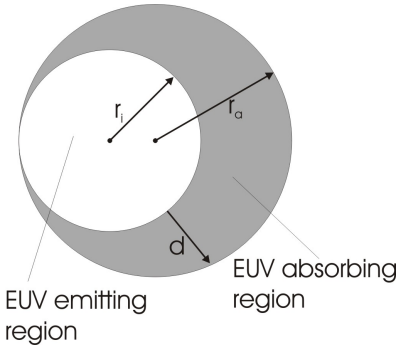

Figure 3.7: Model for the angular distribution of EUV radiation.

where I is the intensity of the EUV emission after having transmitted a distance d in the absorbing region, I_0 the intensity at $d = 0$, and κ the absorption coefficient, being proportional to the density. Assuming a constant density in the non-plasma-region, the intensity distribution behind the absorption region is dependent on the width of the absorbing layer in each direction. A straightforward, but cumbersome geometrical calculation yields

$$d = (r_a - r_i)\cos\alpha + \sqrt{r_a^2 - (r_a - r_i)^2 \sin\alpha} - r_i \ , \tag{3.2}$$

with α as horizontal angle. This results in the intensity distribution shown in fig. 3.8.

From EUV source size measurements [68], it is known that the emission region has a diameter of about 200 μm. Thus r_i was chosen to be 100 μm. The absorption of EUV in a gas atmosphere is dependent on the product of density ρ and path length.

The density is proportional to the absorption coefficient, whereas the path length is a function of $r_a - r_i$.

In order to scale the theoretical curve to the experimental results, the product $\kappa(r_a - r_i)$ had to be 0.525. This corresponds to a product $\rho(r_a - r_i)$ of 47.75 μm g/l. An estimate for r_a can be given by the expansion velocity (see eq. 1.7) of the plasma. A xenon plasma with $T = 35$ eV has an expansion velocity of 2×10^4 m/s. The pulse width was 12 ns. Taking half that time as average expansion time for the plasma particles, an expansion radius of $r_a = 120$ μm can be estimated. In that case, the gas density in the absorbing region has to be 2.4 g/l.

The anisotropy of the EUV emission shows that the standard of measuring EUV conversion efficiencies for laser plasmas is not sufficient. They are measured by energy monitors (see section 1.1.3.1) that detect only a very small solid angle. The EUV CE is then extrapolated for a solid angle of 2π. This, of course, requires isotropic emission. The experiments described in this section clearly show that this is not the case. In order to compare measured conversion efficiencies, the position of the measuring device and the angular intensity distribution need to be known.

If $f(\alpha)$ is the angular distribution function of the intensity, then the intensity can be given as $I = Af(\alpha)$ for each experiment, with A being the scaling factor for the intensity values measured in reality. The mean intensity over the full angle from 0 to π is given by

$$\bar{I} = \frac{1}{\pi} \int_0^\pi Af(\alpha)\, d\alpha \; . \tag{3.3}$$

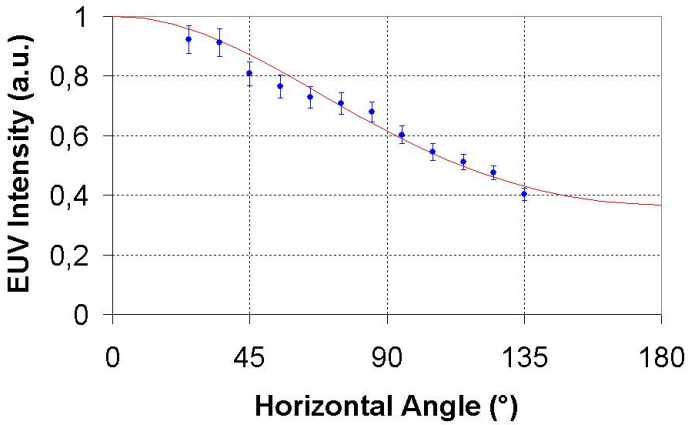

Figure 3.8: Simulated EUV distribution for 0° vertical angle (solid line) and measured values. The simulation is scaled to fit the experimental values.

The function $f(\alpha)$ is given by equations 3.1 and 3.2, yielding an integral that cannot be solved analytically. The intensity distribution for this experiment can, however, be approximated by

$$I = A\left(B\cos^2\left(\frac{\alpha}{2}\right) + 1 - B\right) , \tag{3.4}$$

with $B = f(\pi) = 0.62$. Thus equation 3.3 yields

$$\bar{I} = \frac{1}{\pi}\int_0^\pi A\left(B\cos^2\left(\frac{\alpha}{2}\right) + 1 - B\right) d\alpha = A - \frac{AB}{2} . \tag{3.5}$$

The scaling factor A can be deduced from an intensity measurement for a specific angle. If the intensity per angle I_0 is measured at an angle of α_0, then

$$A = \frac{A_0}{f(\alpha)} = \frac{A_0}{B\cos^2\left(\frac{\alpha}{2}\right) + 1 - B} . \tag{3.6}$$

With the equations 3.5 and 3.6, an EUV intensity measurement can be performed at a known horizontal angle and the average intensity over the whole angle can be deduced by it. The same formalism can be applied to a measurements of different vertical angles.

In conclusion, the EUV emission from an LPP target is highly anisotropic. These experiments were done without a prepulse for the laser plasma. Similar experiments were performed with prepulses, none of them significantly changing the intensity distribution [68]. A laser plasma used as EUV source for a lithography machine needs to display a much better emission uniformity. In order to improve this, the laser pulses need to hit the target from more than one side.

Chapter 4

Debris Emission Measurements of an LPP Source

As it was already pointed out in section 1.5, debris emission and the resulting collector lifetime is one of the key parameters in EUV technology. In this chapter, systematic measurements of the debris loads of LPP sources and possible mitigation schemes are described.

4.1 Debris and Optics Lifetime Diagnostics

4.1.1 Quartz Crystal Monitor

Quartz crystal monitors (QCMs) have been used for many years to monitor various types of deposition processes. Their key component is a quartz oscillator. When the oscillator mass changes, its natural frequency will also change. For deposition the quartz oscillator becomes heavier; thus the oscillation frequency decreases. For sputtering, the frequency increases. These frequency changes can be easily measured at a very high accuracy. For these measurements, a QCM type Intellemetrics IL 150 was used [69]. The natural frequency of the crystal was 6 MHz. Frequency changes could be measured with an accuracy of ± 5 Hz. As the natural frequency is also temperature dependent, the crystal is cooled to keep it at a constant temperature.

As this QCM was originally designed to mainly monitor deposition processes, its measuring range is mostly below the natural frequency. However, during the experi-

ment it became apparent that sputtering was the dominant process in mirror degradation, removing material and thus increasing the frequency. Therefore, on some crystals, a layer of Si or Mo was deposited to decrease their frequency and increase the range that could be measured for the sputtering case.

The conversion of the frequency changes into layer thicknesses depends on the density of the material being used. For the original gold coating, 157.1 Hz corresponds to 1 nm, for Si 17.2 Hz $\widehat{=}$ 1 nm and for Mo 81.5 Hz $\widehat{=}$ 1 nm.

When the QCM was exposed to a laser plasma, the frequency was affected by a high thermal load that could not be cooled away instantly. Electrical effects influence the measured frequency as well. So the information it gives during a running experiment could not be considered reliable. However, measuring the frequency before and after the experiment yields a frequency change that can converted into a thickness change. All measurements with the QCM were done in this manner in order to exclude any temperature effects. The information provided by the QCM can be retrieved without the need to break the vacuum, in contrast to post-exposure diagnostics described in section 4.1.2, making the QCM a very time efficient tool.

One major disadvantage of the QCM diagnostics is the fact that it usually does not consist of the same material as the collector mirror, resulting in different sputter and deposition rates and molar volumes. This discrepancy could only be resolved by depositing a multilayer mirror on the crystal. It is possible to do that, but then there would be the need to change the crystal after each experiment, thus destroying the time efficiency of the method. So the QCM was mainly used to perform relative measurements of erosion or deposition rates rather quickly.

The second drawback of the QCM method is its limitation to measuring thickness changes. When the thickness changes, the mirror degrades. This conclusion cannot necessarily be drawn in the other direction. When the thickness does not change, sputtering and deposition can be in equilibrium, altering the surface composition. This also results in mirror degradation.

4.1.2 Post-Exposure Diagnostics

In order to gain more insight into what happens with the collector mirrors, post-exposure diagnostics is essential. For these measurements, sample mirrors have been exposed to the plasma. These sample mirrors, also called witness plates, were fabricated

by the Fraunhofer Institute for Applied Optics and Precision Engineering in Jena, Germany [70]. They consisted of 40 or 60 Si / Mo bilayers on a Si substrate. The sample size was either 15 × 15 mm or 7×7 mm. The large samples were put in a special holder made of brass with an aperture that could be positioned on different parts of the plate. Therefore, up to four measurements were possible with one plate. The small plates were glued onto mounts with a smaller size. This was an improvement to the holders with apertures, as they sometimes caused brass deposition on the plates. For the small plates there were no more plasma-exposed surfaces near the mirror surface. The mirror samples could be set up in almost any position regarding the plasma.

Different post-exposure diagnostics can be performed on the samples:

- **Energy-dispersive X-ray spectroscopy (EDX):** With EDX, the chemical composition of the surface volume can be analysed. The depth of the analysis is about 1 μm. For EUV optics, this includes the whole layer system. Therefore EDX is not suitable to measure surface contamination, but the amount of Mo in the analysis volume can give evidence about erosion of layers. Being a standard tool in many electron microscopes, an EDX analysis can be done very quickly. However, for quantitative information about mirror erosion, other methods have to be used.

- **X-ray photoelectron spectroscopy (XPS):** An XPS analysis yields the chemical composition of about the top 5 nm of the sample. This surface sensitivity makes it the ideal tool for discovering contamination of the surfaces.

- **Secondary neutron mass spectroscopy (SNMS):** With SNMS, the layer system is sputtered off the sample with the sputtered atoms being analysed. This yields a depth profile of the chemical composition of the sample. The different layers can be counted, and thus information about erosion is gained. However, SNMS is a very time-consuming process and destroys the sample.

- **Small angle X-ray scattering (SAXS):** With SAXS, changes in the crystal structure can be revealed, e.g. it can be discovered how hot the sample got during exposure. For up to 30 bilayers, their number can also be detected by a SAXS analysis. In contrast to SNMS, SAXS is a non-destructive method.

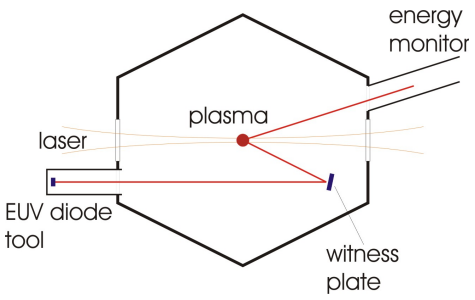

Figure 4.1: Schematic setup of in-situ reflectivity measurements.

- **Surface profilometer:** Surface profilometers can measure the profile of surfaces with an accuracy in the nm range. They can be used to measure steps between exposed and non-exposed parts of a mirror sample.

Common to all post-exposure methods is the time-consuming procedure. There is always the danger of external contamination of the samples when they are taken out of the vacuum chamber and sent to the analysis facilities. On the other hand, they can provide much more detailed information than a QCM, for example. For an understanding of the underlying processes of optics degradation, post-exposure diagnostics have to be performed.

4.1.3 In-situ Reflectivity Measurement

The most relevant parameter for EUV optics is their reflectivity. Thus it seems reasonable to monitor this property directly during the experiment. This is a more empirical approach to the subject, as a reflectivity measurement alone does not reveal anything about the mirror degradation mechanism.

For in-situ reflectivity measurements in this work, mirror samples as described in section 4.1.2 were used. The setup is shown in figure 4.1. The witness plates were placed in a defined position 10 cm away from the plasma. The reflected signal was detected with a diode tool, manufactured by Jenoptik Mikrotechnik [6]. The tool consisted of a diode - the same type as used in the energy monitors - and a zirconium filter. Additionally, an EUV reference signal was taken by an energy monitor.

As the reflection from the witness plate had to be near normal incidence, and the number of flanges in the vacuum chamber was limited, there was only one position where the in-situ reflectivity measurement could be made. It was at a horizontal angle of 50° to the incoming laser beam (according to the angle definition in fig. 3.2).

Figure 4.2: Setup for the measurement of the angular debris distribution.

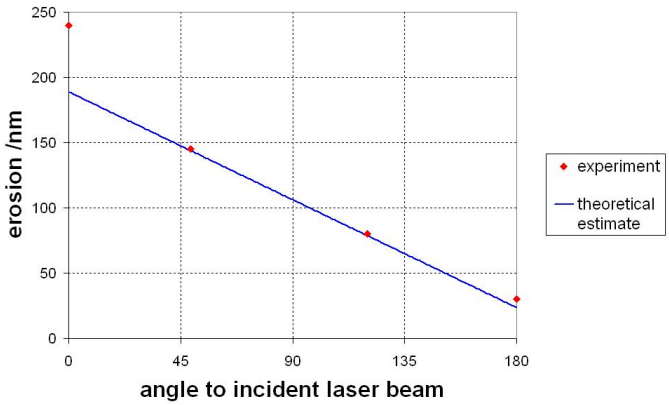

Figure 4.3: Measured erosion rates as a function of the angle to the incident laser beam and fit function.

4.2 Angular and Distance Characteristics of Debris Emission

For the measurement of angular debris distribution, four large witness plates were positioned around the plasma, all having the same distance of 10 cm to the plasma. A photo of the setup is shown in figure 4.2.

The ILT 500 (see section 2.1) was used to drive the laser plasma. It was operated with a repetition rate of 3.3 kHz, and an energy of 80 mJ per pulse. No prepulse was available at the time of this experiment. The exposure lasted 25 minutes, yielding 5×10^6 shots. The pressure in the chamber was 3×10^{-3} mbar.

The samples were first analysed with XPS to find out about contamination. It was found that the surface was contaminated with carbon and oxygen. Their amounts were,

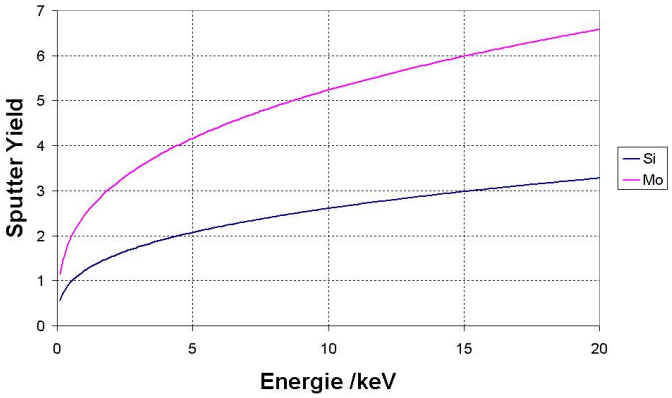

Figure 4.4: Sputter yields of Xe^{1+} ions on silicon and molybdenum [71].

however, very similar to those on a witness plate that was not exposed to the LPP. Therefore it was concluded that no significant amount of contamination was deposited on the samples during exposure.

Then the samples were analysed for erosion. As large plates were used (see section 4.1.2), step heights between exposed and non-exposed parts were measured with a profilometer. Different depths of erosion were found with these measurements. The results can be seen in fig. 4.3. The erosion is strongly dependent on the observed horizontal angle and the highest erosion is in the direction of the incoming laser beam. This is a similar angular distribution to the measured angular dependence of the EUV emission (see section 3). Thus it can be concluded that the erosion of the surface is caused by particles coming out of the EUV-emitting plasma. On the back side of the plasma there is a region of xenon gas that absorbs EUV and debris (see section 3.3).

For a quantitative description of this effect, the number of sputtering ions and atoms and their energy distribution has to be known. Since these numbers are not exactly known, only estimates can be given. The amount of ions can be estimated by the target size and the beam focus. There are approximately 3×10^{14} xenon atoms in the irradiated target. It is assumed that 50 % of them emerge as energetic sputtering ions. The energy distribution can be estimated by the distribution given in fig. 1.10. The sputter yields for xenon ions on silicon and molybdenum are displayed in fig. 4.4. With the described energy distribution, the average sputter yield is $Y_{Si} = 1.29$ for silicon and $Y_{Mo} = 2.61$ for molybdenum.

The experiments (fig. 4.3) hint that the erosion scales linearly with the angle, the number at 0° being about a factor of 8 higher than the number at 180°. It is therefore assumed that the number of emitted ions scales like this with the angle.

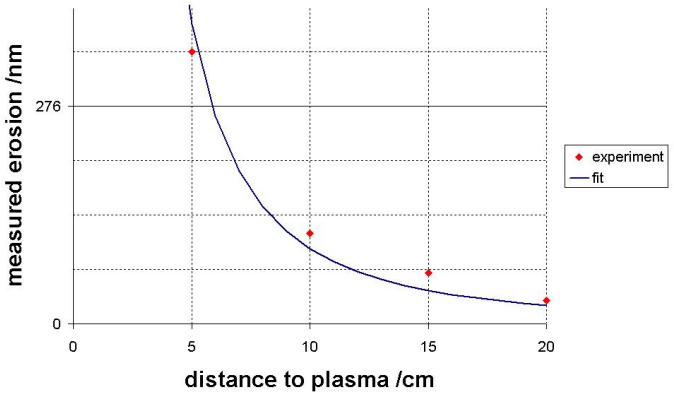

Figure 4.5: Measured erosion rates as a function of the distance to the plasma. The fit function is a $1/r^2$ function.

The mirror samples exposed an area of 20 mm^2 to the plasma. They consisted of a system of silicon and molybdenum layers, a single bilayer having a thickness of 6.9 nm. Thus, in the exposed area, there are 3.43×10^{15} silicon and 4.45×10^{15} molybdenum atoms in one bilayer. With the pulse numbers of 5×10^6 for this measurement and the above mentioned average sputter yields, theoretical erosion depths were calculated. They are displayed as fit curve in fig. 4.3. Given the simple model and the assumptions that had to be made, the theoretical curve fits the experimental data surprisingly well.

The distance characteristics of the erosion was also measured. Therefore, four witness plates were placed at different distances from the plasma, but nearly at the same angle. The results are shown in fig. 4.5. It can be seen that the erosion decreases with the distance. The data fit well with an inverse square fit. Thus it can be concluded that under these conditions there is no debris mitigation occurring between the plasma and the witness plate. The only effect is the decrease of particle density at higher distances.

The mean free path for xenon atoms was around 1 cm for the pressure regime of this experiment. Thus the vast majority of sputtering atoms should have collided with xenon atoms in the atmosphere on their way to the mirror samples. However, their sputter yield did not seem to decrease significantly by these collisions. Otherwise, the erosion should have decreased more strongly with the distance.

4.3 Debris Mitigation Systems for LPP

The measurements presented in the previous section clearly indicate that erosion is the dominant process in EUV optics degradation. Thus any debris mitigation scheme must either slow down the ions to make their sputter yield vanish, or completely prevent the ions from reaching the optics.

Several debris mitigation concepts were evaluated. As the plasma consists mainly of ions and electrons, it seems reasonable to use electric or magnetic fields to deflect the particles and thereby mitigate debris emission. One could also think of mechanical shutters that use the time delay between the arrival of light and debris emitted by a plasma. Another concept is the use of a buffer gas, slowing down the debris particles by collisions.

4.3.1 Electric Fields

Plasma emits charged and neutral particles. In theory, all charged particles can be deflected by electric fields, and thus any damage caused by them can be prevented. This is not true for neutral particles. So far, it is neither known how many neutral particles are emitted by an EUV plasma compared to charged particles, nor which of them causes the greater damage to the collector optics. The primary destruction mechanism was identified as erosion caused by sputtering (see section 4.2). Highly charged ions are known to have higher sputter efficiencies than neutral ones. However, the effect of the particle charge should only be noticed when the potential energy due to ionisation is in the same order of magnitude as the kinetic energy. In order to have a potential energy of 1 keV, the Xe ions would need to be ionised elevenfold [72]. The charge distribution of emitted ions from a comparable plasma was published to have a maximum by twofold ionisation [55]. Thus it seems highly unlikely that a major part of the ions carries enough charge to cause potential energy sputtering. For 1 keV ion charge, the sputter efficiency of xenon ions is around 1 for Si and slightly higher for Mo [71]. Therefore it is expected that atoms cause the same sputtering effect as ions.

In order to experimentally evaluate the possibilities of an electric field a plate capacitor was designed. It consisted of two copper plates that were 7 mm apart. The plates were mounted in a frame of ceramic material. All edges of the copper plates were covered with the frame in order to prevent peaks in the electric field. One copper plate was grounded, the other was set on an electric potential. The length of the capacitor

was 7 cm. The voltage supply produced a voltage up to 5 kV and could endure a current of up to 5 mA.

The higher the repetition rate of the laser, the more charged particles can be found between the capacitor plates, thus contributing to a conductivity. Therefore high voltages can only be maintained at low repetition rates. In order to prove a debris mitigating effect of the capacitor, the repetition rate should be as low as possible, so high voltages can be sustained. In the experiment, a QCM was used to detect sputtering. Therefore the repetition rate needs to be above a certain limit so that the sputtering dominates the competing deposition processes (see section 1.5).

In this experiment the repetition rate was set to 50 Hz. The QCM was placed at a distance of 10 cm from the plasma, the capacitor being between plasma and QCM. The capacitor voltage was set to 950 V, thereby producing an average current of 3.4 mA. It had strong fluctuations and had to be kept below 5 mA all the time in order to prevent voltage breakdown.

The QCM was exposed to the plasma for one hour, accumulating 1.8×10^5 pulses. The measured frequency difference was 32 Hz. Then the voltage was set to 0 V, and the same experiment was repeated. In that case the frequency difference was 28 Hz. Taking into account the accuracy of ± 5 Hz, there was no difference to be measured with and without an electric field.

The parameters for the capacitor dimensions and voltage yielded a cutoff energy of 8.3 keV (see appendix A), meaning that only ions with a higher energy should be able to transmit the capacitor. As no difference in the sputtering behaviour was measured, it can be concluded that ions with a higher energy are mainly responsible for the sputtering. One needs to be very careful with this conclusion though, as factors such as shielding effects could well reduce the effective electric field in the capacitor. But it can definitely be concluded that this capacitor setup was not suitable to reduce optics damage.

Higher voltages could probably lead to mitigation. However, it was not possible to provide them. In order to use electric fields for a commercial EUV source, it will not be possible to use parallel capacitor plates because a large solid angle has to be collected. The only possibility will be a repelling field. In order to repel charged particles instead of just deflecting them, the voltage needs to be higher by a factor of nine (see appendix A). Taking into account that the repetition rate for a commercial EUV source will have to be two orders of magnitude higher than the one used here, and that the voltage will

probably have to be one order of magnitude higher, the power supply for the electric field will have to bear a current three orders of magnitude larger than the 5 mA in this experiment. This will be a very difficult technological task.

4.3.2 Magnetic Fields

In order to test magnetic fields, a permanent magnet was designed by Linos [73]. It was built in a way that there was a homogeneous magnetic field of 0.38 T perpendicular to the flight path over a length of 8 cm. The aperture size was 8 mm. The experiment that was performed was similar to the one in section 4.3.1. The QCM was placed at a distance of 10 cm to the plasma, with the magnet between the plasma and the QCM. The plasma was operated at 200 Hz.

The QCM was exposed to the plasma for 15 minutes, accumulating 1.8×10^5 shots. The measured frequency difference was 18 Hz. After that, the experiment was repeated without the magnet. This time, the frequency difference was 48 Hz. So the magnet decreased sputtering of the QCM.

With these magnet parameters, no ions with an energy of less than 1.6 keV should have passed the magnet (see appendix B). Thus this experiment suggests that a significant part of the sputtering is caused by ions below that energy. This clearly contradicts the results of the experiment in section 4.3.1. It seems like the efficiency of the capacitor was reduced by shielding effects which do not affect magnetic fields. These results suggest that a magnetic field is a more promising approach to debris mitigation than an electric field. However, more detailed experiments with more parameter variations would have to be performed to verify the result.

Even though a debris mitigating effect was shown with a magnetic field, the work was not continued in this direction, as it seems impossible to extend the field to sizes that could protect the whole collector mirror. One can estimate, for example, the dimensions of a pair of Helmholtz-coils that would be necessary to produce a magnetic field strong enough to do that. If the collector is 10 cm away from the plasma, one can set the desired radius of the ions to 10 cm. Onefold charged xenon ions with an energy of 1 keV would require a magnetic field of 0.52 T to have that radius. In a pair of coils with $10,000$ turns each, the current would have to be 5.8 A. Assuming the coils were made of copper wire with a diameter of 0.1 mm, the power consumption of the electrical circuit would be around 37 kW. This power would have to be cooled away. The use

of a pulsed current could reduce the energy dissipation in the coils. However, pulsing these high inductivities on a kHz scale would also pose a major technical challenge.

4.3.3 Mechanical Shutters

Obviously, EUV light travels much faster than any particles emitted by the plasma. One could therefore think about mechanical devices that open a shutter for the light and then block it for the debris. For large solid angles, one could think of some kind of turning wheel that has a large optical transmission but rotates fast enough to let the spokes hit all the debris particles and keep them away from the collector mirror.

A setup like this would actually be the same as a turbo pump. As it was seen in many experiments, turbo pumps are not very suitable to pump heavy atoms like xenon. The blades will be heated up too much due to the collision of ions with them, not to mention the heating caused by the absorption of radiation. The technological task of designing a turbo pump-like device that would withstand this heating is out of range for EUV source suppliers.

4.3.4 Buffer Gases

A possible means of mitigating debris is using a buffer gas [48]. A higher gas pressure will lead to collisions of the debris particles with the gas atoms, leading to energy loss of the debris particles. Compared to an electric or magnetic field, this method has the major advantage that neutral particles will also be affected. Furthermore, it is possible to use buffer gases for large collection solid angles. The deciding question is if it is possible to find regimes where a buffer gas blocks the debris but still allows most of the EUV radiation to be transmitted.

The optimal debris mitigation results should be achieved when the emitted particles lose a maximum of energy in each scattering event. This is the case when the buffer gas atoms have similar masses as the plasma particles. In order to prevent chemical problems, it seems reasonable to choose a noble gas for the buffer. Xenon would serve these purposes ideally but has two major drawbacks: The absorption of EUV light is very high and xenon is very expensive. The better choice is argon, which is easily available, chemically inert and having a much higher EUV transmission than xenon (see figure 4.6).

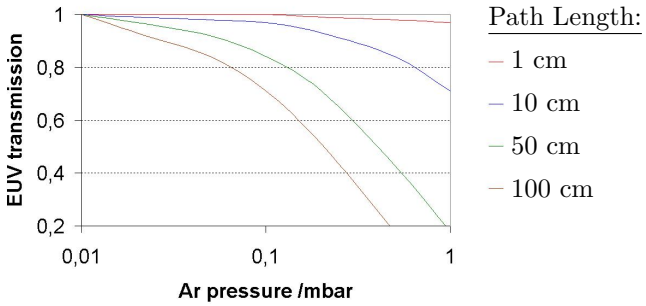

Figure 4.6: Transmission of EUV light in argon at room temperature for different path lengths [4].

The range of xenon ions in an argon atmosphere has been calculated with the SRIM software [74]. It calculates the interaction of ions in matter, modelling screened Coulomb collisions, including effects like exchange and correlation interactions in overlapping electron shells and creation of electron excitations and plasmons in the target.

The results are shown in figure 4.7. The gas densities correspond to pressures of 5×10^{-2} mbar to 1 mbar at room temperature. It should be noted that the important parameter for stopping ions is the gas density, not the pressure. This becomes especially important when the buffer gas heats up.

It is expected that the plasma emits ions with energies up to several keV. The collector is situated 100 mm away from the plasma; thus the range of all emitted ions should be below that number. In order to achieve that, the calculations indicate that the buffer gas pressure should be in the range of 3.5×10^{-7} g/cm^3, corresponding to a pressure of 0.2 mbar at room temperature (see figure 4.7). With this density, ions with an energy of less than 13 keV are stopped. The physically deciding factor for the stopping of an ion is the actual number of gas particles that the ion encounters. This number is proportional to the gas density (i.e. pressure, when the temperature is constant) and the flight path. Thus a stopping parameter α can be defined as the product of gas density and path length, or more generally, as the integral of the density over the path length:

$$\alpha = \int \rho dx \tag{4.1}$$

with ρ being the gas density and x the flight path. In order to stop ions up to 13 keV, α must equal 3.5×10^{-6} g/cm^2 or, at room temperature, 2 mbar$\times$cm. This number is valid for all geometries where argon is used as a buffer gas to stop xenon ions.

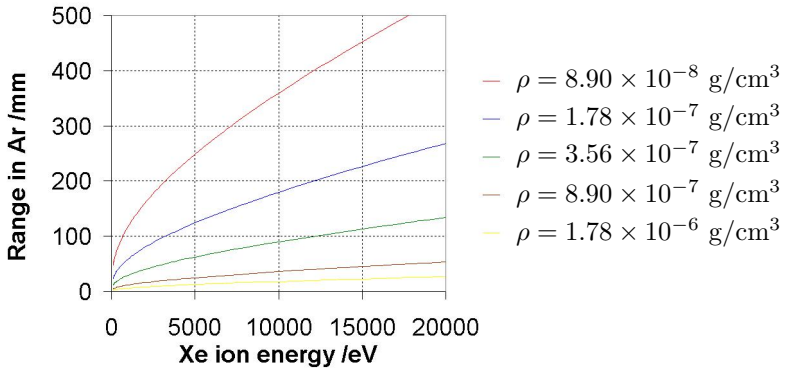

Figure 4.7: Range of xenon ions in an argon atmosphere for different gas densities.

The collector is to be placed 10 cm away from the plasma. With the above-mentioned gas density of 3.5×10^{-7} g/cm^3, the EUV transmission at that length is $T = 93\%$. Taking into account that the light needs to travel back from the collector to the intermediate focus, the absorbing path length is actually larger. For a path length of 50 cm, the transmission still is $T = 71\%$. It should therefore be possible to mitigate debris with a buffer gas while still having an acceptable EUV transmission.

Of all the mentioned debris mitigation concepts, the buffer gas seemed to be the most promising and therefore was implemented. The setup and the measurements done are described in detail in the following section.

4.4 Debris Mitigation with a Buffer Gas

4.4.1 Experimental Setup

In order to implement the buffer gas setup, the target chamber described in section 2.2 had to be modified. The biggest task was to enable argon pressures in the chamber in the range of 0.1 mbar while the xenon pressure was in the range of 10^{-3} mbar. The basic idea was to let about 100 times more argon into the chamber than xenon evaporates into it so that the partial pressures of both gases have a ratio of 100 to 1. Then it required a pump strong enough to achieve a vacuum of about 0.1 mbar under these conditions.

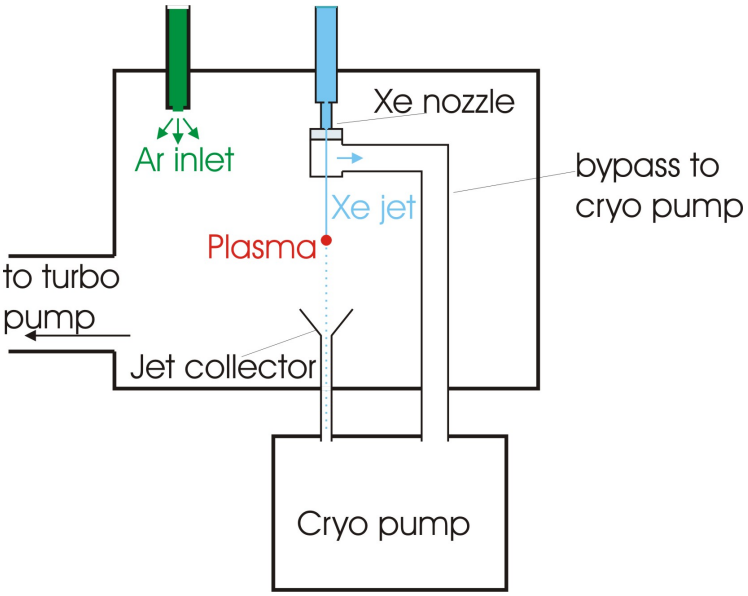

Figure 4.8: Experimental setup for buffer gas debris mitigation.

As a first step, the amount of xenon that evaporated into the chamber had to be minimised. This was achieved by setting up a differential pumping scheme in the chamber (see figure 4.8). As the xenon jet was known to freeze within the first few cm on its way in the vacuum, it was assumed that most xenon evaporated in this part. So a small chamber was constructed that the jet first entered, before leaving it through an aperture into the main chamber. This small chamber was connected directly to the cryo pump with a bypass pipe. The cryo pump was shut off from the main chamber, only leaving a small collector aperture for the xenon jet to fall into. So the cryo pump was prevented from pumping argon out of the main chamber.

The second step consisted in implementing an argon gas inlet and pumping system. The inlet simply consisted of a stainless steel pipe that connected an argon bottle with the chamber. The pumping system had to be able to pump an inlet of several standard litres of argon away while maintaining a vacuum in the range of 10^{-2} to 10^{-1} mbar. The actual gas pressure can then easily be adjusted by regulating the gas inlet. The pump used for these purposes was a Leybold [75] roots pump RUTA 5001/SP630/G. It had a pumping speed of 4510 m^3/h at a pressure of 0.1 mbar.

The laser plasma was operated at 5 kHz for these experiments. The laser power was 800 W on average, resulting in 160 mJ pulse energy. The laser was operated with

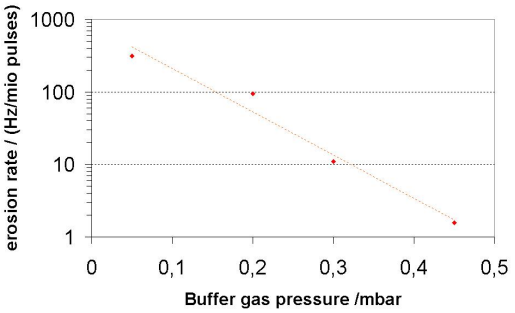

Figure 4.9: Erosion depth measured by the quartz crystal monitor for different buffer gas pressures.

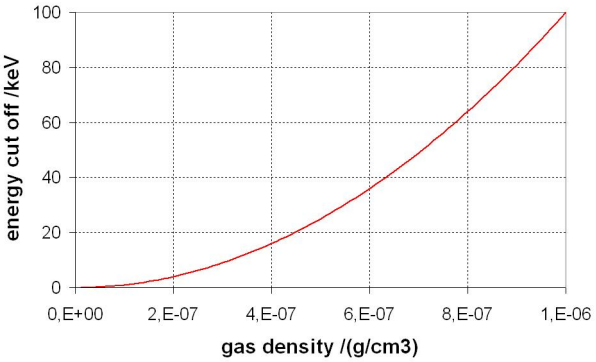

Figure 4.10: Energy cut-off limit for different gas densities.

a prepulse. The conversion efficiency was 0.8% on average, therefore the EUV pulse energy was about 1.3 mJ in 2π sr.

4.4.2 Debris Mitigation at Different Buffer Gas Pressures

Relative erosion rate measurements have been performed for different buffer gas pressures with an Si covered QCM (see section 4.1.1). The results are shown in fig. 4.9. It can be seen that the erosion rate decreases exponentially with the buffer gas pressure.

For a theoretical description of the erosion rate, a simple energy cut-off model was developed. It is assumed that a given buffer gas density stops all ions below a certain energy. That energy can be deduced from the ranges of xenon ions in an argon atmosphere (see fig. 4.7). The energy cut-off as a function of the argon density is displayed in fig. 4.10. The original energy spectrum is assumed to be the distribution displayed in fig. 1.10. The sputter yields of xenon ions on a silicon surface are given in fig. 4.4. Taking into account the distance to the plasma and the surface area of the QCM, a theoretical curve for the sputtering can be given. The results are shown in fig. 4.11. The theoretical values are generally in the same range as the experimental ones.

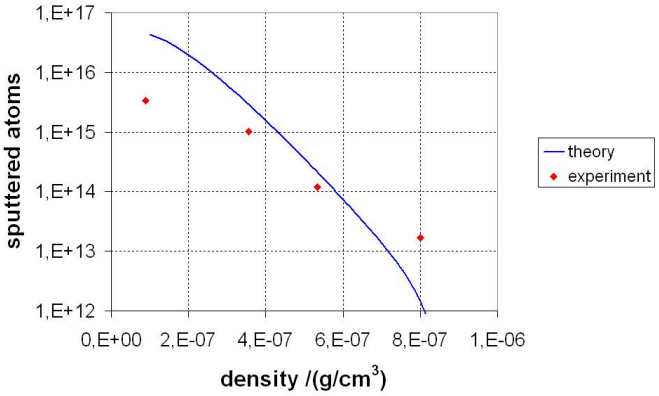

Figure 4.11: Number of sputtered atoms measured by the quartz crystal monitor for different buffer gas pressures and theoretical curve. The experimental values are the same ones as in fig. 4.9.

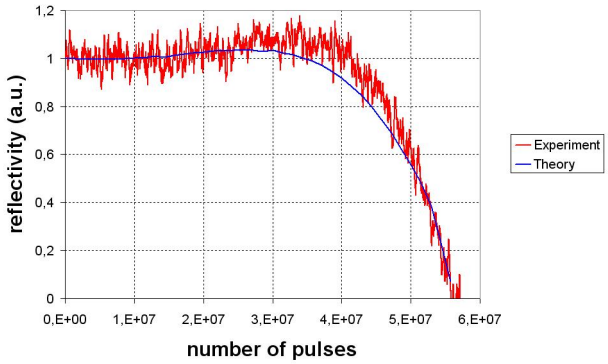

Figure 4.12: Measured reflectivity of a witness plate as a function of laser pulses. The theoretical curve is essentially the same curve as in fig. 4.13. The x values of the theoretical curve were fitted to the experimental data. Each removed bilayer corresponded to 1.46×10^6 pulses.

The predicted decrease of the number of sputtered atoms with increasing gas density, however, is stronger. A possible interpretation is that the real energy spectrum is shifted to lower energies than the one used in the calculation (see section 1.5).

In order to obtain an absolute mirror erosion rate, an in-situ-reflectivity measurement (see section 4.1.3) at a buffer gas pressure of 0.15 mbar was performed. This pressure was selected as it promised to be close to the region of interest (see fig. 4.7), but still low enough that an erosion could be detected with an in-situ measurement. The mirror sample consisted of 40 bilayers of silicon and molybdenum on a silicon substrate. Figure 4.12 shows the measured reflectivity of the mirror sample. It can be seen that the reflectivity remained nearly constant over a period of time until it suddenly dropped.

This can be explained by looking at the reflectivity curve of Mo/Si multilayer mirrors as a function of the layer number (see fig. 4.13). The reflectivity values were calculated with the on-line database *X-ray interactions with matter* [4]. The reflec-

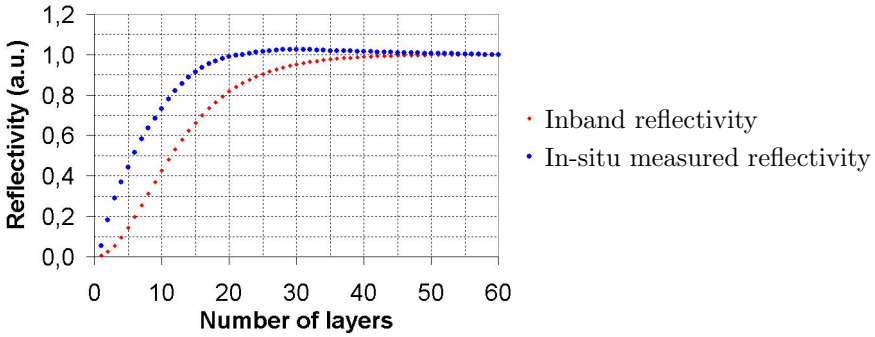

Figure 4.13: Reflectivity of an EUV mirror as a function of the number of bilayers.

tivity measured by the in-situ diode is calculated by taking into account the emission spectrum of the laser plasma, the reflection spectrum of the sample mirror and the transmission spectrum of the zirconium filter. The difference of the two curves is mainly due to the fact that the reflectivity peak of the mirror gets lower and broader when the number of layers decrease. In the in-situ measurement, the integral over the whole reflection peak is measured. However, only part of it is inband.

Assuming that the erosion rate remains constant over the time of the experiment, one can fit the reflectivity curve to the theoretical curve as a function of removed bilayers. In so doing, one can find that after 5×10^7 pulses, approximately 35 bilayers have been removed from the mirror. Each bilayer is 6.9 nm thick, which therefore yields an erosion rate of 4.8 nm/million shots. The QCM value for $p = 0.15$ mbar, taken from the exponential fit in fig. 4.9, is 106 Hz/million shots. Comparing these numbers, a factor of 21.9 Hz frequency change per nm mirror erosion can be given for this experimental setup.

The lifetime of a collector mirror can be estimated from the data presented as follows: It is assumed, as mentioned before, that the erosion rate remains constant. From fig. 4.13 one can make the assumption that a multilayer mirror needs at least 20 bilayers to produce a satisfactory reflectivity. A standard EUV mirror has 60 bilayers; thus 40 can be removed. Taking into account the measured erosion rate of 4.8 nm/million pulses, the lifetime of a collector mirror is 6.4×10^7 shots under these conditions. It should also be noted that due to the slow erosion of the mirror, the surface gets con-

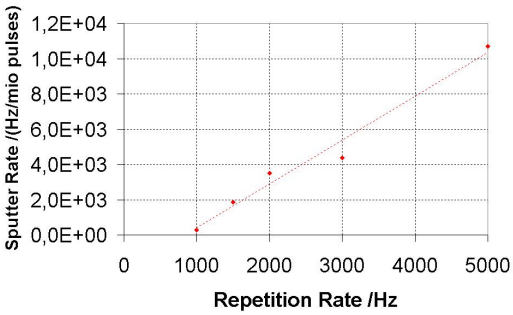

Figure 4.14: Sputter rates measured by a QCM for different laser repetition rates.

stantly renewed, and surface contamination effects therefore are not expected to play a role in mirror degradation.

4.4.3 Debris Mitigation at Different Repetition Rates

As it was mentioned in section 4.3.4, the stopping power for ions in a buffer gas atmosphere is dependent on the gas density - not the pressure - though the pressure is the parameter that is usually available for measurement. For our experiments, the gas flow rate of argon into the vacuum chamber was about 5 ln/min, meaning that 5 litres of argon at 1 bar pressure were flowing into the chamber each minute. For a pressure of 0.2 mbar, this corresponds to 2.5×10^4 l/min. The chamber had a volume of approximately 75 l, so the buffer gas in the chamber was changed completely every 0.18 s. About 70% of the laser power of 800 W was absorbed in the chamber. Taking into account that the absorbed energy is almost completely transformed into thermal energy eventually, the chamber and the buffer gas are heated with 100 J each 0.18 s. Therefore it seems reasonable to assume that temperature effects play a role for debris mitigation with a buffer gas.

Thus, sputter rate measurements for different laser repetition rates were measured. The buffer gas pressure in the chamber was chosen to be 0.1 mbar. The measurements were done with a gold covered QCM (see section 4.1.1). The results can be seen in fig. 4.14. The sputter rates are given in Hz/pulse. The discrepancies in the sputter rate to fig. 4.9 can be explained by the fact that there is a gold instead of a silicon covering on the QCM. The density of gold - and therefore the QCM sensitivity - is about a factor nine higher than the density of silicon, and the sputter rate of xenon ions on gold is a factor of about 6 to 8 higher than on silicon [71]. So one can expect a number that is a factor 50 to 70 higher for the sputter rates in this experiment than in fig. 4.9.

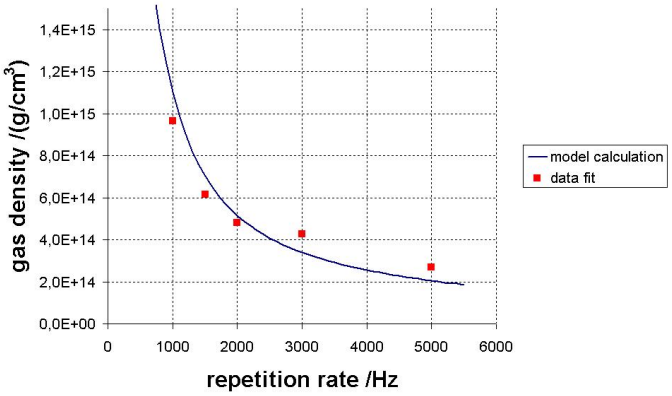

Figure 4.15: Reduction of gas density at higher repetition rates. The blue curve is calculated according to the theory described in the text; the red values are the experimental values obtained by comparison of measured sputter rates with fig. 4.9.

It can be seen that the sputter rate increases linearly with increasing laser repetition rate. As temperature effects on the QCM can be excluded due to the measurement principle (see section 4.1.1), the main effect responsible for this must be a decrease in buffer gas density for higher repetition rates.

A quantitative description of this effect can be given by following an approach originally developed by Kleinschmidt [76] for a different geometry. The chamber volume of 75 l is filled with argon at a base pressure of 0.1 mbar. That corresponds to 2.0×10^{20} argon atoms present in the chamber. With each laser pulse, an energy of 160 mJ is dissipated in the chamber. It is assumed that 10 % of that energy is deposited in fast particles that become thermalised by the buffer gas and thus heat it immediately. That results in a temperature increase of the gas

$$\Delta T = \frac{E}{3/2 N k_B} \quad . \tag{4.2}$$

For the number of argon atoms mentioned and an energy of 16 mJ, this yields a temperature increase of 4 K per pulse. The gas then expands adiabatically with

$$T V^{\kappa - 1} = \text{const} \quad , \tag{4.3}$$

κ being the adiabatic exponent of 5/3 for argon. This adiabatic expansion results in a reduction of the average gas density throughout the chamber by 2 %. The gas delivery takes place at a flow rate of 5000 sccm, which corresponds to 8.3×10^5 cm^3/s at the base pressure of 0.1 mbar. A constant gas density is achieved when the expansion and gas delivery processes are in equilibrium.

The calculated gas density decrease is displayed in fig. 4.15. The values of the experiment are also shown. They were calculated using the fit function of fig. 4.9,

taking into account a scaling factor between the two QCM measurements. Thus gas density values were calculated from the sputter rates measured in the experiments. The calculations indicate that for a repetition rate of 5 kHz, the gas density is reduced by a factor of 10 to room temperature. Assuming that $p/T = \text{const}$, a gas temperature of 3000 K can be estimated for these conditions.

4.4.4 Further Enhancement of Collector Lifetime

Based on the results presented in section 4.4.2, it was attempted to further enhance the lifetime by positioning the buffer gas inlet right next to the witness plate. Thus it was hoped that this would lead to a locally increased buffer gas density in front of the mirror sample. An in-situ reflectivity measurement was performed with an average buffer gas pressure of 0.2 mbar. The witness plate used had only 20 bilayers of silicon / molybdenum, so that changes in the number of bilayers would quickly be seen in the reflectivity measurement (see fig. 4.13). Otherwise, the parameters were the same as in the experiments described in section 4.4.2.

After 5 hours exposure (9×10^7 pulses), no decrease in reflectivity was measured. The experiment was then aborted, and the witness plate was examined with SAXS (see section 4.1.2). It was revealed that only one bilayer had been removed. This number can be extrapolated to get a number for the mirror lifetime (as it was done in section 4.4.2). A removal of 40 bilayers of a 60-bilayer mirror at the measured erosion rate leads to a mirror lifetime of 3.6×10^9 pulses. This is the highest reported mirror lifetime known to the author.

Multilayer mirror manufacturers have already successfully increased the number of layers on EUV mirrors. At the Fraunhofer Institute for Applied Optics and Precision Engineering [70] mirrors with 300 bilayers have been demonstrated [77]. Assuming that the erosion rate is the same for these mirrors, a lifetime of 2.5×10^{10} pulses can be estimated with the same argumentation as above. At a repetition rate of 5 kHz, this corresponds to a lifetime of 1400 hours or 58 days. This number is in the same order of magnitude as the collector lifetime requirements for a HVM tool (see section 1.5).

There is a potential to further increase the collector lifetime by optimising the gas flows. As it was mentioned in section 4.3.4, the path of the EUV light in an absorbing argon atmosphere is much longer than the distance of plasma and collector mirror, as the argon also fills the space between the plasma and the intermediate focus. The

aim of gas flow optimisation should therefore be to confine the buffer gas to the area between plasma and collector. The above-mentioned experiment was already a first step into this direction, as the gas pressure in the environment of the witness plate was higher than in the rest of the chamber.

Further confinement of the buffer gas might be achieved by placing a flow resistance between the plasma and the intermediate focus. The flow resistance needs to have a high optical transmission. A foil trap, similar to the ones used as debris mitigation tool in the gas discharge sources (see section 5.2) would be suitable for such a purpose.

Another possibility is the use of supersonic gas nozzles. These nozzles generate directed gas flows with very low divergence. One can think of different geometries, such as combinations of gas jets with a circular cross sections, planar gas curtains or even ring-shaped jets around the xenon jet. These geometries are feasible; in fact they were realised before in different fields of research, such as materials processing. In section 6.2, a gas curtain setup for a GDP is described, and first experimental results are presented.

Chapter 5

Experimental Setup of the Gas Discharge Produced Plasma

The GDP source used for the experiments in this thesis was a Z-pinch source. Its plasma fuel was xenon. The components can be divided into the electrical part (circuit and electrodes) and the vacuum setup.

5.1 Circuit and Electrodes

The main aim of the electrical circuit is to produce a short voltage pulse along with a high current during the discharge phase. The circuit used was an inductor-capacitor ($L-C$) inversion circuit, displayed in fig. 5.1. The pulse is transferred through the three

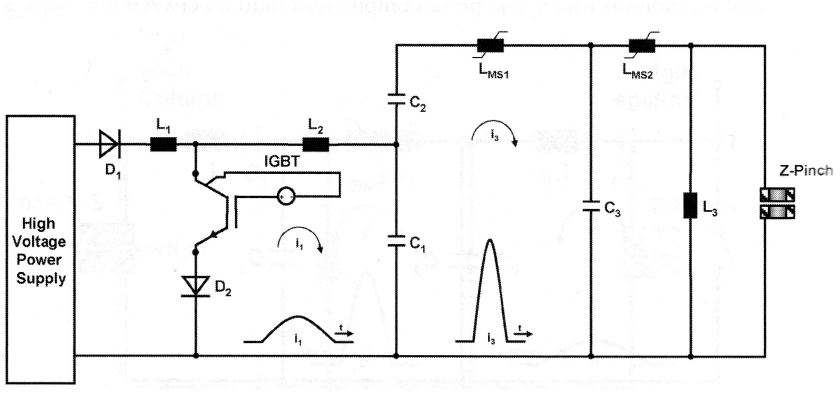

Figure 5.1: $L-C$ inversion circuit as used for the GDP source [17].

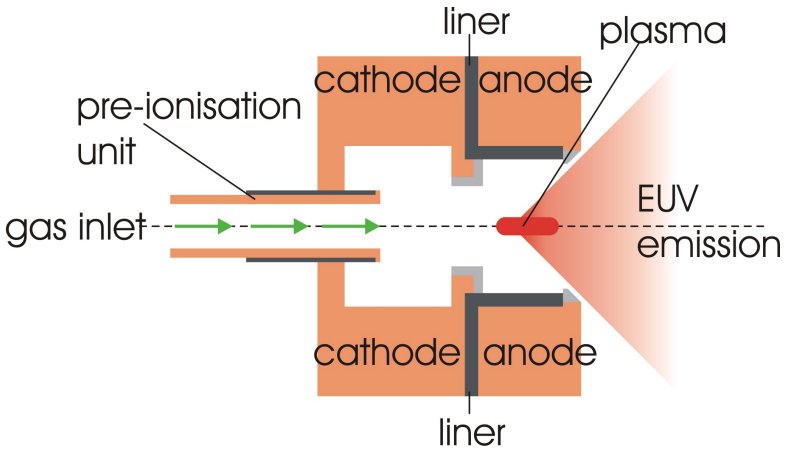

Figure 5.2: Electrode setup for the GDP source.

capacitors one after the other, thereby being compressed (for a detailed description, please refer to [17], for example). The resulting pulse was approximately 100 ns long, which is also the EUV emission time of the plasma. The breakthrough voltage was 3.7 kV for the experiments described in this thesis. Stable breakthrough conditions were achieved by a pre-ionising surface discharge prior to the main voltage pulse.

The most important part of the setup was the electrode system. Its setup can be seen in fig. 5.2. The geometry was cylindrically symmetrical around the optical axis of the system. The surface parts of both cathode and anode were made of tungsten because of its high melting point. The rest of the electrodes was made of copper, providing easy machining and a good heat conductivity. The cathode and anode were separated by the so-called liner, made of silicon nitride.

The plasma temperature of the pinch process was estimated to be about 35 eV from the extreme ultraviolet spectrum. An ion density of about 5×10^{15} cm^{-3} can be given by geometrical considerations. Assuming an average ionisation of $\bar{Z} = 10$ (see section 1.2.3), the electron density was approximately 5×10^{16} cm^{-3}. These are conditions that can be described by the Corona equilibrium model (see section 1.2.2). The EUV energy was 35 mJ in 2π sr per pulse at a conversion efficiency of 1 %. The repetition rate could be set up to 4 kHz.

For repetition rates in the kHz range, electrode cooling is a major issue. For efficient cooling, the contact area of cooling water and electrode parts need to be maximised. This was achieved with a filling of porous metal behind the copper surface. The water

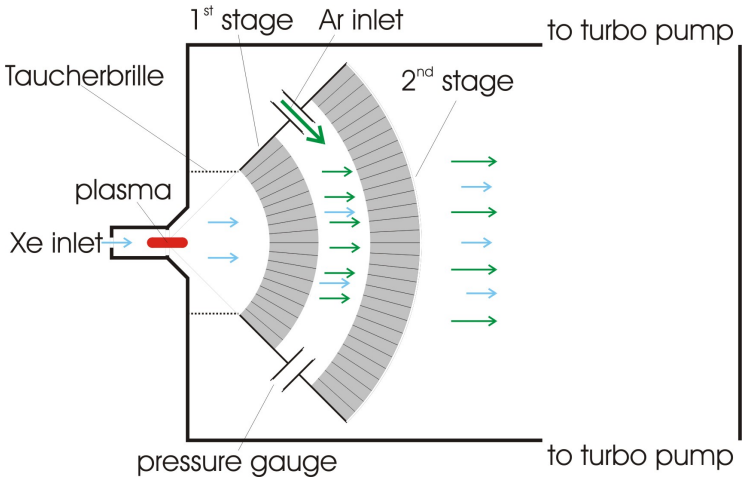

Figure 5.3: Setup of a two-stage debris mitigation tool.

pressure needed to maintain the water flow through that area was provided by a water pumping system capable of delivering up to 9 bar pressure difference.

5.2 Vacuum Setup and Debris Mitigation

The vacuum chamber was pumped by two Pfeiffer TPH 2101 P turbo molecular pumps [78], each having a pumping speed of 1400 l/s for nitrogen. Without gas flows, the turbo pumps achieved a pressure of 1×10^{-6} mbar. The xenon gas flow for source operation was 95 sccm. With this gas flow the chamber pressure was 2×10^{-3} mbar, independent of the pulse repetition rate of the source.

The GDP sources were equipped with foil traps for debris mitigation (see fig. 5.3 and 5.4) - generally referred to as debris mitigation tools (DMTs). They were designed having several hundred foils, all pointing with their narrow side to the plasma. The foils were 0.1 mm thick, the spaces in between them approximately 1 mm. As the DMTs is exposed to high thermal loads during exposure, the foils are made of molybdenum.

The foil traps acted in two ways: They acted as a flow resistance and thus enabled higher gas pressures in defined areas. They also provided a large surface for debris particles that were decelerated to get adsorbed. The foil traps generally consisted of two stages with a buffer gas volume in between them. Argon was used as a buffer gas for the same reasons as it was for the LPP sources (see section 4.3.4). The pressure in the buffer gas volume depended on the argon flow.

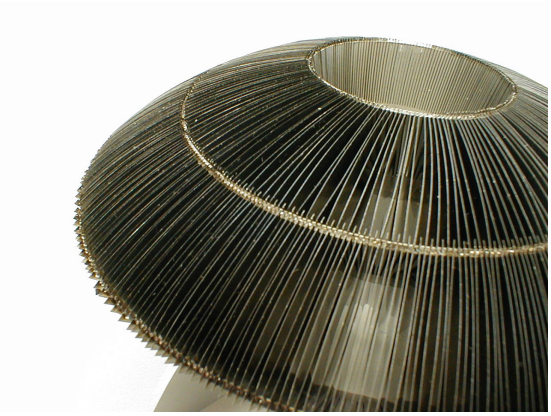

Figure 5.4: 10.5-cm debris mitigation tool.

Two kinds of DMTs were used in the experiments. The first kind was a 10.5-cm tool. It started at 6.6 cm from the plasma and ended at 10.5 cm. It subtended the whole emission angle of the source up to 45° to the optical axis in each direction.

This DMT was generally used with an additional gas confinement tube that connected the electrode area and the DMT (see fig. 5.3). This confinement tube, generally referred to as Taucherbrille (German for diving goggles), caused the xenon fuel of the pinch to be pumped away through the DMT, thereby increasing the pressure before and in the DMT. Consequently, this also increased the stopping parameter α (see section 4.3.4).

The second kind of DMT used was a prototype of a 20-cm tool - meaning that the DMT ended at a distance of 20 cm from the plasma. The prototype only covered a small solid angle, as a full solid angle DMT of this kind would not have fit into the vacuum chamber. Due to the smaller nature, the Ar gas flows for experiments with this tool were much smaller than the flows for the experiments with the short tools. There was no Taucherbrille gas confinement at the 20-cm DMT prototype. Thus the xenon fuel from the source was pumped away beside the DMT.

In comparison with the LPP, the collection solid angle is much smaller. The collector employed is a grazing incidence Wolter collector. From the debris mitigation point of view, this geometry is advantageous, as the light only has to pass once through the debris mitigation region. In the case of the LPP, it has to pass that region at least twice (see section 4.3.4). On the other hand, the foil traps used in the DMTs generate additional light absorption. The optical transmission of full size 20 cm DMT is generally about 70 % (see chapter 7).

Chapter 6

Debris Emission Measurements of a GDP Source

In this chapter, ion emission measurements at GDP sources are described. An ion spectrometer was used for these measurements. There are hardly any previous measurements of ion spectra from a GDP source known to the author. However, for EUV technology this subject has become very interesting and important. Here, the ion spectrum of a GDP EUV source was characterised for different repetition rates, buffer gas flows and hydrogen additions to the plasma fuel. Furthermore, a gas curtain setup is evaluated concerning its debris mitigation capabilities.

6.1 Ion Spectroscopy

6.1.1 Experimental Setup

For a detailed study of the ions emitted by a GDP source, a time-of-flight ion spectrometer (TOF-ESA) was used. The principal setup is shown in fig. 6.1. The main parts are a flight path, a spherical sector energy analyser (ESA) and a detector unit. The spherical sector consists of two curved copper plates with a defined voltage between them. Depending on that voltage, only ions with a defined ratio of energy and charge (E/q) will be deflected in a way that they can pass the ESA. Other ions will be either

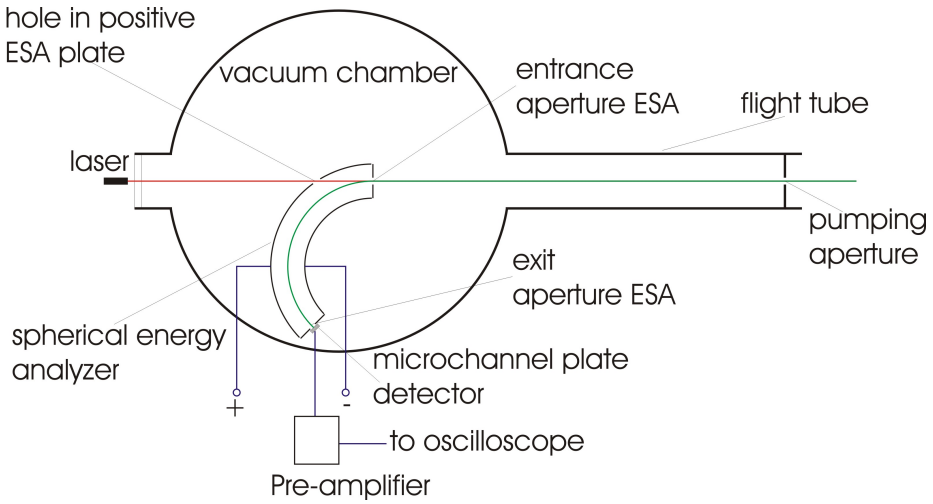

Figure 6.1: Setup of the TOF-ESA ion spectrometer. The main chamber is connected via the pumping aperture.

deflected too little or too much and eventually hit the walls of the ESA. The energy to charge ratio that passes the ESA is given by [79]

$$\frac{E}{q} = \frac{\Delta V}{r_1/r_2 - r_1/r_2} \,, \tag{6.1}$$

where E is the ion energy, q the ion charge, ΔV the voltage between the deflector plates and r_1 and r_2 are the inner and outer radii of the plates. For the spectrometer used, the values for the radii were $r_1 = 6.05$ cm and $r_2 = 4.90$ cm, and the equation yields

$$\frac{E}{q} = \frac{\Delta V}{0.42} \,. \tag{6.2}$$

The resolution of the ESA is given by [54]

$$\frac{\Delta E}{E} = \frac{\omega}{r\,(1 - \cos\phi) + \delta \sin\phi} \,, \tag{6.3}$$

with ω being the diameter of the entrance and exit aperture, r the mean radius of the plates, δ the distance from the end of the curved sector to the final exit aperture and ϕ the angle subtended by the ESA. For the device used, the parameters were $r = 5.47$ cm, $\delta = 1.07$ cm, $\phi = 160°$, and ω was variable up to 4 mm. Thus equation 6.3 reduces to

$$\frac{\Delta E}{E} = 0.009\omega\,[\text{mm}] \,. \tag{6.4}$$

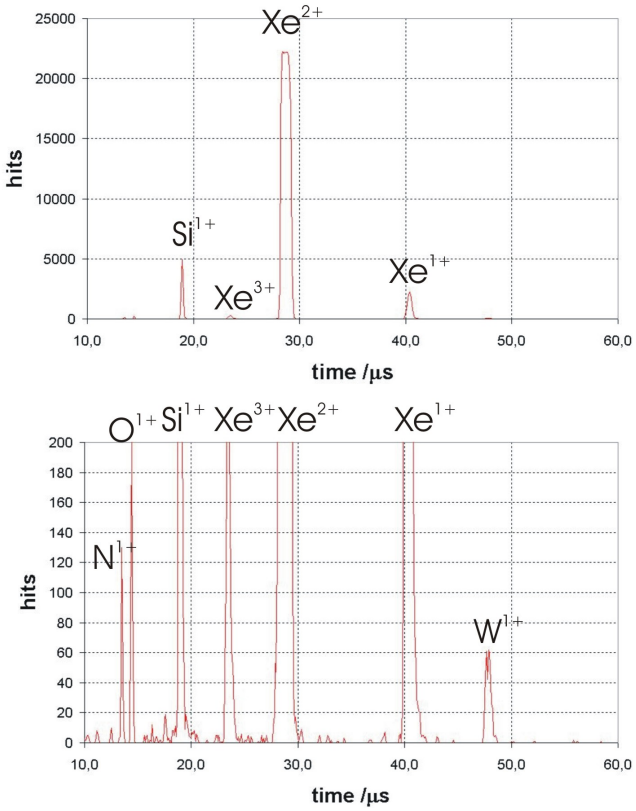

Figure 6.2: Typical time of flight spectrum as measured by the TOF-ESA. This spectrum way recorded at $E/q = 2$ keV. The lower image zooms in on the y axis.

Apertures ω used in experiments were either 1 mm or 4 mm in diameter, resulting in a resolution of $\Delta E/E = 0.9\%$ or $\Delta E/E = 3.6\%$. The small aperture resulted in a higher resolution, being especially valuable in the identification of ion species (see section 6.1.2.1). The larger aperture resulted in higher signals and therefore a higher sensitivity. This was important when operating the device with debris mitigation methods that reduced the ion signal.

The ESA acts as a filter for particles with the same ratio of energy and charge. In order to distinguish one ion from another one in the case of double the mass and double the charge, the ion detection needs to be time resolved, as a higher energy results in smaller flight times. The time resolution was achieved by the use of microchannel plates (MCPs) as detector. In this application, a matched set of two MCPs in the Chevron Geometry [80] was used. They had an electron gain of more than 4×10^6 and a rise time below 1 ns. The time-of-flight signals delivered by the MCPs were accumulated with an oscilloscope. An example of an accumulated picture can be seen in fig. 6.2.

In order to separate the signals of different ion speeds, their flight path must be as long as possible. On the experimental side, however, long flight paths pose problems regarding laboratory space, vacuum maintenance and detector adjustment. For the experiments described here, the flight path of the ions between plasma and detector was 2.20 m.

For the operation of the ion spectrometer, the mean free path of the ions needed to be much bigger than the distance they travelled. In the source chamber the pressure was $2 \ldots 3 \times 10^{-3}$ mbar during operation. The mean free path for xenon atoms in this pressure is 2 cm - much too short for the flight path mentioned above. Therefore the ESA was set up in a differentially-pumped vacuum chamber. It was pumped by a Varian V 1001 Navigator [65] turbo molecular pump with a pumping speed of 950 l/s for nitrogen. The pumping aperture to the main chamber had a diameter of 1 mm. Without opening the chamber to the source chamber, a pressure of 6×10^{-8} mbar was achieved. With an open aperture, the pressure depended on the gas flows in the source chamber, but it was always below 1×10^{-6} mbar. The mean free path for xenon at 1×10^{-6} mbar is 40 m; therefore the setup fulfilled the above-mentioned condition.

There were two possibilities for the location of the pumping aperture. The first one was at the connection flange of the main chamber and the spectrometer, 63.8 cm away from the plasma. The second one was at the end of a steel pipe leading into the main chamber, the aperture being 20 cm away from the plasma. Both were at an angle of 20° to the optical axis. As the volume behind the differential pumping aperture could be considered free of collisions, the position of the aperture actually defined the measurement position. Having the aperture 20 cm away from the plasma was the better position as the collector is supposed to be at the same distance, and so the ion spectrum could be measured at a relevant position. However, this setup was much more difficult to adjust, and a low enough pressure in the TOF-ESA chamber was more difficult to maintain. Therefore this position could not be used for all experiments.

The measurement range of the TOF-ESA was limited by two factors: For approximately 10 μs after the pinch process with the emission of the ions, there was considerable electrical noise disturbing the signal of the microchannel plates. It was not possible to adequately shield the measuring equipment to enable any measurement that short after the plasma explosion. That means that very light and very fast ions cannot be detected. The second limitation was the maximum voltage that could be applied to the deflector plates of the ESA. The maximum possible was a voltage of 6

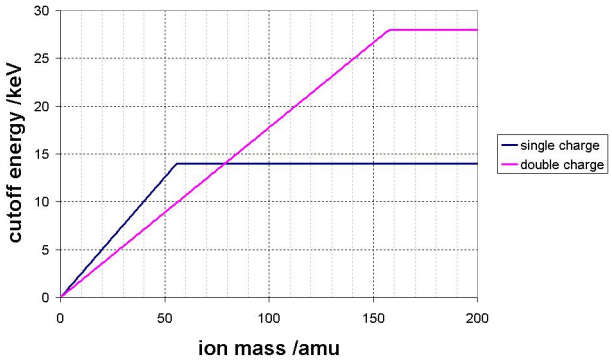

Figure 6.3: Measurement range for the TOF-ESA spectrometer for single and double charged ions.

kV. According to equation 6.2, this resulted in a maximum detectable energy of 14 keV for single charged and 28 keV for double charged ions. The combined effect of both these limitations is displayed in fig. 6.3. Xenon ions, for example, have atomic weights of around 130 amu (see fig. 6.5). For single charged ions, this yields a cutoff energy of 14 keV due to the ESA voltage limitation. Double charged ions are limited by the time barrier after the pinch to about 23 keV. This, however, does not take into account that the ESA has a finite resolution, resulting in a certain width of the peaks (see fig. 6.2). If the whole peak is to be recorded, the effective energy limit is somewhat lower. This of course is only of importance when the limiting factor is the time barrier. Thus, double charged xenon ions could be detected up to an energy of 20 keV.

The trigger to start the flight time measurement was set at the rise of the voltage at the last capacitor in the discharge circuit. As there were possible time offsets to the actual time of the ion emission, and in order to account for inaccuracies in the measured flight path, the trigger offset and the flight path were calculated by looking at two known ion signals. It was considered safe to assume that xenon ions were among the most frequent ones. So offset time and distance were calibrated by looking at the Xe^{1+} and Xe^{2+} signals for different energies.

Tests were performed to evaluate the reproducibility of results. For one case, several measurements were done with the same parameters without changing anything in between the experiments. It showed that the reproducibility of the results was 15%. This is also the number that appears in the error bars of measurements performed with the TOF-ESA.

Other tests were carried out - the spectrometer being newly adjusted to the source before each experiment. In that case, the fluctuations were much bigger. It showed that the reproducibility of the alignment is extremely low. This was due to the combination of two apertures (differential pumping aperture and ESA entrance aperture). They were about 2 m away from each other. They had to be aligned so that the ESA pointed directly into the pinch. There was an alignment laser (see fig. 6.1) that enabled the apertures to be aligned with the plasma. However, it could not be ruled out that one of the apertures cut part of the acceptance angle of the other. Furthermore, the exact position of the plasma along the optical axis could drift for several mm during longer operation (several hours).

These effects led to the conclusion that absolute measurements of ion numbers could not be performed. Measured numbers of ions could only be compared for relative measurements, where the experimental setup was not touched between the experiments. So it was not possible to correlate the number of emitted ions to measured sputter rates, or to compare the ion emission spectrum for different experiments. It was, however, possible to observe the change in distributions for variations of different source parameters. These measurements are presented in the following sections.

6.1.2 Ion Spectrum of a GDP Source

6.1.2.1 Species Identification

The first measurements performed with the TOF-ESA were aimed at the identification of ion species present in the chamber during operation. For these experiments, no debris mitigation was applied. The source was running at a repetition rate of 500 Hz. The differential pumping aperture was 63.8 cm away from the plasma. In order to achieve a high resolution of the signals, the ESA entrance aperture was 1 mm.

The ion species in the time of flight signal can be identified by looking at the flight time at a given energy value of the device. Even for careful measurements, the accuracy is not high enough to identify the ion species beyond doubt. Usually there are two or three possibilities left. Additional evidence can be provided by setting the measurement to a high time resolution and analysing the shape of the peak. The shape reproduces the isotope pattern of the ion producing the peak, convoluted with the pulse response function of the device. Examples can be seen in fig. 6.5 and 6.4. The flight time and the peak shape analysis combined made it possible to identify all observed peaks.

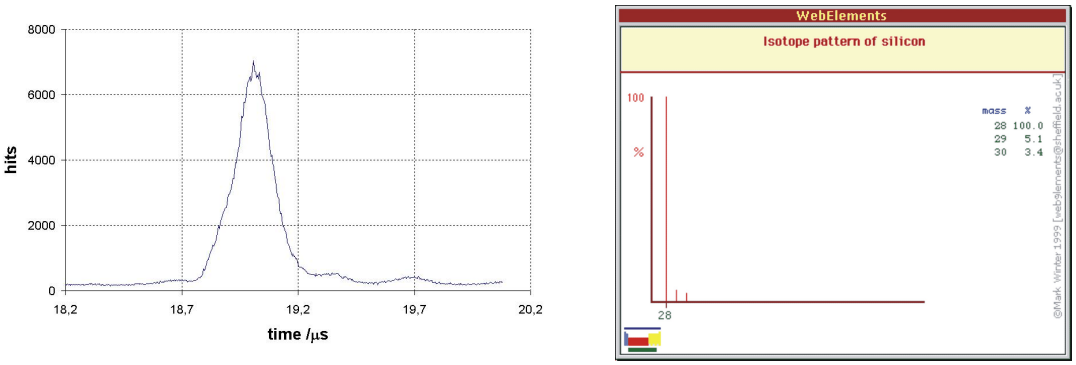

Figure 6.4: Measured signal peak for Si^{1+} (left) and isotope pattern of Si [81]. Even the two small side peaks of Si^{29} and Si^{30} can be observed in the measured signal - their integral areas also matching the ratios of the isotopes in silicon. These side peaks clearly distinguish the peak for Si and Al - the latter only having one isotope, Al^{27}.

Ions of the following atoms were detected when the source was running without any buffer gas: carbon, nitrogen, oxygen, magnesium, silicon, iron, molybdenum, xenon, tungsten and thorium. When argon as buffer gas was present, its ions could be detected, too. Carbon, oxygen and magnesium ions could only be observed with a single charge and the signals were just above the detection limit. Due to their low mass and the limitations of the TOF-ESA, they could only be observed at low energies. Carbon and oxygen were parts of residual gases present in practically all vacuums. The origin of magnesium is not known. Nitrogen and silicon could only be observed in the single charge state, too. These ions most likely originated from the liner separating the cathode and the anode. It was made of silicon nitride. Iron and molybdenum were also only detected as single charged ions. They were believed to originate from the debris mitigation tools and other hardware as well as the chamber walls. Tungsten ions appeared up to a triple charge, thorium ions up to a double charge. Both these ions could only originate from the electrodes which were made of tungsten. The tungsten contained a small addition of thorium which makes machining easier. Xenon could be observed up to a triple charge state, too. It, of course, originated from the plasma. If argon was present as a buffer gas, then single charged argon ions could be observed, too.

Even if all of the ion species mentioned could be detected in most experiments, the amount of most of them could vary to a great extent. The only reproducible numbers were the amounts of the different xenon ions. The amount of electrode and

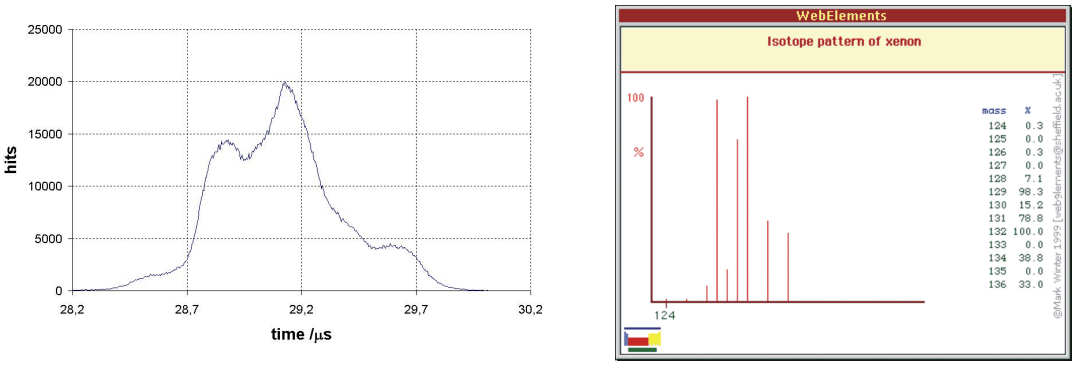

Figure 6.5: Measured signal peak for Xe^{1+} (left) and isotope pattern of Xe [81].

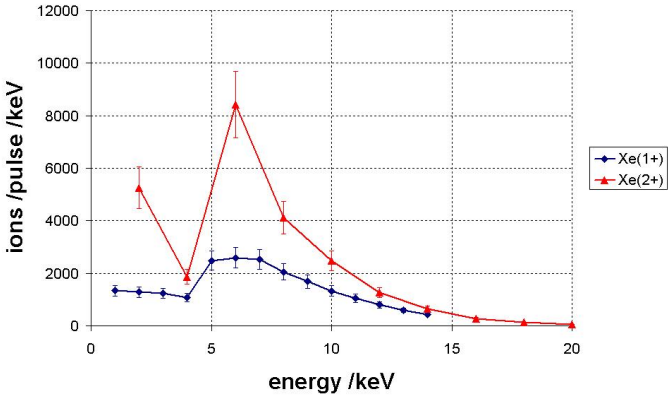

Figure 6.6: Spectrum of Xe^{1+} and Xe^{2+} ions. There was a 20 cm DMT present, and the differential pumping aperture of the TOF-ESA spectrometer was 20 cm away from the plasma.

liner material ions (tungsten, thorium, silicon and nitrogen) could differ strongly due to slight misalignments of the spectrometer, slow heating processes of the electrodes and short circuit events in the electrodes. The latter effect in particular could change the amount of the mentioned ions drastically on short timescales. The analysis of the spectra is therefore focused on the Xe^{1+} and Xe^{2+} ions.

6.1.2.2 Energy Distribution

The spectrum of xenon ions can be seen in fig. 6.6 and 6.7. For the spectrum in fig. 6.6, the differential pumping aperture of the TOF-ESA was 20 cm away from the plasma. Both Xe^{1+} and Xe^{2+} ions have their maximum at an energy of 6 keV. There are about 2.5 times more Xe^{2+} ions present than Xe^{1+}. The distribution for Xe^{1+} is much broader and decreases more slowly for higher energies.

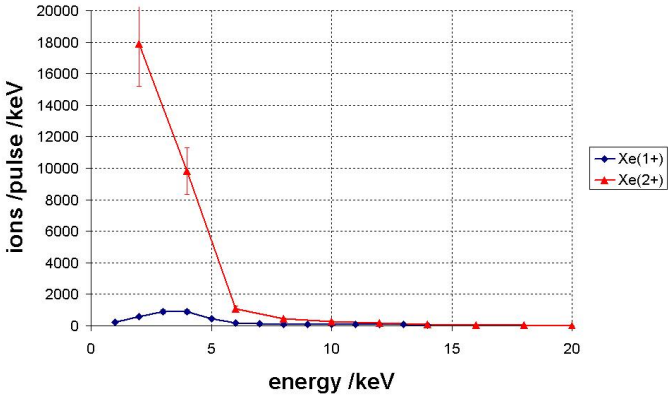

Figure 6.7: Spectrum of Xe^{1+} and Xe^{2+} ions. The differential pumping aperture of the TOF-ESA spectrometer was 63.8 cm away from the plasma.

For the spectrum in fig. 6.7, the differential pumping aperture was 63.8 cm away. The absolute numbers cannot be compared with the ones of fig. 6.6, as some other experimental parameters were different as well. The settings for the pre-amplifier were different, for example. But it can clearly be seen that the ion distribution changed due to the longer part of the flight path that was at normal chamber pressure. The Xe^{2+} distribution now has its highest value at the lowest data point taken: at 2 keV. The Xe^{1+} shifted its maximum to 4 keV. Both distributions shifted to lower energies.

It is not possible to draw conclusions about conditions in the plasma from these measurements. For the efficient generation of EUV radiation, the majority of xenon ions in the plasma needs to be ionised tenfold. That means that in the first 20 cm in normal chamber pressure, all ions carrying a charge of 4 or more become thermalised (Xe^{3+} ions can still be detected in very small quantities at low energies at 20 cm). Measuring at a longer distance than the 63.4 cm in fig. 6.7, the Xe^{2+} peak would shift further to lower energies and eventually vanish.

6.1.3 Ion Spectrum with Buffer Gas Flow

These experiments were carried out with a 20 cm DMT prototype described in section 5.2. The spectrum of Xenon ions can be seen in fig. 6.8 and fig. 6.9. Not surprisingly, the amount of ions detected decreases with increasing buffer gas flow. For buffer gas flows up to 20 sccm, a slight shift of the maximum in the energy distribution to 8 keV can be seen for Xe^{1+} and Xe^{2+} ions. Furthermore, it can be seen that the decrease in ions with increasing buffer gas flow is much stronger for Xe^{2+} ions. This can be

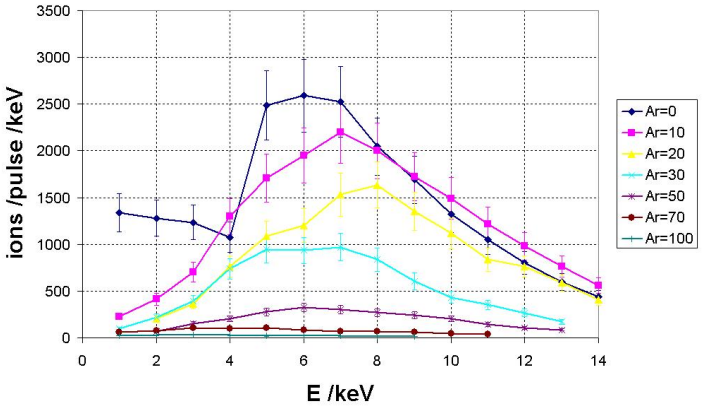

Figure 6.8: Spectrum of Xe^{1+} ions for different Ar buffer gas flows. Argon flows are given in sccm.

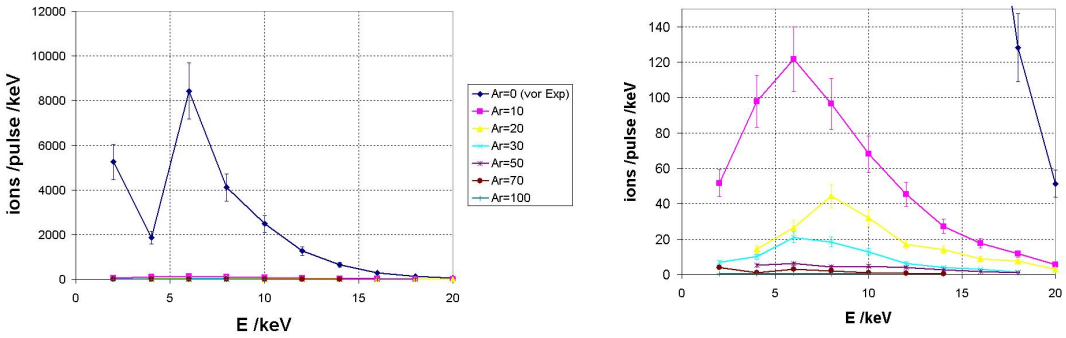

Figure 6.9: Spectrum of Xe^{2+} ions for different Ar buffer gas flows. Argon flows are given in sccm. The right image zooms in on the y-axis.

quantitatively seen in fig. 6.10, where the integrated amount of ions for different buffer gas rates is displayed. For a buffer gas flow of as little as 10 sccm, the amount of Xe^{1+} ions decreases to 84 % of its original value, whereas the number of Xe^{2+} ions drops to 2 % of its original value.

A quantitative explanation of the decrease of the total ion number can be given with a simple physical model. It is assumed that an ion that suffers a collision with a buffer gas atom loses some of its energy and at least one elementary charge. Thus, after a collision, that particle is not present in the total number of the respective ions, as the charge number is not the same anymore. If one collision is enough to eliminate

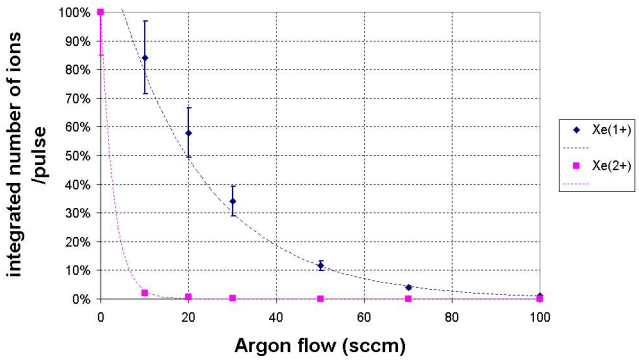

Figure 6.10: Decrease of total number of ions with increasing Ar buffer gas flow.

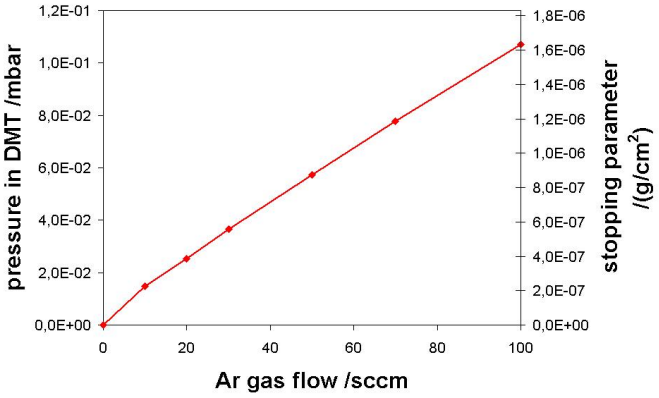

Figure 6.11: Measured pressures in the DMT centre section for different Ar gas flows. The right axis displays the calculated stopping parameters for the pressures.

an ion out of the measured number, then the total number of ions N should be an exponential function of the gas particle density n and the travelled path length x [82]

$$N = N_0 \exp(-\sigma n x) \quad , \tag{6.5}$$

with N_0 being the initial number of ions and σ the relevant cross section for the scattering of the ions in the gas atmosphere. The gas particle density n can be converted to the mass density ρ with $\rho = Cn$ with $C = M/N_A$. Here M is the atomic weight of the gas and N_A is Avogadro's number. For argon, this yields a value of $C = 6.66 \times 10^{-23}$ g for C. Equation 6.5 then turns into

$$N = N_0 \exp\left(\frac{-\sigma}{C}\alpha\right) \quad , \tag{6.6}$$

α being the stopping parameter defined in section 4.3.4.

The total number of Xe^{1+} and Xe^{2+} ions can be fitted with an exponential function (see fig. 6.10). The buffer gas flow on the x-axis is proportional to the pressure inside

the DMT (see fig. 6.11). The stopping parameters belonging to the pressure values were calculated as follows: In the centre section of the DMT, the measured pressure was assumed to be uniformly distributed, and in the lamella parts on both sides the pressure was assumed to decrease linearly to the chamber pressure. Thus the dependence of the stopping parameter α of the gas flow rate f was given by $\alpha = f \times 1.63 \times 10^{-8}$ g/(sccm cm^2). With the fit functions in fig. 6.10, this yields scattering cross sections of $\sigma = 2.0 \times 10^{-16}$ cm^2 for Xe^{1+} ions and $\sigma = 1.4 \times 10^{-15}$ cm^2 for Xe^{2+} ions.

There are no values available for the ion neutral elastic scattering cross section of xenon in argon. For argon ions in argon, however, the cross section σ is in the range of $3 \ldots 5 \times 10^{-16}$ cm^2 [83], which is in the same order of magnitude.

It can be said that the one-collision model describes the decrease of ions of a certain species fairly well. It should be noted, however, that the damage potential of energetic ions does not vanish after one collision. Energetic ions have to undergo many collisions until they are thermalised. The stopping of these ions cannot be described with the cross sections calculated here. More complex models have to be applied, as in section 4.3.4, where the ranges of xenon ions in argon buffer gas atmosphere were calculated using the SRIM code [74].

6.1.4 Hydrogen Addition to Xenon Fuel

An approach suggested by Ruzic [84] to reduce the energy of emitted ions is to add light atoms to the plasma. The ion acceleration in an expanding plasma is caused by the fast ejection of electrons. These generate an electric field that accelerates the ions. If there are light ions present, these are accelerated faster and shield the accelerating field for the heavier ions [85, 86]. This results in the light atoms carrying most of the kinetic energy, whereas the heavier ones stay relatively slow. Hydrogen is the most straightforward choice for adding light atoms to the xenon fuel of the source.

The accelerated hydrogen ions have a much less damaging effect on the optical surfaces. The sputter yield of hydrogen and xenon ions on a ruthenium surface has been calculated using the TRIM software package [74]. The results are displayed in fig. 6.12. It can be seen that the xenon sputter yield is two orders of magnitude larger than the hydrogen sputter yield. Thus, practically no sputtering is to be expected from hydrogen ions.

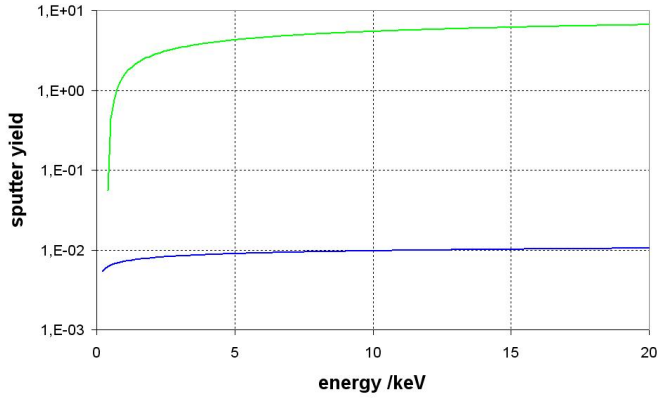

Figure 6.12: Sputter yields of xenon (green) and hydrogen (blue) on a ruthenium surface. These curves were calculated with the TRIM software package.

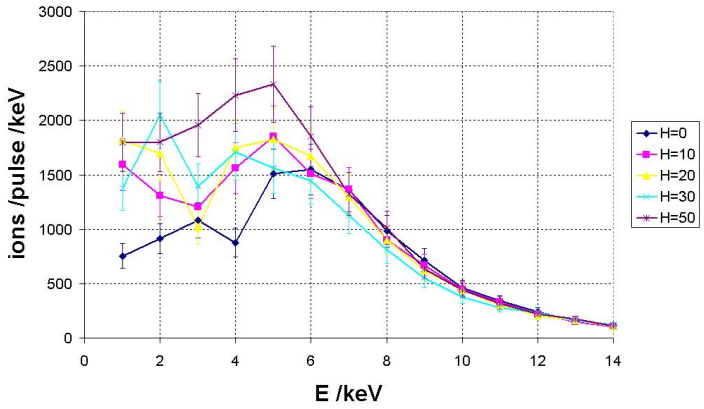

Figure 6.13: Spectrum of Xe^{1+} ions for different H_2 flows. H_2 flows are given in sccm.

In addition, hydrogen atoms in the vacuum have a cleaning effect on optical surfaces. Surfaces in a vacuum chamber are always subject to the growth of carbon layers. Hydrogen reacts with the surface carbon and forms hydrocarbons, mainly methane and ethane [87]. These are gaseous at room temperature and can easily be pumped away. Other chemical reactions are possible, too. In the chamber, however, there are relatively high temperatures and hard ultraviolet radiation present. These conditions usually lead to the cracking of bigger hydrocarbon molecules and result in the above-mentioned gaseous compounds.

For these experiments, a hydrogen flow of up to 50 sccm was mixed with the standard xenon flow of 95 sccm and used as a working gas for the pinch. The spectra of xenon ions were recorded under the same experimental conditions as the ones with

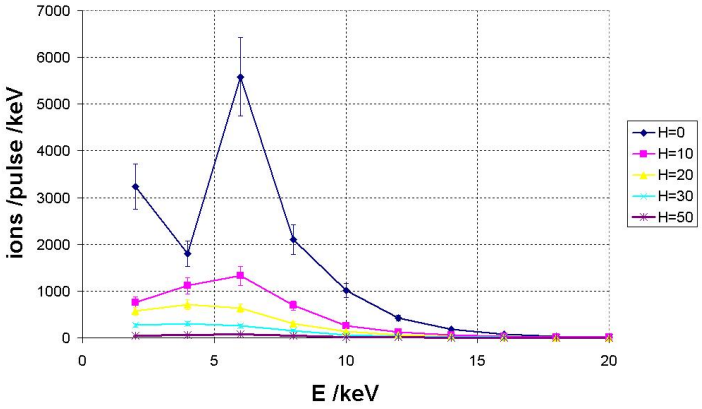

Figure 6.14: Spectrum of Xe^{2+} ions for different H_2 flows. H_2 flows are given in sccm.

different argon buffer gas flows reported in the above section - there was a 20 cm DMT present and the differential pumping aperture was at 20 cm.

The Xe^{1+} and Xe^{2+} spectra are displayed in fig. 6.13 and 6.14. For the Xe^{1+} ions, the addition of hydrogen has no effect for energies of 6 keV and more. For lower energies, however, the number of Xe^{1+} ions actually increases. This also leads to an increase of the total ion number displayed in fig. 6.15. For a hydrogen gas flow of 50 sccm, the total number of Xe^{1+} ions is 47 % higher than for no hydrogen flow.

The effect of the hydrogen addition on the Xe^{2+} ions is reverse. Their number decreases with increasing hydrogen flow. The total amount of Xe^{2+} ions decreases to 30 % for 10 sccm hydrogen flow and down to 2 % for 50 sccm hydrogen flow.

A shielding effect, as suggested above, cannot be responsible for these results, as it should reduce both the number of Xe^{1+} and Xe^{2+} ions in a similar way. As this is not the case, a different effect must be responsible for the change in the ion spectrum. It is not unlikely that neutral hydrogen atoms present in the chamber become ionised by Xe^{2+} ions. The first two ionisation energies of xenon are 11.0 eV and 20.1 eV [25], whereas the ionisation potential of hydrogen is 13.6 eV. Therefore Xe^{1+} ions cannot ionise hydrogen atoms, whereas Xe^{2+} ions are able to do so.

A similar one-collision model as in section 6.1.3 can be applied to interpret the effect. It is assumed that the charge transfer collisions take place in the pinch region. Equation 6.6 can be applied then, with $C = 1.67 \times 10^{-22}$ g for hydrogen and $\alpha = f \times 8.35 \times 10^{-9}$ g/(sccmm cm^2). With the fit function in fig. 6.14, this yields a cross

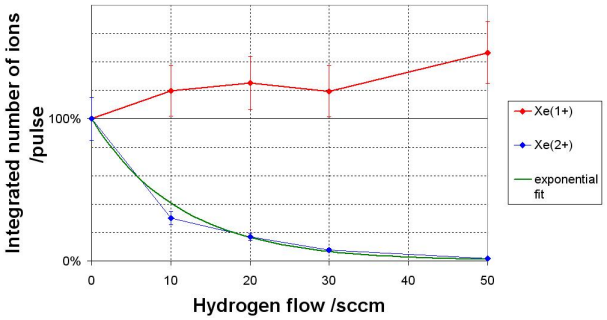

Figure 6.15: Change of total number of ions with increasing H_2 buffer gas flow.

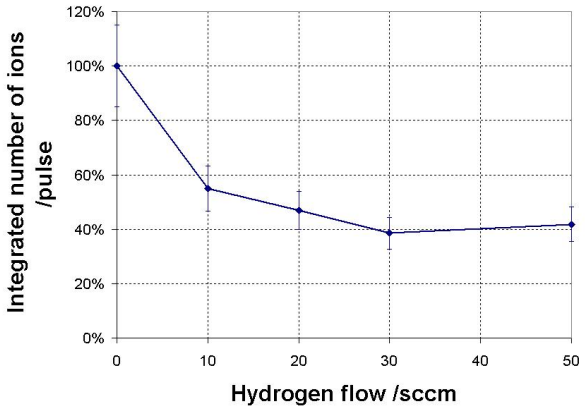

Figure 6.16: Total number of Xenon ions measured for different H_2 flow rates. H_2 flow rates are given in sccm.

section of $\sigma = 2.0 \times 10^{-15}$ cm^2. Values of the charge transfer cross section of Xe^{2+} and hydrogen reported in the literature range from 4×10^{-16}cm^2 to 2×10^{-15}cm^2 [88].

The sum of the two xenon ion species is shown in fig. 6.16. It can be seen that the hydrogen addition leads to a reduction of the total ion number measured. This clearly shows that the hydrogen addition has a debris mitigating effect.

6.1.5 Effect of Different Repetition Rates

The spectrum of xenon ions has been recorded for different repetition rates up to 3 kHz. The differential pumping aperture was 63.8 cm away from the plasma. The opening aperture of the ESA was 1 mm. There was no debris mitigation tool present.

The spectra are shown in fig. 6.17 and 6.18. In both cases the distribution itself does not change, but the signal gets stronger. The increase of the total number of ions can be seen in fig. 6.19.

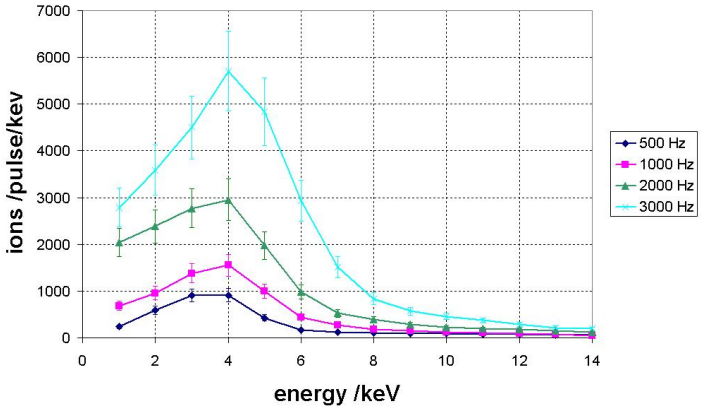

Figure 6.17: Spectrum of Xe^{1+} ions for different source repetition rates.

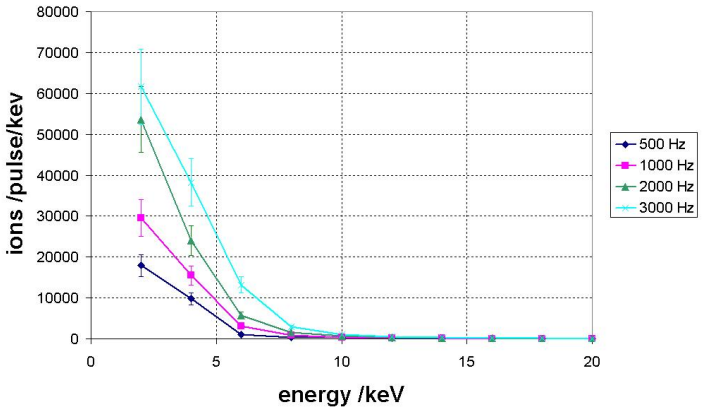

Figure 6.18: Spectrum of Xe^{2+} ions for different source repetition rates.

This effect displays an analogy to the measurements performed on a laser plasma. In section 4.4.3 it is demonstrated that higher repetition rates lead to higher sputter rates on a quartz crystal monitor. As energetic ions are the main reason for sputtering on surfaces, it is most likely that the same effect is seen here. There seems to be no reason why more ions per pulse should be emitted at higher repetition rates. The buffer gas, however, is exposed to intense heating. This leads to a decrease in density and consequently, in ion stopping power.

However, it is rather difficult to compare these results with the buffer gas measurements as it was done for the LPP case (see section 4.4.3). The experiments described here were performed without a debris mitigation tool. For the buffer gas measurements, a DMT was present. Thus the geometries were different. Furthermore, the absence

Figure 6.19: Increase of total number of ions with increasing source repetition rate.

of a DMT in the repetition rate measurements implies that only part of the ions were thermalised in the gas atmosphere. For the model described in section 4.4.3, a major assumption was that this happens to all energetic ions.

6.2 Evaluation of a Gas Curtain for Debris Mitigation

6.2.1 Motivation

A debris mitigation scheme often discussed is a gas curtain (see also section 4.4.4). Implementation of a gas curtain requires a supersonic gas flow. These have a very low divergence and thus enable a gradient in the gas pressure perpendicular to the flow direction [89].

The stopping power for fast ions and neutrals in a gas atmosphere is dependent on the stopping parameter only (see section 4.3.4). Due to the necessary optical transmission, that value is limited, and a gas curtain is not expected to change that situation very much. So a gas curtain should not be expected to improve the mitigation of fast neutrals and ions. However, in GDP sources there is considerable debris consisting of macroscopic particles - their size being in the nm to μm range. A static buffer gas atmosphere does not present an obstacle to these particles. A supersonic gas jet, in contrast, can deflect macroscopic particles, because all buffer gas atoms carry a momentum in the same direction. In combination with a foil trap, even a slight deflection of particles can lead to their stopping in the foil trap eventually.

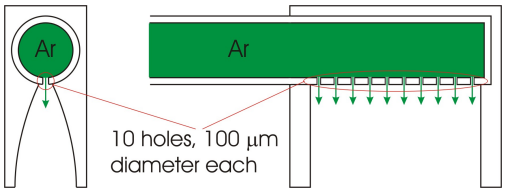

Figure 6.20: Nozzle used in the gas curtain experiments.

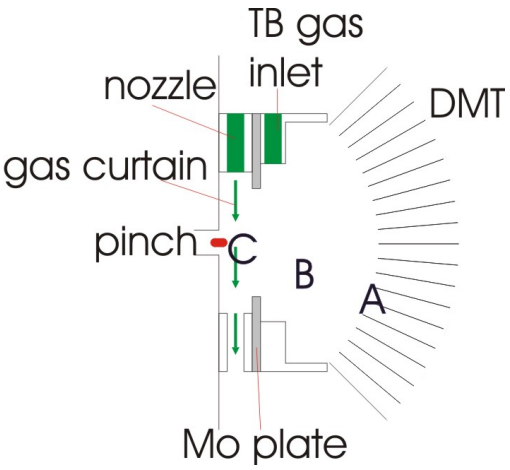

Figure 6.21: Setup for the gas curtain measurements. The points A, B and C show the measuring positions of the pressure probe.

In this section, experiments evaluating the feasibility of gas curtain setups are described. The pressure distribution has been measured around a supersonic gas jet and the spectra were recorded. The latter is important to ensure the mitigation of fast ions does not decrease when using the gas curtain.

6.2.2 Experimental Setup

The gas nozzle used in the gas curtain experiments is described in fig. 6.20. It consisted of a 6 mm stainless steel pipe that was fit into a nozzle body. The gas was fed into the steel pipe. The pipe had a row of 10 holes, each with a diameter of 100 μm, on the side. These holes led into a parabolic profile in the nozzle body. At a flow rate of 500 sccm through the nozzle, the backing pressure was 0.75 bar.

The experimental setup can be seen in fig. 6.21. The nozzle was put very close to the pinch so that the gas jet covered the whole solid angle. However, to avoid overheating, the nozzle itself was placed in the shadow of the anode plate. A short DMT (10 cm long) was used as a foil trap in combination with a Taucherbrille gas confinement (see section 5.2). The Taucherbrille had a slit on the opposite side of the nozzle so that the gas jet was pumped differentially. A molybdenum plate divided the

gas nozzle from the Taucherbrille gas inlet and provided some further confinement of the gas jet.

The pressure distribution was measured with a stainless steel capillary probe that was inserted through the debris mitigation tool into the area of interest. It was connected to a Baratron pressure meter. The pressure was measured at three different positions, shown as A, B and C in fig. 6.21. For these measurements, the source was not operating, as that would have destroyed the pressure probe.

For ion spectra measurements, the TOF-ESA device (see section 6.1.1) was used. The ion flux was measured at an angle of 20 degrees and the distance of the differential pumping aperture was 63.8 cm away from the plasma. The source was operated at a repetition rate of 500 Hz. This was low enough to ensure that there would be no damaging effects due to heating of the components, but high enough to still obtain a signal at significant buffer gas flow rates. The electrode system operation was very stable through these measurements, so that the tungsten ion distribution could be analysed for different gas flows as well (see also section 6.1.2.1). The temperature development was monitored at the molybdenum plate, as it suffered the most heat influx. The temperature was measured with a thermocouple inserted between the molybdenum plate and the nozzle holder. For these experiments the source repetition rate was gradually increased to 2 kHz. The aim was to ensure that gas curtain operation was possible at higher repetition rates as well, and that the components would not suffer damage due to overheating.

6.2.3 Pressure Distribution

Measuring the pressure distribution was necessary to verify that the nozzle indeed provided a gas jet. Otherwise it could happen that - due to turbulences - the nozzle just acted in the same way as a simple gas inlet. The pressure distribution should have a clear maximum at point C (see fig. 6.21) when the gas flows through the nozzle, and it should be evenly distributed over points A, B and C when the gas flows through the Taucherbrille gas inlet.

Fig. 6.22 shows the pressure distribution measured for an argon buffer gas flow of 500 sccm through either the nozzle or the Taucherbrille gas inlet. Additionally, there is a flow of 95 sccm of xenon through the electrode system. These are the same gas flow conditions as in a running source. The difference in pressure distributions can be

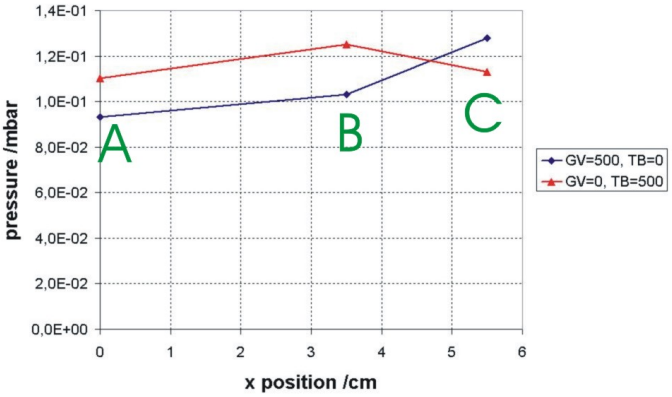

Figure 6.22: Pressure distribution measured in the Taucherbrille area for a xenon gas flow of 95 sccm and an argon gas flow of 500 sccm. TB stands for Taucherbrille gas inlet and GV for gas curtain. The data points A, B and C are the same ones as shown in fig. 6.21

.

clearly recognised. If the buffer gas flows through the nozzle, there is a clear maximum at point C. With the gas entering the Taucherbrille through the gas inlet, there is a slight maximum at point B, which is close to the inlet. However, although a pressure gradient can be measured, there seems to be potential in optimising the nozzles in order to obtain a stronger gas flow (and thus a higher gradient).

It can also be seen that the integral of the pressure over the flight path is smaller if the nozzle is used. That area, of course, represents the stopping parameter (see section 4.3.4). For the nozzle setup, these data yield $\alpha = 0.57$ mbar×cm, for the experiment with the Taucherbrille gas inlet $\alpha = 0.71$ mbar×cm. However, there are only three data points and the side areas close to the plasma position and inside the DMT are not included. Therefore the number for the stopping parameter seen here is too small.

The fact that there is less gas present at the same incoming flow rate means that the gas is pumped away more quickly if the nozzle is used. As shown in fig. 6.21, there is a gas outlet on the opposite side of the nozzle, enabling the gas from the nozzle to be pumped out quicker. The gas pressure distribution clearly shows that this scheme works, and a pressure gradient can be generated in the Taucherbrille area. The effect becomes even stronger when higher buffer gas flows are used.

6.2.4 Ion Spectrum

The three most common ion species emitted by a GDP source are Xe^{1+}, Xe^{2+} and W^{1+} (see section 6.1.2.1). These are the only ones that can still be detected when there are significant buffer gas flows. Fig. 6.23 shows the ion spectrum of Xe^{1+} ions for different

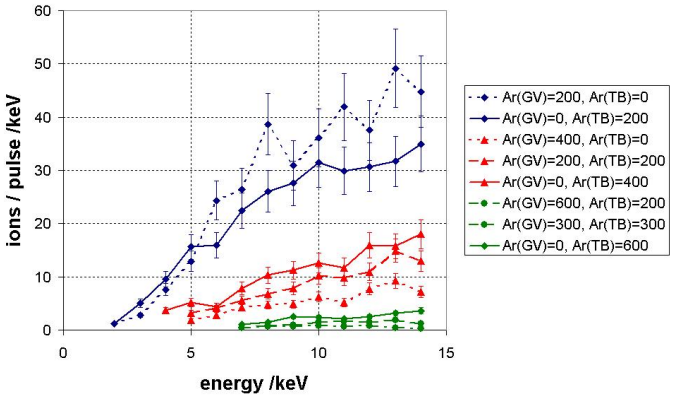

Figure 6.23: Ion spectrum of single charged xenon ions.

buffer gas flows. The differences to the spectra in fig. 6.8 can be attributed to different experimental conditions (see also section 6.1.1). For a buffer gas flow of 200 sccm, there seem to be some more ions coming through to the spectrometer when the nozzle is used. The difference, however, is very close to the error bars of the data points. For buffer gas flows of 400 and 600 sccm, the spectrometer detects fewer ions when the nozzle is used. In fact, the number of ions is reduced to roughly 50% when the nozzle is used instead of the gas curtain inlet.

In fig. 6.24, the spectra of W^{1+} ions can be seen. In the case of the 200 sccm gas flow, the nozzle actually seems to mitigate the ions a little bit better than the Taucherbrille gas inlet. However, the differences are within the error bars. For higher gas flows, the situation is very similar to the case of Xe^{1+} ions. The number of ions detected when the nozzle is used is about 50% lower than for the other case.

Xe^{2+} ions decrease very strongly with only little buffer gas flows present. In fact, they are close to the detection limit for more than 200 sccm buffer gas flow. In this situation, no differences between gas curtain nozzle and Taucherbrille gas inlet can be measured.

Overall it can be seen that for Ar gas flows of over 400 sccm, the mitigation of Xe^{1+} and W^{1+} ions is about twice as efficient with the gas curtain nozzle compared to the Taucherbrille gas inlet. This is a very surprising result, as no difference in the ion spectrum was expected. The likely reason is that high speed and the common direction of all gas flow particles led to a stronger deflection of single ions than in a static buffer gas atmosphere. This deflection then leads to a higher efficiency of the foil traps in the DMT.

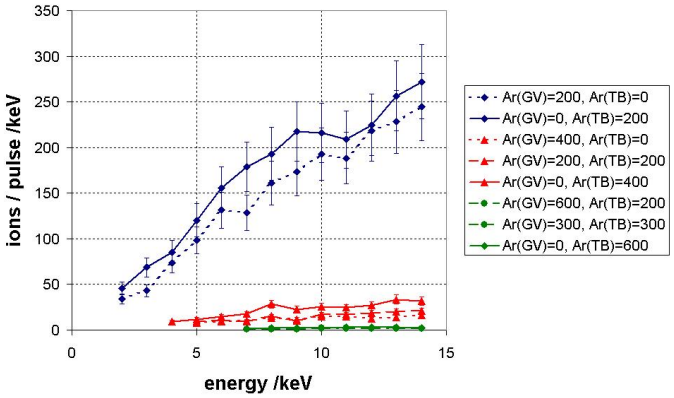

Figure 6.24: Ion spectrum of single charged tungsten ions

.

6.2.5 Temperature Development

The temperature development for different repetition rates is shown in fig. 6.25. The source repetition rate was increased in 500 Hz steps and left running for about 20 minutes at each repetition rate. By that time, the temperature measured by the thermocouple stabilised, meaning the area around the device was in thermal equilibrium. The temperature increase for each 500 Hz step in the repetition rate became lower for higher rates. The step was 70 K for the repetition rate increase from 0 to 500 Hz and only 30 K for the increase from 1500 to 500 Hz. The temperature measured for 2 kHz was 240 °C.

Assuming a worst-case scenario, continuing the curve with a temperature increase of 70 K for each repetition rate step, the upper limit for the temperatures at 4 kHz would be 520 °C. This is still far below the melting points of all materials (copper, stainless steel, molybdenum) used in the setup. These temperature measurements show that there are no problems of thermal damage to be expected when using the gas curtain at high repetition rates of several kHz.

6.2.6 Conclusion

A gas curtain was implemented using the nozzle described in section 6.2.2. It was shown to display a pressure gradient perpendicular to its flow direction. Measurements of ion spectra at 500 Hz source repetition rate displayed a 50% better mititgation of Xe^{1+} and W^{1+} ions than with the same buffer gas flow without that pressure gradient.

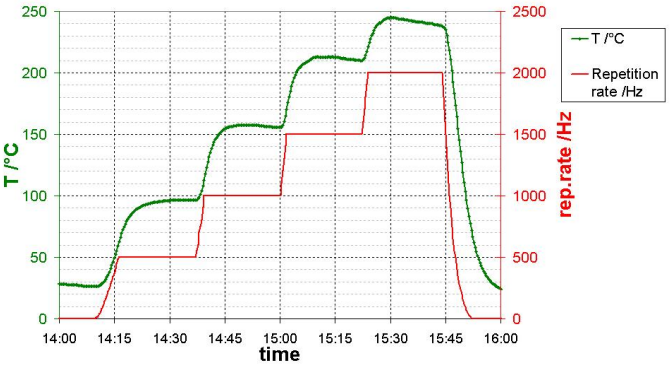

Figure 6.25: Temperature development of gas curtain nozzle (green) for different repetition rates (red).

Temperature measurements at higher repetition rates showed that the setup should not suffer from thermal degradation with a source operating at 4 kHz or higher.

Chapter 7

Transmission Test Stand for Debris Mitigation Tools

For the application of DMTs, not only their debris-mitigating capabilities are of interest, but also their optical transmission. A good debris mitigation makes sense only when still enough EUV light is transmitted. In order to check the optical transmission of the DMTs, a test stand was set up and evaluated.

7.1 Experimental Setup

The setup of the test stand is shown in fig. 7.1 and fig. 7.2. The plasma was simulated by a light source consisting of a laser, a diverging lens, a diffuser and an aperture. The

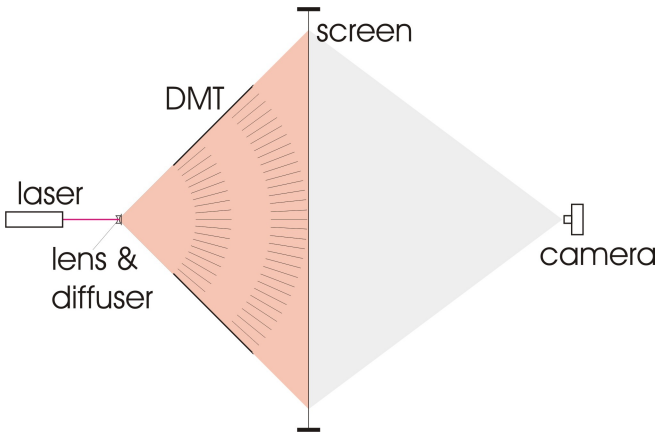

Figure 7.1: Principal setup of the transmission test stand for debris mitigation tools.

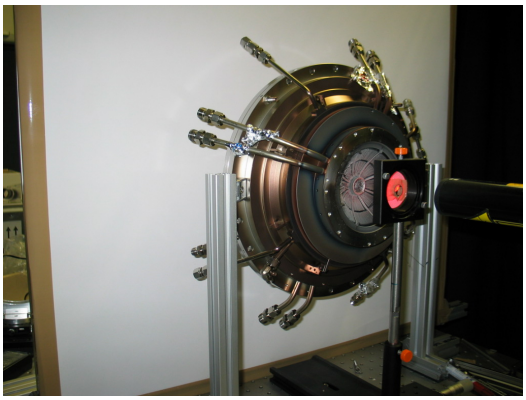

Figure 7.2: Photo of the DMT transmission test stand. The diverging lens with the diffuser can be recognized by the scattered red light from the laser. The DMT is mounted between the diffuser and the white paper screen in the back.

aperture defined the light source to have a diameter of 1 mm. An EUV-emitting pinch plasma has the same diameter.

The DMT was illuminated by this light source and the shadow was observed on a thin screen behind it. The screen was observed with a digital camera. Comparing the pictures of the screen with and without a DMT present, a spatial transmission distribution could be measured. The photo detector chip of the camera had a linear response; this was verified by performing the same experiment at different exposure times. For the evaluation of the test stand, the first full-size 20 cm DMT (full solid angle, in contrast to the prototype described in section 5.2) with two stages was analysed.

The transmission picture was obtained by dividing the intensity value of every pixel by the intensity value of the same pixel when no DMT was present. However, during experiments it turned out that in some areas of the screen the light intensity actually increased (fig. 7.3). For that picture, pixels that were darker with a DMT present were coloured white. Otherwise they were assigned a grey value. The darker a pixel is in the picture, the more the light has increased. The effect can be explained with grazing-incidence reflection of the light at the foils of the DMT. The light reflected at the foils, however, is not transmitted through the focusing optics. Thus it had to be regarded as lost, and a correction had to be made in the analysis.

For the transmission measurements, the correction worked as follows: Pixels that displayed an increased light intensity with a DMT were set to have a transmission of one. The remaining pixels were treated normally, the transmission being the ratio of pixel intensities.

Figure 7.3: This picture shows the increase in light intensity in certain areas when a DMT is present. Dark pixels indicate such an increase. The foil structure of the DMT can be easily recognised.

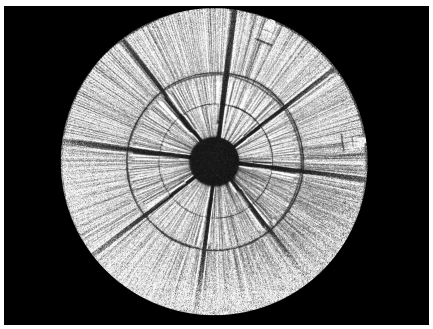

Figure 7.4: Transmission picture of a DMT as explained in the text. Black pixels indicate $T = 0$, white pixels indicate $T = 1$.

7.2 Results

Fig. 7.4 shows the transmission distribution of the DMT. The foil structure can clearly be recognised. The concentric dark rings are caused by the support structure. The centre region is shadowed, as there is a beam dump for the electron beam coming out of the pinch (see section 1.5).

Pixels with the same distance to the centre of the picture represent the same angles to the optical axis. Averaging all transmission values with the same distance to the centre yields the transmission as a function of the angle to the optical axis. These values can be compared with theoretical ones. The theoretical values were calculated from the blueprints of the DMT. The ratio of foil surface (no transmission) to free surface (transmission) were calculated for each angle to the optical axis. As the DMT consisted of two stages, some foils in the second stage were already in the shadow of a foil in the first stage and thus did not reduce transmission any further. This was taken into account in the calculations. The comparison of theoretical and experimental data is shown in fig. 7.5. The experimental values fit the theoretical ones very well. The two dips in the curve are caused by the support structure.

In order to obtain an integral transmission for a DMT, it has to be taken into account that larger illumination angles represent bigger solid angles. The integral

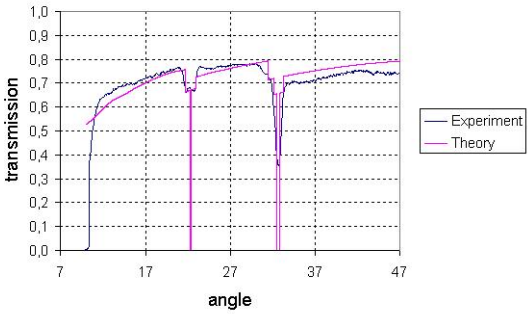

Figure 7.5: DMT transmission as a function of angle to the optical axis. Comparison of theoretical and experimental values.

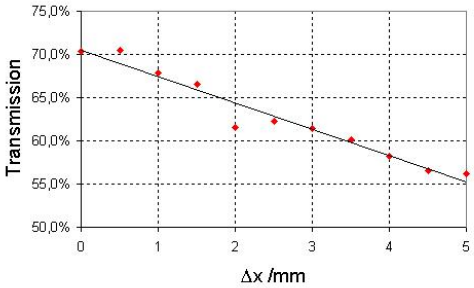

Figure 7.6: Integrated DMT transmission as a function of source displacement perpendicular to the optical axis.

transmission can be calculated as the weighted average of the transmission values for each angle. This procedure yields an integral transmission of 70.1% for the DMT measured. For the theoretical values the integral transmission can be calculated to be 72.9 %.

Another measurement was performed to check the sensitivity of the DMT to maladjustments of the source. A shift of the source in the direction of the optical axis can be regarded as not critical, as it is a movement parallel to the foils. It would lead to very little additional shadowing due to the support structure. A displacement of the source perpendicular to the optical axis results in more shadowing. Therefore the light source was displaced from the optical axis, and the DMT transmission was measured. Fig. 7.6 shows the integrated transmission as a function of displacement of the light source.

Experiments were also performed replacing the screen with a system of Fresnel lenses. They were meant to simulate a collector, and it was hoped to measure an intensity distribution at the intermediate focus. These experiments failed due to the poor optical quality of the available Fresnel lenses.

Appendix A

Charged Particles in a Planar Capacitor

Charged particles will be deflected in a planar capacitor. If their energy is too low, they will eventually hit one of the capacitor plates. In other words, for a given charge and given capacitor parameters only particles above a certain energy will be transmitted through the capacitor. In order to obtain an expression for this cut-off, the worst-case particle trajectory is considered. In this case, the particle enters the capacitor on one side in a way that the deflection allows it just to pass the other side in the middle of the capacitor and exit it at the same side as the beginning. The geometry is shown in fig. A.1. In the following calculation, l is the length of the capacitor plates, d the distance between them and V the applied voltage between them. The particle mass is m, its charge q and its speed is $\vec{v}$. It is assumed that $l \gg d$ and therefore $|\vec{v}| \approx v_x = v$. In x-direction, the particle travels at a constant speed, whereas in y-direction there is a constant acceleration. Thus the trajectory has a parabolic shape with

$$y = \frac{1}{2}\frac{qU}{md}\left(\frac{x}{v}\right)^2 \quad . \tag{A.1}$$

The cut-off condition is

$$y = d \qquad \text{for} \qquad x = \frac{l}{2} \quad . \tag{A.2}$$

Thus it follows that

$$U[\mathrm{V}] = 16\frac{Ed^2}{ql^2} = 16\frac{E_{kin}[\mathrm{eV}]}{Z}\left(\frac{d}{l}\right)^2 \tag{A.3}$$

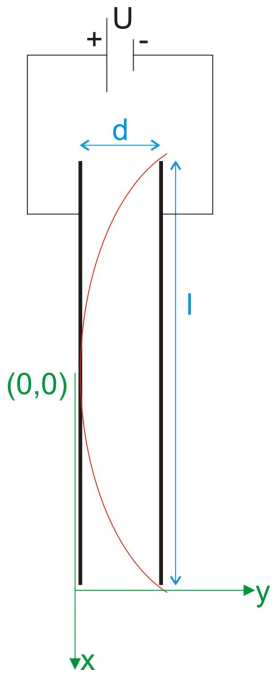

Figure A.1: Worst possible particle trajectory (red) in a planar capacitor.

or

$$E_{kin}[\mathrm{eV}] = \frac{ZU[\mathrm{V}]}{16}\left(\frac{l}{d}\right)^2 \quad . \tag{A.4}$$

The capacitor used in the experiment had a length of 70 mm. The plates were 7 mm apart. The entrance and exit apertures were only 5 mm wide. This requires the expression d^2 in equation A.4 to be changed to $d_1 d_2$, with d_1 being the distance between the plates and d_2 the aperture width. For the voltage of 950 V used in this experiment, the cutoff energy was 8.3 keV.

For large collection angles a repelling field would have to be used. The cutoff in that case would be

$$E_{kin}[\mathrm{eV}] = U[\mathrm{V}] \quad . \tag{A.5}$$

For the same cutoff, this leads to a voltage that is nine times higher than in the capacitor setup.

Appendix B

Charged Particles in a Magnetic Field

In a magnetic field, a charged particle travels on a circular trajectory, the radius given by

$$r = \frac{mv}{qB} \quad , \tag{B.1}$$

where m is the particle mass, v its speed, q its charge and B the magnetic flux density. The geometry is given in fig. B.1. Considering a worst-case scenario as in appendix A, the particle trajectory is given by

$$y = -\sqrt{r^2 - x^2} + r \quad . \tag{B.2}$$

The cut-off condition is the same as in the capacitor case

$$y = d \qquad \text{for} \qquad x = \frac{l}{2} \quad . \tag{B.3}$$

For the cut-off it follows that

$$r = \frac{d}{2} + \frac{l^2}{8d} \tag{B.4}$$

and

$$v = \frac{qB}{m} r = \frac{qB}{m} \left(\frac{d}{2} + \frac{l^2}{8d} \right) \quad . \tag{B.5}$$

Setting in the parameters for the magnet given in section 4.3.2, $B = 0.38$ T, $d = 8$ mm and $l = 8$ cm, and assuming a single charged xenon ion, we get $v = 4.8 \times 10^4 \ \frac{\mathrm{m}}{\mathrm{s}}$. That corresponds to a kinetic energy of 1.6 keV.

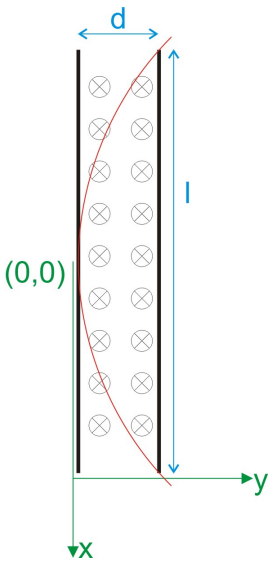

Figure B.1: Worst possible particle trajectory (red) in a homogeneous magnetic field.

Summary and Conclusion

This thesis is mostly concerned with the lifetime of the collector optics of high power EUV sources. Research in this field is driven by companies developing these sources. The experiments for this work were performed in close collaboration with one of these companies, namely XTREME technologies [7]. One consequence of this process is that the research does not focus on fundamental physical problems. Fundamentally new, previously unknown phenomena were not expected to be discovered. Instead, the main research interest is to optimise the known source concepts and push the important source parameters to their limits.

One of the main parts of this work was the characterisation of debris emission of an LPP source and the evaluation of different debris mitigation schemes. Sputtering of energetic ions had been identified as the main damaging effect to the optical surfaces. The maximum debris emission was in the direction of the incoming laser beam.

Four mitigation schemes were evaluated: mechanical shutters, buffer gases, electric and magnetic fields. It was shown that mechanical shutters can be ruled out. Test setups for electrical and magnetic fields were evaluated. Electrical fields did not have a strong effect on the debris load. Magnetic fields seemed to be somewhat more efficient, but the scalability to large solid angles is highly questionable. Inserting buffer gases between the plasma and the collector seems to be the only feasible solution. A buffer gas system that worked over the full solid angle was implemented at the LPP source. With such a scheme, a lifetime of 3.6×10^9 pulses was demonstrated at conditions that still show manageable EUV absorption in the gas. This is the highest number published so far for a xenon-based LPP. With a larger number of mirror layers, a lifetime of 2.5×10^{10} pulses can be extrapolated. This is in close range to the requirements of high-volume manufacturing tools [5]. The mirrors with the increased number of layers were also demonstrated already. The collector lifetime for xenon-LPPs is not to be considered a showstopper anymore.

For the gas discharge plasmas, ion emission measurements were performed. The ion spectrum of a high power Xe-GDP source was characterised for the first time. Similar measurements were performed by other groups, but only for systems with low repetition rates [83, 55]. Ion sputtering of surfaces was the primary damaging effect here as well. It was shown how the increase of the buffer gas pressure and addition of low mass atoms like hydrogen reduce the amount of ejected ions. Absolute optics lifetime measurements were not performed as part of this work for organisational reasons: They were performed by co-workers at another EUV source. A lifetime of 10^9 pulses was demonstrated by them recently.

The possibility of using a gas curtain was evaluated as well. The results were promising: Although there seemed to be quite an optimisation potential in the nozzle used, differences in the ion spectrum were measured. The setup was also shown to withstand the thermal loads associated with higher repetition rates, which is a crucial problem for many aspects of the discharge plasma.

As a minor part of the work, the optical transmission of the debris mitigation tools was measured. It was shown that the tools have an optical transmission of approx. 70 %, which is close to the theoretical value. Although this does not seem to be a very interesting result from the physical point of view, the result is extremely important for the debris mitigation at GDPs. The DMTs are precision-engineered, using large surfaces made out of molybdenum foils. It is very likely that there are no devices in the world that look similar and are made of the same material. Thus, aspects of the position precision, stress and strain on the foils etc. are not known. Therefore the tools had to be evaluated after the construction. A second aspect of the transmission test stand is that it is not clear that the DMT maintains its transmission after hundreds of millions of pulses. The transmission test stand provides a means to quantify possible deteriorations in the DMT performance.

Another part of the work was not directly connected with debris mitigation. The EUV emission isotropy of a LPP was measured. It was shown that the main emission is in the direction of the incoming laser pulse. A model was presented, showing that the distribution can well be explained by absorption on the back side of the plasma. Unfortunately the EUV emission maximum is the same as the debris emission maximum. The high anisotropy of the emission could also pose problems for the illuminating optics behind the intermediate focus.

What will the future of EUV sources look like? The answer is not easy to give, as in industrial research there are many results that are confidential and thus not published. There are, however, some trends that can be seen.

The optics lifetime of xenon-based sources due to ion sputtering does not seem to be a problem anymore, in part due to the results of this thesis. For the GDP case, particles of electrode material are still present. They are too big to be stopped efficiently by a buffer gas. If they are stopped in the DMT, they can cause additional shadowing, reducing the DMT transmission. However, it is not likely that xenon-based sources will ever have to fulfill the HVM requirements. The conversion efficiency - and with it the EUV power for HVM (125 W EUV in the IF) - does not seem to be achievable with these sources.

The alternatives are tin and lithium - tin being favoured by most researchers. Both of these could fulfill the source power requirements. The optics lifetime problems, however, are expected to be worse than for xenon. There will be an additional effect of deposition of tin or lithium on optical surfaces. Although sputtering and deposition could cancel each other for certain conditions, it is not to be expected that they can do that over the whole range of a collector mirror. Thus the deposition effect will have to be suppressed together with the other debris effects. Recently, cleaning procedures with halogens were suggested.

Laser produced and gas discharge plasmas are still competing for the scheme eventually being used for HVM. The main drawback for the LPP is the availability of a laser that delivers about 10 - 15 kW in ns pulses at a repetition rate of several kHz. It is often claimed that the EUV output can be scaled up without problems once the laser is available. However, the author of this work does not know of any group seriously developing a laser with these parameters. Both the development time and cost are most likely too high.

So the only source that seems feasible as a HVM source is a tin-based discharge plasma. The success of its development will depend on if - apart from the collector lifetime - the other big problems will be solved - namely output power and electrode lifetime. Recently, continuously rotating electrodes were suggested, constantly renewing their surface with a tin layer. They seem to be a solution for the electrode lifetime issue. As the constant movement also allows a better heat dissipation, they could also contribute to the solution of the output power problem.

Bibliography

[1] www.intel.com.

[2] www.itrs.net

[3] K. Ota, Y. Watanabe, V. Banine and H. Franken, *EUV Source Requirements for EUV Lithography*, EUV sources for lithography, Ed. V. Bakshi, SPIE Press (2006).

[4] *X-ray interactions with matter*, internet database, www.cxro.lbl.gov.

[5] V. Bakshi, *EUV Source Technology: Challenges and Status*, EUV sources for lithography, Ed. V. Bakshi, SPIE Press (2006).

[6] www.jo-mikrotechnik.com.

[7] www.xtremetec.de

[8] M. C. Schürmann, T. Missalla, K. R. Mann, S. Kranzusch, R. M. Klein, F. Scholze, G. Ulm, R. Lebert, L. Juschkin, *Metrology tools for EUVL-source characterization and optimization*, Proc. SPIE **5037**, 378 (2003).

[9] www.ptb.de

[10] F. Bijkerk, S. A. van der Westen, C. Bruineman, R. Huiting, R. de Bruijn and R. Stuik, *Flying Circus EUV Source Metrology and Source Development Assessment*, EUV sources for lithography, Ed. V. Bakshi, SPIE Press (2006).

[11] Y. Tao, F. Sobatzadeh, H. Nishimura, R. Matsui, T. Hibino, T. Okuno, S. Fujioka, K. Nagai, N. Norimatsu, K. Nishihara, N. Miyanaga, Y. Izawa, A. Sunahara and T. Kawamura, *Monochromatic imaging and angular distribution measurements*

of extreme ultraviolet light from laser-produced Sn and SnO_2 plasmas, Appl. Phys. Lett. **85**, 1919 (2004).

[12] Y. Tao, M. Nakai, H. Nishimura, S. Fujioka, T. Okuno, T. Fujiwara N. Ueda, N. Miyanaga and Y Izawa, *Temporally resolved Schwarzschild microscope for the characterization of extreme ultraviolet emission in laser-produced plasmas*, Rev. Sci. Instrum. **75**, 5173 (2004).

[13] D. Salzmann, *Atomic Physics in Hot Plasmas*, Oxford University Press, New York (1998).

[14] Y. B. Zel'dovich and Y. P. Raizer, *Physics of Shock Waves and High-Temperature Hydrodynamic Phenomena*, Ed. W. D. Hayes and R. F. Probstein, Dover Publications, Mineola (2002).

[15] D. Attwood, *Soft X-Rays and Extreme Ultraviolet Radiation*, Cambridge University Press (1999).

[16] D. Colombant and G. F. Tonon, *X-ray emission in laser-produced plasmas*, J. Appl. Phys. **44**, 3524 (1973)

[17] U. Stamm, G. Schriever and J. Kleinschmidt, *High-Power GDPP Z-Pinch EUV Source Technology*, EUV sources for lithography, Ed. V. Bakshi, SPIE Press (2006).

[18] R. C. Spitzer, T. J. Orzechowski, D. W. Phillion, R. L. Kauffman and C. Cerjan, *Conversion efficiencies from laser produced plasmas in the extreme ultraviolet regime*, J. Appl. Phys. **79**, 2251 (1996).

[19] A. Cummings, G. O'Sullivan, P. Dunne, E. Sokell, N. Murphy and J. White, *Conversion efficiency of a laser-produced Sn plasma at 13.5 nm, simulated with a one-dimensional hydrodynamic model and treated as a multi-component blackbody*, J. Phys. D **38**, 604 (2005)

[20] E. R. Kieft, K. Garloff, J. J. A. M. van der Mullen and V. Banine, *Comparison of experimental and simulated extreme ultraviolet spectra of xenon and tin discharges*, Phys. Rev. E **71**, 036402 (2005).

[21] N. Böwering, M. Martins, W. N. Partlo and I. V. Fomenkov, *Extreme ultraviolet emission spectra of highly ionized xenon and their comparison with model calculations*, J. Appl. Phys. **95**, 16 (2004).

[22] S. Churilov, Y. N. Joshi and J. Reader, *High-resolution spectrum of xenon ions at 13.4 nm*, Opt. Lett. **28**, 1478 (2003).

[23] F. Gilleron, M. Poirier, T. Blenski, M. Schmidt and T.Ceccotti, *Emissive properties of xenon ions from a laser-produced plasma in the 100-140 Å spectral range: Atomic-physics analysis of the experimental data*, J. Appl. Phys. **94**, 2086 (2003).

[24] G. O'Sullivan, A. Cummings, P. Dunne, P. Hayden, L. KcKinney, N. Murphy and J. White, *Atomic Physics of Highly Charged Ions and the Case for Sn as a Source Material*, EUV sources for lithography, Ed. V. Bakshi, SPIE Press (2006).

[25] J. D. Gillaspy, *Atomic Xenon Data*, EUV sources for lithography, Ed. V. Bakshi, SPIE Press (2006).

[26] U. Stamm, K. Gäbel, J. Kleinschmidt et al., *EUV source development at XTREME Technologies: An update*, EUV Source Workshop, San Jose, USA (2005).

[27] M. Richardson, *The UCF tin-doped droplet source*, EUV Source Workshop, San Jose, USA (2005), Proceedings available at www.sematech.org.

[28] I. Fomenkov, W. Partlo and N. Böwering, *Progress in development of a high power source for EUV lithography*, EUV Source Workshop, Miyazaki, Japan (2004), Proceedings avilable at www.sematech.org.

[29] J. Pankert, *Philip's EUV source: main messages*, EUV Source Workshop, Miyazaki, Japan (2004), Proceedings available at www.sematech.org.

[30] H. A. Baldis, E. M. Campbell and W. L. Kruer, *Laser-Plasma-Interactions*, Handbook of Plasma Physics, Vol. 3: Physics of Laser Plasma, Ed. A. M. Rubenchik and S. Witkowski, North Holland (1991).

[31] R. Kodama, T. Mochizuki, K. A. Tanaka and C. Yamanaka, *Enhancement of keV x-ray emission in laser-produced plasmas by a weak prepulse laser*, Appl. Phys. Lett. **50**, 720 (1987).

[32] U. Teubner, G Kühnle and F. P. Schäfer, *Soft x-ray spectra produced by subpicosecond laer-double-pulses*, Appl. Phys. Lett. **59**, 2672 (1991).

[33] R. de Bruijn, A. Bartnik, H. Fledderus, H. Fiedorowicz, P. Hegeman, R. Constantinescu and F. Bijkerk, *Characterization of a novel double-gas-jet laser-plasma EUV source*, Proc SPIE **3997**, 157 (2000).

[34] H. Fiedorowicz, A. Bartnik, M. Szczurek, H. Daido, N. Sakaya, V. Kmetik, Y. Kato, M Suzuki, M. Matsamura, J. Tajima, T. Nakayama and T. Wilhein, *Investigation of soft X-ray emission from a gas puff target irradiated with a Nd:YAG laser*, Opt. Comm. **163**, 103 (1999).

[35] M. Kanouff, H Shields, L. Bernardez, D. Chenoweth and G. Kubiak, *Absorption of extreme ultraviolet light in a laser produced gas-jet plasma source*, J. Appl. Phys. **90**, 3726 (2001).

[36] M. Mori, T. Shiraishi, E. Takahashi, H. Suzuki, L. B. Sharma, E. Miura and K. Kondo, *Extreme ultraviolet emission from Xe clusters excited by high-intensity lasers*, J. Appl. Phys **90**, 3595 (2001).

[37] S. Ter-Avetisyan, M. Schnürer, H. Stiel, U. Vogt, W. Radloff, W. Karpov, W. Sandner and P. V. Nickles, *Absolute extreme ultraviolet yield from femtosecond-laser-excited Xe clusters*, Phys. Rev. E **64**, 036404 (2001).

[38] B. A. M. Hansson, L. Rymell, M. Berglund and H. M. Hertz, *A liquid-xenon-jet laser-plasma X-ray and EUV source*, Microelec. Engin. **53**, 667 (2000).

[39] I. W. Choi, H. Daido, S. Yamagami, K. Nagai, T. Norimatsu, H. Takabe, M. Suzuki, T. Nakayama and T. Matsui, *Detailed space-resolved characterization of a laser-plasma soft-x-ray source at 13.5-nm wavelength with tin and its oxides*, J. Opt. Soc. Am. B **17**, 1616 (2000).

[40] W. H. Bennet, *Magnetically Self-Focussing Streams*, Phys. Rev. **45**, 890 (1934).

[41] Y. Teramoto, H. Sato and M. Yoshioka, *Capillary Z-Pinch Source*, EUV sources for lithography, Ed. V. Bakshi, SPIE Press (2006).

[42] J. Pankert, K. Bergmann, R. Wester, et. al., *Hollow-Cathode-Triggered Plasma Pinch Discharge*, EUV sources for lithography, Ed. V. Bakshi, SPIE Press (2006).

[43] H. Wolter, *Spiegelysteme streifenden Einfalls als abbildende Optiken für Röntgenstrahlen*, Ann. Phys. 6. Folge **10**, 94 (1952).

[44] H. Wolter, *Verallgemeinerte Schwarzschildsche Spiegelsysteme streifender Reflexion als Optiken für Röntgenstrahlen*, Ann. Phys. 6. Folge **10**, 286 (1952).

[45] H. A. Bender, D. O'Connell and W. T. Silfvast, *Velocity characterization of particulate debris from laser-produced plasmas used for extreme-ultraviolet lithography*, Appl. Optics **34**, 6513 (1995).

[46] J. M. Bridges, C. L. Cromer and T. J. McIlrath, *Investigation of a laser-produced plasma VUV light source*, Appl. Opt. **25**, 2208 (1986).

[47] H. Daido, S. Yamagami, M. Suzuki, H. Azuma, I. W. Choi and H. Fiedorowicz, *Low-energy ion emission from a xenon gas-puff laser-plasma X-ray source*, Appl. Phys. B **72**, 385 (2001).

[48] M. L. Ginter and T. J. McIlrath, *Debris and VUV emission from a laser-produced plasma operated at 150 Hz using a krypton fluoride laser*, Appl. Opt. **27**, 885 (1988).

[49] T. Letardi, D. Lo and C.-E. Zheng, *Particle dynamics of debris produced during laser-plasma soft x-ray generation*, J. Appl. Phys. **89**, 1458 (2001).

[50] M. C. Miller, J. R. Celeste, M. A. Stoyer, L. J. Suter, M. T. Tobin, J. Grun, J. F. Davis, C. W. Barnes and D. C. Wilson, *Debris characterization diagnostic for the NIF*, Rev. Sci. Instrum. **72**, 537 (2001).

[51] M. Richardson, W. T. Stilfvast, H. A. Bender, A. Hanzo, V. P. Yanovsky, F. Jin and J. Thorpe, *Characterization and control of laser plasma flux parameters for soft-x-ray projection lithography*, Appl. Opt. **32**, 6901 (1993).

[52] M. Wieland, T. Wilhein, M. Faubel, C. Ellert, M. Schmidt and O. Sublemontier, *EUV and fast ion emission from cryogenic liquid jet target laser-generated plasma*, Appl. Phys. B **72**, 591 (2001).

[53] P. Mora, *Plasma Expansion into a vacuum*, Phys. Rev. Lett. **90**, 185002 (2003).

[54] E. L. Antonsen, K. C. Thompson, M. R. Hendricks, D. A. Alman, B. E. Jurczyk and D. N. Ruzic, *Ion Debris Characterization from a Z-Pinch Extreme Ultraviolet Light Source*, J. Appl. Phys. **99**, 063301 (2006).

[55] L. E. Klebanoff, R. J. Anderson, D. A. Buchenauer, N. R. Fornaciari and H. Komori, *Erosion of condenser optics exposed to EUV sources*, EUV sources for lithography, Ed. V. Bakshi, SPIE Press (2006).

[56] H. Komori, T. Abe, T. Suganuma, Y. Imai, Y. Sugimoto, H. Someya, H. Hoshino, G. Soumagne, Y. Takabayashi, H. Mizoguchi, A. Endo, K. Toyoda and Y Horiike, *Laser-produced-plasma light source development for extreme ultraviolet lithography*, J. Vac. Sci Technol. B **21**, 2843 (2003).

[57] R. C. Elton, D.-M. Billings, J. Grun, F. C. Young, C. K. Manka, B. H. Ripin, H. R. Burris, J. Resnick, D. J. Ripin and J. R. Millard, *X-ray damage to optical components using a laser-plasma source*, J. Appl. Phys. **74**, 5432 (1993).

[58] S. Bajt, H. N. Chapman, N. Nguyen, J. Alameda, J. C. Robinson, M. Malinowski, E. Gullikson, A. Aquila, C. Tarrio and S. Grantham, *Design and performance of capping layers for extreme-ultraviolet multilayer mirrors*, Appl. Opt. **42**, 5750 (2003).

[59] K. Hamamoto, Y. Tanaka, T. Watanabe, N. Sakaya, M. Hosoya, T. Shoki, H. Hada, N. Hishinuma, H. Sugahara and H. Kinoshita, *Cleaning of extreme ultraviolet lithography optics and masks using 13.5 nm and 172 nm radiation*, J. Vac. Sci. Technol. B **23**, 247 (2005).

[60] L. E. Klebanoff, M. E. Malinowski, W. M. Clift, C. Steinhaus and P. Grunow, *Use of gas phase ethanol to mitigate extreme UV/water oxidation of extreme UV optics*, J. Vac. Sci. Technol. A **22**, 425 (2004).

[61] J. H. Underwood, E. M. Gullikson and K. Nguyen, *Tarnishing of Mo/Si multilayer x-ray mirrors*, Appl. Opt. **32**, 6985 (1993).

[62] M. Berglund, L. Rymell, H. M. Hertz and T. Wilhein, *Cryogenic liquid-jet target for debris-free laser-plasma soft x-ray generation*, Rev. Sci. Instrum. **69**, 2361 (1998).

[63] L. Rymell, M. Berglund and H. M. Hertz, *Debris-free single-line laser-plasma x-ray source for microscopy*, Appl. Phys Lett. **66**, 2625 (1995).

[64] www.ilt.fraunhofer.de.

[65] www.varianinc.com

[66] www.helixtechnology.com

[67] S. Kranzusch, C. Peth and K. Mann, *Spatial characterization of extreme ultraviolet plasmas generated by laser excitation of xenon gas targets*, Rev. Sci. Instrum. **74**, 969 (2003).

[68] M. Hotzel, private communication.

[69] www.intellemetrics.com.

[70] www.iof.fraunhofer.de.

[71] G. P. Chambers and J. Fine *Pure element sputtering yield data*, Practical Surface Analysis (second edition), Vol. 2: Ion and Neutral Spectroscopy, Ed. D. Briggs and M. P. Seah, Wiley & Sons (1992).

[72] J. D. Gillaspy, *Highly charged ions*, J. Phys. B. **34**, R93 (2001).

[73] www.linos.de

[74] *The stopping and range of ions in matter*, software package, www.srim.org

[75] www.leybold.com

[76] J. Kleinschmidt, private communication.

[77] T. Feigl, private communication.

[78] www.pfeiffer-vacuum.com

[79] E. M. Purcell, *The Focusing of Charged Particles by a Spherical Condenser*, Phys. Rev. **54**, 818 (1938).

[80] J. L. Wiza, *Microchannel Plate Detectors*, Nucl. Inst. and Meth. **162**, 587 (1979).

[81] www.webelements.com

[82] H. Vogel, *Gerthsen Physik*, 18. Auflage, Springer-Verlag (1995).

[83] D. N. Ruzic, *Origin of debris in EUV sources and its mitigation*, EUV sources for lithography, Ed. V. Bakshi, SPIE Press (2006).

[84] D. N. Ruzic, private communication.

[85] J. E. Crow, P. L. Auer and J. E. Allen, *The expansion of plasma into a vacuum*, J. Plasma Phys. **14**, 65 (1975).

[86] A. V. Gurevich and A. P. Meshcherkin, *Ion acceleration in an expanding plasma*, Sov. Phys. JETP **53**, 945 (1981).

[87] L. Baars-Hibbe, private communication.

[88] T. Kusakabe, T. Horiuchi, N. Nagai, H. Hanaki, I. Konomi and M. Sakisaka, *Charge transfer of multiply charged slow argon, krypton, xenon ions on atomic and molecular targets. Single-charge transfer cross sections*, J. Phys. B: At. Mol. Phys. **19**, 2165 (1986).

[89] N. R. Fornaciari, M. P. Kanouff, *Discharge source with gas curtain for protecting optics from particles*, world patent WO 03/026363 A1 (2003).

Acknowledgements

At first, I would like to express my gratitude to Professor Roland Sauerbrey for giving me the opportunity to work in this interesting and dynamic field of research. I would also like to thank him for his continuing support through all ups and downs of the EUV projects. My further gratitude goes to Professor Henryk Fiedorowicz and Professor David Ruzic for acting as external referees to this thesis.

For the work at the Institute of Optics and Quantum Electronics I would like to thank Mario Hotzel, Reinhard Seifert and Wolfgang Ziegler for all the help they have given me.

Most of the work was performed in the laboratories of XTREME Technologies. Special acknowledgements go to Guido Hergenhan, Kai Gäbel, Rene de Bruijn and Jürgen Kleinschmidt. There are many more people at XTREME Technologies who deserve a "thank you" in one or the other way. They are (in alphabetical order): Lutz Baars-Hibbe, Istvan Balogh, Jesko Brudermann, Gilbert Dornieden, Alexander Eickhoff, Sebastian Enke, Frank Flohrer, Wolfgang Friedrichs, Bernhard Grote, Diethard Klöpfel, Björn Mader, Thomas Missalla, Mike Möritz, Rainer Müller, Dörthe Reins, Guido Schriever, Max Christian Schürmann, Uwe Stamm, Boris Tkachenko, Tran Duc Chinh, Mario Wegstroth and Christian Ziener.

Further on, I would like to thank Henrik Fiedorowicz, Andrzej Bartnik, Janus Mikolajczyk and Rafal Rakowski for their hospitality during my visits to the Institute of Optoelectronics in Warsaw, Poland.

Erik Antonsen, Keith Thompson and David Ruzic of the plasma material interaction research group at the University of Illinois in Urbana-Champaign also deserve acknowledgements for providing the ion spectrometer used in this thesis.

A special thanks goes to my parents, who have stood behind me in every station of my life. And last, but not least, the biggest "thank you" goes to Rachel for providing a happy home whenever I was not at work.

Zusammenfassung (deutsch)

Das Interesse an plasmabasierten Hochleistungsquellen für extrem ultraviolette (EUV) Strahlung ist in den letzten Jahren stark gewachsen. Die Entwicklung dieser Quellen ist eine Grundlage der EUV-Lithographie, die in einigen Jahren zur Herstellung von Computerchips serienreif sein soll. Es gibt zwei grundlegende Konzepte der Plasmaerzeugung für EUV-Quellen: das Laserplasma (LPP) und das Gasentladungsplasma (GDP). Beim LPP wird ein kurzer Laserpuls auf ein Target fokussiert und erzeugt dort ein Plasma. Beim GDP erzeugt ein kurzer Spannungspuls eine Gasentladung und koppelt so die Energie in das Plasma.

Die vorliegende Arbeit dreht sich im wesentlichen um die Lebensdauer von Kollektoroptiken in EUV-Hochleistungsquellen. Der Großteil der Forschung auf diesem Gebiet wird von Firmen geleistet, die diese Quellen entwickeln. Die Experimente für diese Arbeit wurden in enger Zusammenarbeit mit einer dieser Firmen, XTREME Technologies GmbH [7], durchgeführt. Als Folge dieser Forschungsstruktur steht weniger die Erforschung fundamentaler physikalischer Probleme im Mittelpunkt des Interesses. Der Fokus liegt vielmehr auf Optimierung der bekannten Quellenkonzepte und deren Realisierung.

Ein großer Teil der Arbeit bestand in der Charakterisierung der Debrisemission eines LPPs und der Evaluation verschiedener Unterdrückungstechniken für den Debris. Die Erosion durch Sputtering wurde als der dominante Schädigungseffekt für optische Oberflächen identifiziert. Das Maximum der Debrisemission lag in der Richtung des einfallenden Laserstrahls.

Es wurden vier Debrisunterdrückungskonzepte untersucht: bewegliche mechanische Blenden, Puffergase, elektrische und magnetische Felder. Es wurde gezeigt, dass mechanische Blenden keine realistische Lösung des Problems darstellen. Für elektrische und magnetische Felder wurden Testexperimente durchgeführt. Elektrische Felder zeigten keinen großen Einfluss auf die Debrisemission. Magnetische Felder zeigten sich etwas

wirksamer bzgl. der Debrisunterdrückung, jedoch erscheint die Skalierbarkeit auf große Raumwinkel nicht gegeben. Die Einströmung von Puffergasen zwischen Plasma und Kollektor ist die einzige realisierbare Lösung.

Ein funktionierendes Puffergassystem wurde an einer LPP-Quelle implementiert. Damit konnte eine Optiklebensdauer von 3.6×10^9 Pulsen demonstriert werden, wobei die EUV-Absorption im Gas noch nicht zu groß war. Das ist die höchste bisher veröffentlichte Optiklebensdauer für eine solche Quelle. Mit einer größeren Anzahl von Schichten in der Optik lässt sich eine Lebensdauer von 2.5×10^{10} Pulsen extrapolieren. Diese Zahl liegt in der gleichen Größenordnung wie die Anforderungen an EUV-Quellen für die Massenproduktion [5]. Spiegel mit dieser erhöhten Anzahl von Schichten wurden bereits demonstriert. Daher kann die Optiklebensdauer für xenonbasierte LPP-EUV-Quellen als ein im Prinzip gelöstes Problem angesehen werden.

An GDP-Quellen wurden Messungen der Ionenemission durchgeführt. Das Ionenspektrum einer GDP-Hochleistungsquelle wurde erstmalig charakterisiert. Ähnliche Experimente anderer Arbeitsgruppen bezogen sich auf Laborquellen mit niedriger Repetitionsrate [83, 55]. Auch hier war die Erosion der Optikoberflächen durch energetische Ionen der dominante Schädigungseffekt. Es wurde gezeigt, dass sich die Menge der emittierten Ionen sowohl durch Erhöhung des Puffergasdruckes, als auch durch Beimischung leichter Atome (Wasserstoff), reduzieren ließ. Absolute Messungen der Optiklebensdauer an GDP-Quellen waren nicht Teil dieser Arbeit – sie wurden von Mitarbeitern an einer anderen Quelle durchgeführt. Eine Optiklebensdauer von 10^9 Pulsen wurde dabei von ihnen demonstriert.

Die Möglichkeit, Gasvorhänge einzusetzen, wurde ebenfalls untersucht. Die Ergebnisse sind vielversprechend. Obwohl die benutzte Düse noch erhebliche Optimierungsmöglichkeiten aufweist, konnten Unterschiede im Ionenspektrum nachgewiesen werden. Es konnte auch gezeigt werden, dass der verwendete Aufbau des Gasvorhangs auch der thermischen Belastung bei hohen Repetitionsraten standhält. Letzteres führt bei Gasentladungsquellen oftmals zu großen Problemen.

Ein kleiner Teil der Arbeit widmete sich der Messung der optischen Transmission der verwendeten Debrisfilter. Es konnte gezeigt werden, dass diese Filter eine Transmission von ca. 70 % aufweisen. Dieser Wert ist sehr nahe am theoretischen Maximum. Dies ist aus physikalischer Sicht kein besonders bemerkenswertes Resultat. Für die Praxis der Debrismitigation an GDP-Quellen ist es jedoch sehr wichtig. Die Filter besitzen eine enorme Oberfläche, die zum größten Teil aus Molybdänfolie besteht. Sie

sind einzigartige Sonderanfertigungen, für die es keine Erfahrungswerte für Positionsgenauigkeit, Spannungen im Material etc. gibt. Aus diesem Grund müssen die Filter auf ihre optische Qualität getestet werden. Ein weitere Vorteil des Testaufbaus ist die Möglichkeit, Debrisfilter nach ihrem Einsatz zu untersuchen und so Alterungseffekte in den Filtern zu identifizieren.

Ein weiterer Teil der Arbeit war nicht direkt mit Debrisuntersuchungen verbunden. Die Isotropie einer LPP-Quelle wurde vermessen. Es zeigte sich, dass das Maximum der Emission in der Richtung des einfallenden Lasers war, verbunden mit einem starken Abfall in andere Richtungen. Der wahrscheinlichste Grund dafür ist die Absorption von EUV-Strahlung an der Rückseite des Plasmas. Hierzu wurde ein Modell entwickelt, dass diesen Effekt erklärt. Leider fällt der Bereich größter EUV-Emission mit dem Bereich höchster Debrisemission zusammen. Die starke Anisotropie der EUV-Emission könnte sich auch als Problem für die Beleuchtungsoptik eines EUV-Steppers erweisen.

Wie sieht die Zukunft von EUV-Quellen aus? Die Antwort liegt nicht klar auf der Hand, da der Großteil der Forschung geheimgehalten wird. Es können jedoch einige Trends ausgemacht werden.

Die Erosion von Otpikoberflächen stellt für xenonbasierte Quellen kein Problem mehr dar, auch wegen den Ergebnissen dieser Arbeit. Im Fall von GDP-Quellen sind noch Bruchstücke des Eletrodenmaterials im Prozess anwesend. Diese sind zu groß, um durch ein Puffergas aufgehalten zu werden. Wenn sie in einem Debrisfilter gestoppt werden, können sie zusätzliche Abschattungen hervorrufen und damit die optische Transmission beeinträchtigen. Xenonbasierte Quellen werden jedoch vermutlich nicht in der Lage sein, die Anforderungen der EUV-Leistung für die Massenproduktion (125 W EUV im Zwischenfokus) zu erfüllen, da ihre Konversionseffizienz zu gering ist.

Die Alternativen zu Xenon sind Zinn und Lithium, wobei ersteres von den meisten Beteiligten favorisiert wird. Beide Materialien haben Konversionseffizienzen, die die Anforderungen an die EUV-Leistung erfüllen könnten. Die Probleme der Optiklebensdauer sind bei ihnen jedoch um ein vielfaches größer als bei Xenon. Die Ablagerung von Zinn oder Lithium auf der Optik tritt als zusätzlicher Effekt auf. Ablagerung und Erosion können sich für bestimmt Bedingungen ausgleichen. Es ist jedoch unwahrscheinlich, dass die Bedingungen so gewählt werden können, dass dies über den ganzen Bereich eines Kollektorspiegels der Fall ist. Deshalb muss die Ablagerung komplett unterdrückt, bzw. abgelagertes Material vom Spiegel entfernt werden. Vor kurzem wurden z. B. Reinigungstechniken mit Halogenen vorgeschlagen.

LPP- und GDP-Quellen stehen immer noch im Wettstreit um das bessere Konzept für Massenproduktionsquellen. Der große Nachteil für LPP-Quellen ist der benötigte Laser. Dieser muss ca. 10 - 15 kW in Pulsen von wenigen Nanosekunden Länge bei einigen kHZ Repetitionsrate liefern. Es wird oft behauptet, dass die EUV-Leistung von LPP-Quellen einfach hochgeschraubt werden kann, sobald der passende Laser erhältlich ist. Abgesehen von möglichen, heute noch unbekannten Problemen bei der Hochskalierung, ist dem Autor dieser Arbeit keine Organisation bekannt, die solche Laser ernsthaft entwickelt. Die Kosten und benötigte Zeit werden i. A. als zu hoch angesehen.

Als einzige mögliche EUV-Quelle für den Massenproduktionsbetrieb in der Lithographie erscheint daher eine zinnbasierte GDP-Quelle. Eine erfolgreiche Entwicklung wird davon abhängen, ob die drei großen Probleme von GDP-Quellen, EUV-Leistung, Optiklebensdauer und Elektrodenlebensdauer gelöst werden können. Die neueste Entwicklung auf letztem Gebiet sind rotierende Elektroden, deren Oberfläche sich durch einen Zinnüberzug kontinuierlich erneuert. Diese könnten die Lösung der Probleme der Elektrodenlebensdauer darstellen und durch einen verbesserten Wärmehaushalt auch die Erhöhung der EUV-Leistung erleichtern.

Lebenslauf (deutsch)

Name:	Thomas Hermann Brauner
Geburtsdatum:	23.03.1976
Geburtsort:	Wittlich (Rheinland-Pfalz)
Staatsangehörigkeit:	deutsch
Familienstand:	verheiratet
Privatanschrift:	Felix-Klein-Str. 7, 37083 Göttingen

08/1982-07/1986	Grundschule Wittlich-Friedrichstraße
08/1986-06/1995	staatl. Cusanus-Gymnasium Wittlich
19.06.1995	Erlangung der allg. Hochschulreife
07/1995-07/1996	Zivildienst bei Maria Grünewald, Einrichtung für Menschen mit geistiger Behinderung, Wittlich
09/1996-07/2002	Studium der Physik an der Friedrich-Schiller-Universität Jena
09/1999-06/2000	Auslandsaufenthalt an der University of Warwick (Großbritannien)
19.07.2002	Abschluss des Studiums als Diplom-Physiker
09/2002-12/2006	Doktorand im Institut für Optik und Quantenelektronik der Friedrich-Schiller-Universität Jena
ab 01/2007	Mitarbeiter bei der XTREME Technologies GmbH, Göttingen

Göttingen, den 20.12.2006

Thomas Brauner

Ehrenwörtliche Erklärung (deutsch)

Ich erkläre hiermit ehrenwörtlich, dass ich die vorliegende Arbeit selbständig, ohne unzulässige Hilfe Dritter und ohne Benutzung anderer als der angegebenen Hilfsmittel und Literatur angefertigt habe. Die aus anderen Quellen direkt oder indirekt übernommenen Daten und Konzepte sind unter Angabe der Quelle gekennzeichnet.

Weitere Personen waren an der inhaltlich-materiellen Erstellung der vorliegenden Arbeit nicht beteiligt. Insbesondere habe ich hierfür nicht die entgeltliche Hilfe von Vermittlungs- bzw. Beratungsdiensten (Promotionsberater oder andere Personen) in Anspruch genommen. Niemand hat von mir unmittelbar oder mittelbar geldwerte Leistungen für Arbeiten erhalten, die im Zusammenhang mit dem Inhalt der vorgelegten Dissertation stehen.

Die Arbeit wurde bisher weder im In- noch im Ausland in gleicher oder ähnlicher Form einer anderen Prüfungsbehörde vorgelegt.

Die geltende Promotionsordnung der Physikalisch-Astronomischen Fakultät ist mir bekannt.

Ich versichere ehrenwörtlich, dass ich nach bestem Wissen die reine Wahrheit gesagt und nichts verschwiegen habe.

Göttingen, den 20.12.2006

Thomas Brauner